ADDITIVE MANUFACTURING OF SENSORS FOR EXTREME ENVIRONMENTS

by

Kiyo Tiffany Fujimoto

A dissertation

submitted in partial fulfillment

of the requirements for the degree of

Doctor of Philosophy in Materials Science and Engineering

Boise State University

May 2022

BOISE STATE UNIVERSITY GRADUATE COLLEGE

**DEFENSE COMMITTEE AND FINAL READING APPROVALS**

of the dissertation submitted by

Kiyo Tiffany Fujimoto

Dissertation Title:     Additive Manufacturing of Sensors for Extreme Environments

Date of Final Oral Examination:          10 March 2022

The following individuals read and discussed the dissertation submitted by student Kiyo Tiffany Fujimoto, and they evaluated the student's presentation and response to questions during the final oral examination. They found that the student passed the final oral examination.

| | |
|---|---|
| David Estrada, Ph.D. | Chair, Supervisory Committee |
| Emily Heckman, Ph.D. | Member, Supervisory Committee |
| Brian Jaques, Ph.D. | Member, Supervisory Committee |
| Claire Xiong, Ph.D. | Member, Supervisory Committee |
| Troy Unruh, M.S. | Member, Supervisory Committee |

The final reading approval of the dissertation was granted by David Estrada, Ph.D., Chair of the Supervisory Committee. The dissertation was approved by the Graduate College.

DEDICATION

To Benjamin Joseph Simmons, Kotaro Andrew Simmons and Raiden Oliver Simmons. You motivate me to be the best version of myself, and I love you with my whole heart.

ACKNOWLEDGMENTS

My academic career has been an eye-opening and humbling path paved by the support of an incredible number of people that I am deeply grateful for. There are more people on this path than I can list who have helped to guide me, both past and present. However, I wish to acknowledge the most influential ones here.

To begin, I would like to acknowledge my professor, Dr. David Estrada. You have had an incredible impact on me while serving as my committee chair, advisor, professor and mentor. You opened doors for me that led to opportunities that I never knew existed, and I, without a doubt, would not be at this point in my life if it were not for your presence in my life. It is through your passion for science and learning, your creativity, your vision, your unwavering work ethic, your thoughtful approach to research, and, finally, in the way you care for those around you that I have been shown the impact of not only the work that we do, but also the impact of who we choose to be as people.

I would also like to acknowledge my INL Graduate Fellowship mentor, Troy Unruh, who has been alongside me since the beginning of my graduate career. You took a chance on me, and it propelled my career in ways that otherwise wouldn't be possible. Thank you for the time and energy you invested in me, for being a friend, and for always being willing to lend an ear and give advice. I will forever be grateful for our time together, and I am so thankful that you were a part of my journey.

I would like to acknowledge Dr. Robert Fox, Dr. Donna Baek, Dr. Mary Case and Dr. Michael McMurtrey. Thank you for welcoming me into the lab and for creating space for me at the INL so I could finish the remainder of my dissertation work at the INL. A very special thank you to Dr. Robert Fox, your leadership has had substantial impact in my life, and I feel so grateful and lucky to have had the opportunity to be part of your team.

There were many hours spent in the Idaho Microfabrication Laboratory at BSU, and a large portion of this research work would not have been possible without the support of Travis Gabel and Peter Miranda. Thank you for the many hours of discussion, your patience, and for the time spent in assisting me with various research tasks. Your contribution to my graduate school experience is highly regarded.

I would like to acknowledge my dissertation advisory committee members, Drs. Emily Heckman, Claire Xiong and Brian Jaques. Thank you for your guidance and support throughout this research. I would also like to thank those in the Advanced Nanomaterials and Manufacturing Laboratory. Especially, Dr. Tony Varghese,  Dr. Twinkle Pandhi, and Katie Yocham for your friendship, for teaching me the value of a positive attitude, for your collaborative character, and for the many hours of fruitful discussion on a wide range of topics.

This work would also not have been possible without the support of the MSE department at BSU. Thank you for providing the facilities to support innovative and world changing research. I am grateful to the MSE staff for creating a supportive and productive environment for students to thrive and grow. There have been a few notable individuals along the way who have served as friends, confidants, and the very best

cheerleaders anyone could ask for, they include Kevin Shumard, Jenny Fothergill, Jennifer Watkins, Courtney Hollar and Tim Phero. Thank you from the bottom of my heart.

The Chemistry department at Boise State University was instrumental towards shaping me as a scientist and for training me in research methods. Special acknowledgement goes to Dr. Kevin Ausman, Dr. Henry Charlier, Dr. Michael Callahan, Dr. Dale Russell and Dr. Kevin Cornell. Thank you for your contributions to an undergraduate program that helped me to discover my passion for science and the research process.

I would like to acknowledge my family (Andy, Yoshie, Stan, Steve and Akina) for their unwavering support in all my endeavors. Thank you for your constant love and encouragement as I have tried to find my path. I have come to realize that this is a very rare thing to have. Please know, this would not have been possible without you.

Last, and most importantly, I would like to thank my husband, Benjamin Simmons and our two boys, Kotaro and Raiden, for the massive amounts of love,

support, patience and kindness you provided to me so we could make it through to the

end. It has been a long and challenging journey, and *we* did it!

ABSTRACT

Advanced manufacturing based direct-write technologies have emerged as the predominant enabler for the fabrication of active and passive sensors for use in harsh operating environments. The ability to directly write and integrate electronic components onto physical packaging can be achieved with additive manufacturing (AM) methods such as direct write technologies (DWT) which include aerosol jet printing (AJP), Ink Jet Printing (IJP), Plasma Jet Printing (PJP), and Micro-Dispense Printing (MDP). In this work, we investigate the use of these methods to accelerate, modernize, and enhance the functionality of sensors and instrumentation to achieve the goal of improving the safety and efficiency of processes that take place within harsh environments. This dissertation accomplishes these objectives with the following activities: (1) an investigation targeting structural health monitoring of space habitats with the development of AJP capacitive strain gauges, (2) an investigation on the melt behavior of AM melt wires by benchmarking the performance of AM melt wires to their classically fabricated counterparts for peak temperature monitoring in nuclear reactors, and (3) the development of AM neutron dosimeters for directional flux monitoring in the TREAT reactor. The results from these activities highlight DWTs as potential solutions for the development of miniature and robust sensors that are difficult to achieve with traditional fabrication methods for nuclear and aerospace instrumentation.

TABLE OF CONTENTS

LIST OF TABLES

LIST OF FIGURES

LIST OF ABBREVIATIONS

| | |
|---|---|
| μm | micrometer |
| Ω·cm | ohm per centimeter |
| °C | degrees celsius |
| 3-D | Three Dimensional |
| AEC | Atomic Energy Commission |
| Al | Aluminum |
| AJP | Aerosol Jet Printing |
| AM | Advanced Manufacturing |
| APBC | All-Purpose Barge Cement |
| ASI | Advanced Sensors and Instrumentation |
| ATR | Advanced Test Reactor |
| Bq/g | Bequeral per gram |
| BUSTER | Broad Use Specimen Transient Experiment Rig |
| CAD | Computer-Aided Design |
| CCM | Cubic centimeter per minute |
| Co | Cobalt |
| cP | centipoise |
| CSGs | Capacitance based Strain Gauge |
| DOE-NE | Department of Energy Nuclear Energy |
| DLP | Digital Light Processing |

| | |
|---|---|
| DSC | Differential Scanning Calorimetry |
| DWT | Direct Write Technologies |
| EBR-1 | Experimental Breeder Reactor 1 |
| EDL | Entry, descent and landing |
| EDS | Energy Dispersive X-Ray Spectroscopy |
| E/W | East/West |
| Fe | Iron |
| g | gram |
| GAIN | Gateway for Accelerated Innovation in Nuclear |
| GE | General Electric |
| GHG | Greenhouse Gas |
| GW | Gigawatt |
| HE-RSG | High Elongation Resistance based Strain Gauge |
| HPGe | High Purity Germanium |
| IEA | International Energy Agency |
| IJP | Inkjet Printing |
| in. | inch |
| INL | Idaho National Laboratory |
| kHz | kilohertz |
| kN | kilonewton |
| klbf | kilo pound force |
| kW | kilowatt |
| LCR | Inductance Capacitance and Resistance |

| | |
|---|---|
| MCNP | Monte-Carlo N-Particle |
| MDP | Micro-Dispense Printing |
| MeV | megaelectron volt |
| min | minute |
| MTRs | Material Test Reactors |
| MIMIC-N | Materials Irradiation Capability for Neutron Sensors |
| MJ | Megajoule |
| mm | millimeter |
| MNFW-1 | MIMIC-N Flux Wire Experiment 1 |
| MNFW-2 | MIMIC-N Flux Wire Experiment 2 |
| MPa | Megapascal |
| MRCC | maximum relative change in capacitance |
| ms | millisecond |
| MTS | Material Test System |
| MW | Megawatt |
| NASA | National Aeronautics and Space Administration |
| NE | Nuclear Energy |
| NEET | Nuclear Energy Enabling Technologies |
| Ni | Nickel |
| NIST | National Institute of Standards and Technology |
| N/S | North/South |
| NSUF | National Science User Facility |
| OD | Outer Diameter |

| | |
|---|---|
| PA | Pneumatic Atomizer |
| PDS | polydimethylsiloxane |
| PET | polyethylene terephthalate |
| pF | picofarad |
| PIE | Post Irradiation Examination |
| PJP | Plasmajet Printing |
| PMMA | polymethyl methacrylate |
| PVP | Polyvinylpyrrolidone |
| RPM | Rotations Per Minute |
| RSG | Resistance based Strain Gauge |
| SEM | Scanning Electron Microscopy |
| sec. | second |
| $sec^{-1}$ | 1/sec |
| SHM | Structural Health Monitoring |
| $SiO_2$ | silicon dioxide |
| Sn | Tin |
| TEM | Transmission Electron Microscopy |
| Ti | Titanium |
| TREAT | Transient Reactor Test Facility |
| U-235 | uranium-235 |
| U.S. | United States |
| U.S. NRC | United States Nuclear Regulatory Commission |
| V | Volt |

XCT              X-Ray Computed Tomography

XRD             X-Ray Diffraction

Zn               Zinc

CHAPTER ONE: INTRODUCTION

## 1.1 General Introduction

Innovations in additive manufacturing (AM) methods such as direct write technologies (DWT) stand to revolutionize the way we produce manufactured goods by enabling the direct printing of electronic devices and metal parts. The ability to directly write and integrate electronic components onto physical packaging can be achieved with these techniques.[1,2] Additive manufacturing fabricates an object by the successive addition of materials, which are then joined together layer by layer, and is defined by the American Society for Testing and Materials (ASTM) in ISO/ASTM 52900:2015 as a "process of joining materials to make parts from a 3D model data, usually layer upon layer, as opposed to subtractive manufacturing and formative manufacturing."[3]

Within the AM space there exists subclassifications that include binder jetting, direct energy deposition, material extrusion, material jetting, powder bed fusion, sheet lamination and vat polymerization.[3] For the work here, there is a focus towards DWT methods, which typically fall within the classification of material extrusion and material jetting, for printed electronics applications. These methods are constantly evolving, and some current examples of such methods include such methods include Aerosol Jet Printing (AJP), Ink Jet Printing (IJP), Plasma Jet Printing (PJP), and Micro-Dispense Printing (MDP) capable of producing 2D or 3D material patterns with desired geometries, architecture, and compositions using computer aided design software. As DWT gain popularity due to their flexibility in patterning and ability to facilitate rapid

prototyping, the printed electronics community is exploring them for the development of advanced sensors. More, specifically, applications for extreme environments with a focus on structural health monitoring and in-pile measurements within aerospace and nuclear industries, respectively, are of particular interest. DWT provide a potential solution for the development of miniature, robust sensors enabling a reduction in design space and/or radiation shielding requirements that are difficult to achieve with traditional fabrication methods used for nuclear and aerospace instrumentation. Additional benefits for aerospace, especially for soft structural materials, are found in the wide range of substrates available for DWT to include flexible materials such as polyimide (Kapton), polyethylene terephthalate (PET) and polydimethylsiloxane (PMDS). To expand on this, the National Aeronautics and Space Administration (NASA) has begun exploring DWT for in-space manufacturing of sensors and for structural health monitoring of soft materials used for inflatable habitats, parachutes and decelerating systems.[4–6] For nuclear applications, DWT are being explored to enable advanced instrumentation capable of measuring field properties inside advanced test reactors to expedite fundamental materials discoveries in order to advance the nuclear fuel cycle.[7,8]

DWTs are rapid prototyping processes that do not require costly prefabricated photomasks or templates while being relatively low cost. For the most part, functional materials in the form of nanoparticles are dispersed in a solvent, and are then deposited onto a substrate, which is followed by the need to sinter the printed material with either *ex-situ* (AJP, IJP, MDP) or *in-situ* (PJP) methods using an energy source such as heat, lasers, or photonic flash to form a continuous film.[9–13]

## 1.1.1 Direct Write Technologies

<u>1.1.1.1 Aerosol Jet Printing</u>

Aerosol jet printing is a digital printing technique that offers a non-contact, liquid phase, microscale (10-100 µm) patterning that has been used to fabricate a variety of sensors to with enhanced capabilities to include sensors for harsh environments, flexible temperature sensors, gas sensors, strain sensors, touch sensors and electrochemical sensors.[14–21]

The flexibility in fabrication and patterning is afforded with its broad material compatibility range, which is attributed to its ability to print with inks having viscosities ranging from 1-1000 cP and with particle sizes < 500 nanometers.The rheological properties of the inks directly affect the minimum achievable feature size. Additionally, the inks intended for use with this printing technique, can be solutions, dispersion, or solvents, but they must possess behavior that is shear thinning or Newtonian in nature.[22] The formation of aerosol within this system relies on the interplay between surface tension, viscosity, volatility and density of the ink, and is accomplished with the use of ultrasonic or pneumatic atomization, and those processes are described in the following two sections that are summarized from *Wilkinson* et al.[23]

<u>1.1.1.1 Ultrasonic atomization</u>

To produce an aerosol via ultrasonic atomization (Figure 1.1), a transducer is submerged within a medium (usually water) capable of transferring the high frequency oscillations that are produced. The wave propagates through the medium to a vial, containing the ink, that is positioned above the transducer. In the vial, a standing wave is formed at the surface and the superposition of consecutive waves creates large peaks. At

the top of these peaks, local shear results in small droplets being ejected from the bulk

ink volume. Positive pressure, in the form of a carrier gas, is applied to the vial that then

drives the aerosol from the vial to the deposition head.

The ultrasonic atomizer can produce an aerosol from small particle size (<50 nm),

low viscosity (1-10 cP) inks having small volumes of around 2 mL with a maximum

particle loading of 55 wt%. Aerosols generated are typically low in dispersity, with

droplet sizes ranging from 2 to 5 μm.
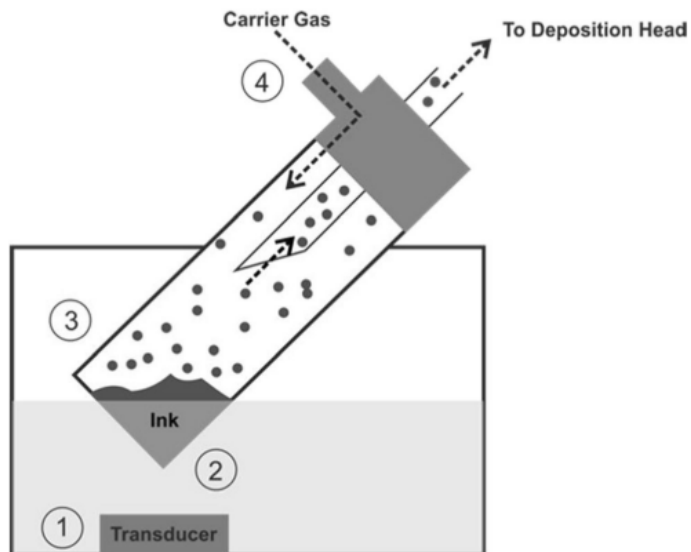


**Figure 1.1      Schematic of Ultrasonic Atomization from Wilkinson et Al.[23]
Operation principle of the ultrasonic atomization process to include the (1)
transducer, (2) transfer medium, (3) formation of waves, (4) and the carrier gas to
transfer to the deposition head for AJP printing.**

1.1.1.2 Pneumatic Atomization

Within the pneumatic atomizer (Figure 1.2), which is a collision-style atomizer,

an inert atomization/carrier gas (usually nitrogen) is applied into the container holding the

ink to form a mist/aerosol. The carrier gas is accelerated across the top of the ink supply

channel, which creates a region of reduced static pressure, and the ink is then drawn to

the carrier gas flow. Once the ink reaches the level of the carrier gas stream, the topmost

layer of the bulk volume of ink is sheared to produce a series of polydisperse droplets.

Within the mixture of droplets, large, high-inertia droplets impact the side wall of the

atomizing chamber, and return to the reservoir, and the small, lower inertia droplets

remain as aerosol and then are exhausted from the atomizer towards the virtual impactor.

The aerosol that has made it from the reservoir to the virtual impactor is then further

separated with low-inertia droplets being ejected via the exhaust gas, and high-inertia

droplets move on towards the deposition head.

This atomization approach is the more tolerant method as it is capable of printing

inks having viscosities ranging from 1-1000 cP, particle sizes of less than 500 nm, and a

particle loading of 85 wt% to produce aerosol droplets of 1-5 μm.
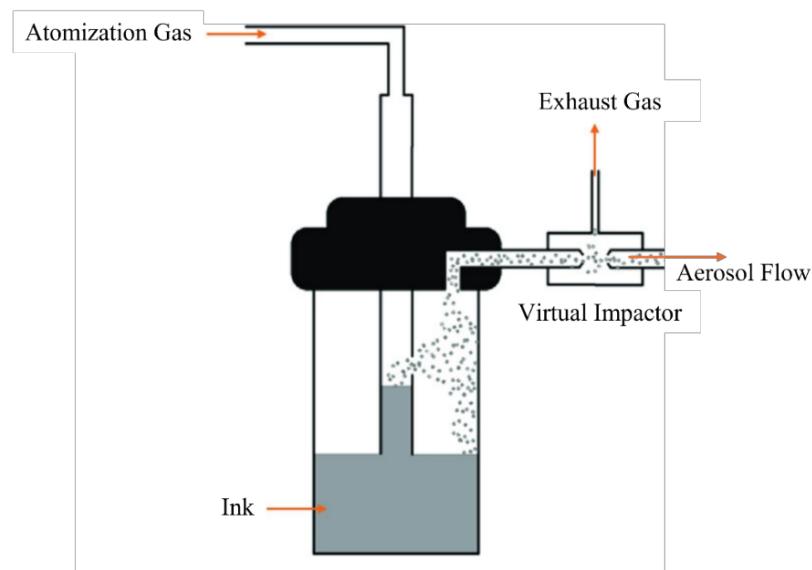


**Figure 1.2.    Schematic of Pneumatic Atomization.**[24]

<u>1.1.1.2 Plasma Jet Printing</u>

A relatively new printing technology that emerged around 2016, PJP, introduces

the potential for *in-situ* sintering and the tailoring of physical and chemical characteristics

of the printed material.[5,25,26] Similar to the principle of the AJP, PJP is a multi-material additive manufacturing platform, which generates an aerosol of the desired material that is then deposited onto a substrate with the use of a carrier gas. However, with AJP and other DWTs mentioned, a post processing step is required to sinter and remove any ink additives in the form of organic compounds to obtain a consolidated thin film, which may subject the print and substrate to relatively high processing temperatures that can range from 50 to 400 °C. A significant difference between the PJP and other DWTs is the integration of an *in-situ* plasma sintering, and is considered a method for "dry" printing without the need for post processing steps. This process combines an atmosphere pressure cold plasma, which consists of a dielectric barrier discharge of a gas (helium, argon, hydrogen, etc.) with aerosol delivery, which makes it a low temperature deposition process (70-90 °C).[25]

A high level overview of the PJP will be provided, and a more detailed overview can be found within the work completed by *Ramamurtri et al.*.[25] To begin, the major controls for the PJP are the gas, liquid and plasma for the atmospheric print head based on the dielectric discharge of gas mixtures and aerosolized particles from the bulk ink volume. The material to be deposited can be in the form of a solvent, dispersion or solution, and the PJP will deposit starting materials having loading concentrations of 1.6-3.2 wt% and viscosities close to 1 cP.

The PJP printhead contains a dielectric tube that contains a nozzle on one end, has metal electrodes dispersed over it which are connected to a high voltage power supply that creates a discharge of a gas mixture, and a manifold that delivers aerosolized material into the tube. Through the liquid inlet, the material to be printed is introduced to

the atomizer, which creates an aerosol of the delivered material with a piezoelectric

nebulizer. The non-aerosolized material exits via the liquid outlet for recirculation. The

aerosol, however, is picked up by a carrier gas and passes through the plasma region

before directed to the substrate. When the aerosolized ink enters the plasma region, it is

subjected to a combination of electrical and magnetic fields, electro-hydrodynamic

forces, and bombardment with the plasma species. The material to be printed is then

accelerated out of the nozzle with a momentum that is created by an externally applied

electric field and plasma that expels the material The nozzle of the PJP is detachable and

can be interchanged to control the geometry and resolution of the printed features, and a

schematic of the PJP printhead is provided in **Fig. 1.3.**
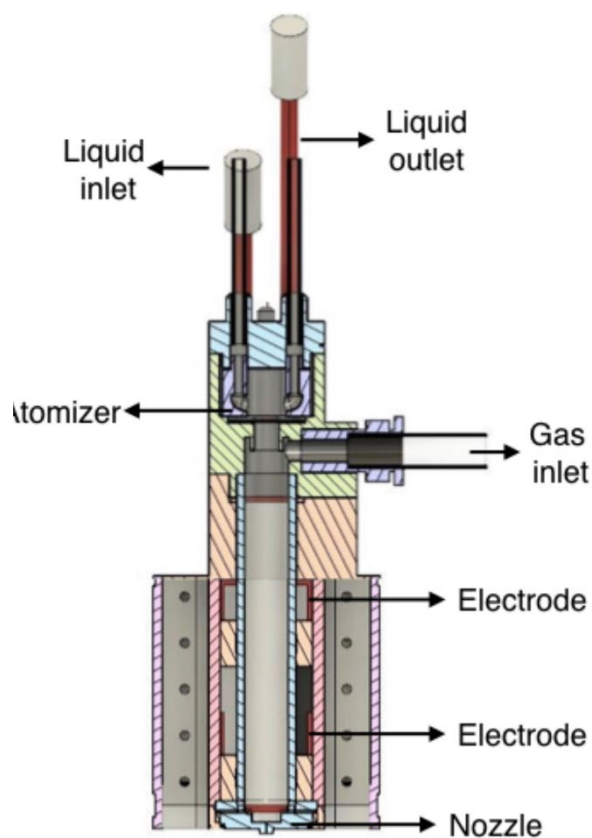


**Figure 1.3**     **Schematic of the PJP print head.**[25]

## 1.1.1.3 Inkjet Printing

IJP is a fully digital, non-contact printing technique capable of producing feature sizes of as small as 20 μm, which involves the generation and precise deposition of small ink droplets onto a substrate. includes continuous ink jet (CIJ) and drop-on-demand (DoD) printing that has been used to demonstrate the fabrication of a variety of sensors ranging from those based on electrochemical processes and those capable of monitoring humidity, gas, temperature, strain, and many more.[27–35]

CIJ and DoD differ in that CIJ ejects a continuous jet of ink droplets from the nozzle, which require the systems to include deflection or droplet selection devices making these systems the more complex of the two, as DoD only ejects an ink droplet on demand, and doesn't require the additional systems.[36,37] However, both CIJ and DoD have similar working principles in that a pressure force is generated by various types of actuation mechanisms such as thermal, electrostatic and piezoelectric. The forces developed from these actuators then forces the ink through the nozzle causing the ejection of an ink droplet, which is then directed to the substrate. As DoD, does not require the additional systems for droplet deflection or droplet selection, these systems typically have greater printing accuracy and resolution due to their printheads generally having a smaller distance from the nozzle to the substrate.[37]

IJP is capable of dispensing a wide variety of functional fluids, such as solvent and aqueous bases nanoparticle suspensions, ultraviolet curable fluids, biological solutions, and any chemical compatible with the printing cartridge. Liquids used are recommended to have a high boiling point and low evaporation rate to avoid drying at the nozzle-air interface. Additionally, materials for printing with IJP must have a viscosity

range of 10-12 cP, a surface tension from 28-33 dynes/cm, and particle sizes < 200 nm

where the particle size is dependent on the nozzle size selected. Finally, these materials

should have a pH range between 4-9 to prevent damage to the print cartridge.
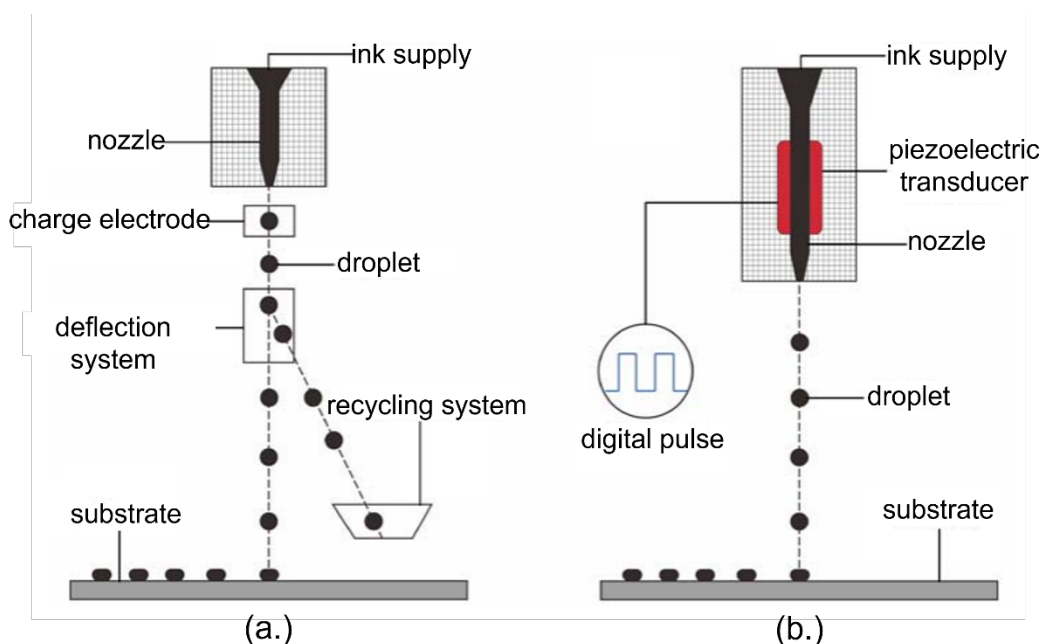


**Figure 1.4    Schematic diagram of inkjet printing. (a.) Continuous inkjet mode and (b.) drop-on-demand mode.**[38]

<u>1.1.1.4 Micro-Dispense Printing</u>

MDP is a relatively simple material dispensing method that can also be classified

as an extrusion-based method that is essentially a system that provides controlled paste

dispensing. The applications of this printing method for sensors is generally within the

flexible electronics space with the development of gas, strain, pressure, taste, textile,

chemical, and temperature sensors.[39–47] An extensive list of around 10,000 commercially

available materials are available for use with this method due to its compatibility with a

wide range of viscosities from 1 cP nanoparticle inks to 1 million cP flake loaded pastes,

and having similar rheological properties to screen printing pastes, which are typically

based on non-aqueous solvents showing Newtonian or pseudoplastic behavior.[48–50]

There are a few extrusion-based printing technologies available that provide varying levels of precision, but their working principles are similar, as deposition of material onto a substrate relies on pressure applied to material loaded in a syringe to produce a continuous flow of materials through a nozzle. The applied force can either be piston driven or pneumatic driven. The feature sizes that can be produced are dependent on the nozzle sized used and reported feature sizes range from 10 to 300 μm, where the achievable feature size is dependent on the inner diameter of the nozzle tip. Additionally, the particle size of the nanoparticle inks or pastes is suggested to be at least ten times larger than the dispensing tip or nozzle used. Finally, the applied force can either be piston or pneumatic driven. Two examples of printing systems that operate under these principles include the Voltera V-One (**Fig. 1. 5**), which is piston driven and nScrypt's SmartPump™ (**Fig. 1.6**), which is a pneumatic driven system.
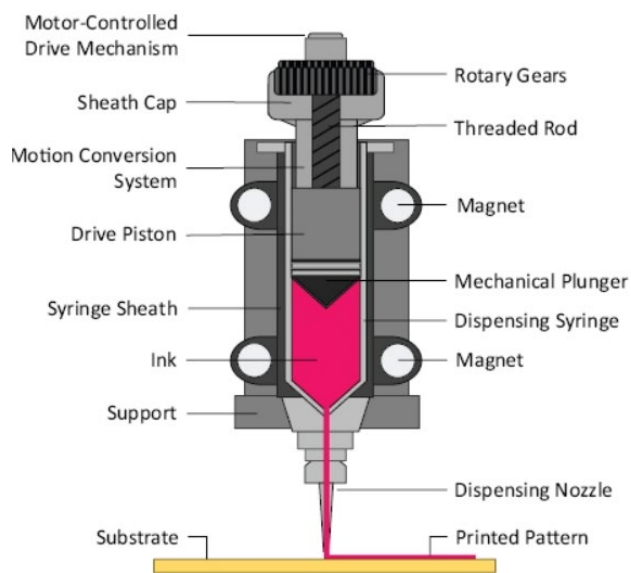


**Figure 1.5**      **Schematic diagram of the Voltera V-One mechanical displacement syringe extruder.**[50,51]
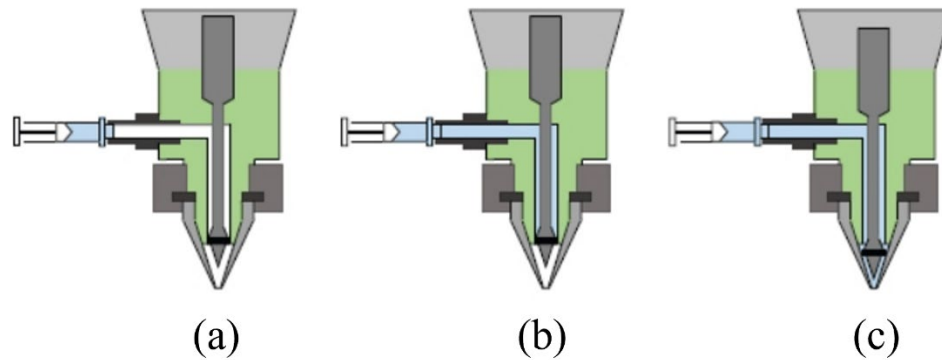
**Figure 1.6**     **Operating mechanism of the high precision nScrypt SmartPump™: (a) a syringe or cartridge is filled with material and attached to the valve body, (b) positive pneumatic pressure causes the material to flow into the valve body, and (c) the valve is opened and the ink flows through the dispensing tip to the substrate.**[50,52]

### 1.1.2 Additive Manufacturing for Extreme Environments

Extreme environments are described as habitats having inhospitable conditions for life where harsh environmental conditions exist beyond optimal range for human development.[53] Sensors developed for nuclear reactors and space applications are required to tolerate high temperature, large strain/stress, corrosive/erosive environments, vibration, and intense radiation.[54–57] Conventional sensors are not capable of withstanding these harsh environments, which requires that sensors be adapted in terms of their materials and sometimes even sensing modalities. For example, radiation and high temperatures can cause changes to the mechanical and electrical properties of metals and semiconductors making conventional thermocouples prone to drift and loss of calibration, transmutation, or even mechanical fracture.[55] While material considerations are key for harsh environment sensor and instrumentation development and fabrication, additional device design challenges are introduced with the need to produce highly specialized designs for use with non-conventional structures especially in the aerospace industry, and

for nuclear application size constraints result in device geometries that can be severely limited.[58,59]

The limiting factor for implementing DWT in nuclear instrumentation fabrication is the current selection of commercially available feedstock materials that are compatible with these technologies. However, the database of materials available for DWTs is rapidly expanding and benefitting greatly from emerging nanomaterials development, and efforts are currently being made to significantly expand the library AM materials to include those that are more nuclear relevant. These efforts provide the necessary path towards incorporating these novel methods for nuclear energy applications, and such material breakthroughs will revolutionize in-pile sensor development and deployment for the monitoring of nuclear fuel and material behavior during an irradiation experiment. These development efforts span a wide range of materials to support various sensor development efforts, but some examples of these materials include graphene, platinum, thermoelectrics, nickel and nickel oxide, chalcogenide based inks, which have all been demonstrated to be compatible with DWTs of interest.[14,27,60–64]

Methods for ink synthesis encompass both top-down and bottom-up methods. This process begins with nanoparticles of the metal, ceramic or alloy of interest in the form of a powder or a dispersion. The key challenges of the top-down approach are found in obtaining a homogenous dispersion of functional material with a solvent system compatible with DW technologies, limited control over particle size and large particle size distributions. On the other hand, bottom-up methods for metallic nanoparticles requires the synthesis of nanoparticles from their metallic precursors. A capping agent, which induces steric stabilization to minimize agglomeration is employed to enhance

suspension stability and is a critical factor in producing AM feedstock for DWT. The bottom-up approach is the preferred method, as it allows for greater control over particle size and size distribution, which are key properties of affecting the quality of the ink formulation. Key challenges associated with bottom-up methods includes the development of an appropriate synthesis method, isolation of desired particle shape, particle size and distribution, and identification of an appropriate capping agent.

Towards this end, this work aims to provide the foundation to develop the fundamental knowledge about the impact of harsh environments on the microstructure and physical properties of AJP deposited materials, and the resulting influence on sensor performance. The determination of how materials used in DWT respond in extreme environment conditions may lead to the development of sensors intended for nuclear and aerospace applications while using a fabrication technique that is more environmentally friendly, is more cost efficient and is better able to utilize critical materials when compared to classical fabrication methods. Two industries that could stand to benefit substantially from innovations in sensor and instrumentation technologies include nuclear and aerospace. While the use of DWT within these two industries is expected to increase, much work remains to be done to understand the behavior of DWT deposited materials and DWT fabricated devices under harsh and extreme environments.

**1.2 Motivation**

1.2.1 Nuclear Energy

With the Industrial Revolution the way humans lived and worked around the world was forever changed with the development of industrial processes facilitating a transition from using wood and water as the main energy sources to those that are based

on fossil fuels. With this change came a higher standard of living, and for over a century that standard of living has only continued to grow as technological advances have accelerated our ability to steadily increase productivity and accessibility while also reducing costs associated with manufacturing. Consequently, for over a century our use of fossil fuel-based energy sources has rapidly increased, and now the world is at a point where it is dependent on those energy sources derived from fossil resources.[65]

Fossil fuel consumption within the transportation sector, electricity production, industrial processes, agriculture, commercial and residential uses, and land use and forestry produce greenhouse gas (GHG) emissions and has resulted in the accumulation of GHGs within the Earth's atmosphere. The rapid increase in GHG emission and accumulation within the Earth's atmosphere is alarming as it is linked to environmental degradation. Environmental degradation can be defined as "the depletion of environmental resources such as air, water and soil; the elimination of ecosystems; extinction of wildlife; and pollution, perceived to be harmful to the ecosystem", and it is more certain than ever that humans have played a critical role in environmental degradation attributed to climate change or global warming, and the salience of climate change is ever growing.[66] With this understanding, it is critical that drastic action is taken in reducing global warming to avoid reaching tipping points that will force us towards reduced growth and environmental disaster.[65–68]

Furthermore, ambitious climate action has reached a global scale with the implementation of the Paris Agreement (2015) and the goal of holding the global average temperature increase to well below 2 °C above pre-industrial levels from a drastic reduction in GHG emissions.[69] To support a path towards zero GHG emissions, focus has

been made towards the electricity sector, which, according to the International Energy

Agency (IEA), is the largest producer of GHG emissions in the world. To facilitate a total

transformation of the energy systems that are the foundation of our economies the IEA

has developed a roadmap for the global energy sector with the goal of achieving net zero

by 2050 to increase the use of clean and renewable energy technologies.[70] Advancements

in clean energy technologies have resulted in the formation of an energy nexus, for

reducing GHGs, consisting of renewable, sustainable, and low carbon emitting energy

sources, which includes nuclear, solar, hydro, wind, biomass and geothermal to make the

transition away from gas and oil to those sources that are more environmentally

friendly.[65,71] A key utility to address in the energy transition is nuclear energy (NE), and

according to the Nuclear Energy Institute, within the U.S., NE generates most of our

nation's clean energy (over half). This can be attributed to NE's superior energy density

which enables it to meet baseload power and peak loading point demands and has made it

a primary contributor within the nexus of clean energy sources. A diverse

decarbonization strategy is key towards making energy transitions to mitigate climate

change, and advances in renewable energy sources have had an unexpected impact on the

nuclear energy landscape.[71]

Nuclear power is created by harnessing nuclear fission energy with the from a

wide range of fuels available consisting of metallic fuels (U-Mo, U-Zr), plate fuels like

Al-$U_3Si_2$, ceramic fuels ($UO_2$, UN, UC, $UB_2$, $UB_4$), Tri-structural Isotropic particle fuel

(TRISO) made up of a uranium, carbon and oxygen fuel kernel, and mixed oxide fuels

($UO_2$ and $PuO_2$), thorium-based and plutonium-based fuels that release many high-energy

neutrons during a nuclear fission where the nucleus of an atom splits into two or more

smaller nuclei.[72–74] This causes a chain reaction that then heats the surrounding water coolant to create steam that spins a turbine to generate electricity. The environment within the reactor core is exceptionally harsh due to a combination of high temperature, high stresses, aggressive coolant chemistries and intense radiation fluxes causing high operational burdens to structural materials.[75] The first presentation of a nuclear reactor was performed by a group of scientists led by Enrico Fermi in 1942 with the development of Chicago Pile-1 erected on the floor of a squash court beneath the University of Chicago's athletic stadium.[76] After World War II, Congress created the Atomic Energy Commission (AEC) to encourage the development of nuclear energy for peaceful civilian purposes.  From there, the AEC authorized the construction of the Experimental Breeder Reactor I (EBR-I) in Idaho, and in 1951 EBR-I successfully first demonstrated the production of electric power from a nuclear reactor as it lit up four 200-watt light bulbs with the electricity it generated, which proved the viability of nuclear or atomic energy as a power source for electricity generation.[77]  In 1955, the city of Arco, Idaho became the first to be lit by atomic power from a reactor built near EBR-1, the BORAX III developed by Argonne National Laboratory.[78] Since then, nuclear has developed a reputation of being a 24/7 carbon-free electricity source, and there are currently 444 operable reactors across the globe, and its total global energy production contribution is 10.5%.[79] However, within the public domain there is a very strong awareness of the potential hazards of nuclear power that are associated with nuclear criticality and the release of radioactive materials, and the main safety concern of NE has always been the probability of uncontrolled release of radiation.

While nuclear energy has had a declining share in global electricity the current efforts in creating a clean energy future has reinvigorated interest and commitments towards preserving the current fleet of nuclear reactors within the United States (U.S.) and has accelerated momentum in the development of next generation reactors.[61,80,81] However, within the public eye, there is significant concern over the safety of NE which is prompted by severe reactor accidents such as Chernobyl in 1986 , Three Mile Island in 1979 and Fukushima Daiichi Nuclear Power Plant in 2011, which have emphasized the need to enhance accident tolerance of nuclear reactors to address sustainability concerns with advanced fuel developments and to implement more robust structural materials for the enhanced safety and efficiency in operations necessary to develop advanced fuel cycle technologies.[82–84]

Within the United States the Department of Energy Office of Nuclear Energy (DOE NE) has identified the key challenges facing nuclear energy according to the *Nuclear Energy R&D Roadmap Report to Congress (2010)* are: Capital cost, waste management, proliferation and terrorism risks, and safety and reliability. Within this roadmap key R&D objectives were identified and served as guidelines for the development of the Nuclear Energy Enabling Technologies (NEET) program, and in its efforts to resolve U.S. industry nuclear technology development issues, NEET aims to support innovative and cross-cutting nuclear energy technologies. The Advanced Sensors and Instrumentation (ASI) program element within NEET, which fosters R&D necessary to produce and deploy innovative and advanced sensors, as well as instrumentation controls, and analytics for the current nuclear fleet and advanced reactor designs to ensure safety in operation. Additionally, the development of advanced sensors and

instrumentation supports efforts in conducting experimental and computation research to characterize, understand and predict materials behavior in extreme nuclear environments.

The development, demonstration and qualification of advanced reactor fuel forms will facilitate an accelerated deployment of advanced reactor technologies, which requires a greater understanding of the irradiation effects on fuels and material behavior.[85] This understanding is critical for the assessment of potential materials for any nuclear reactor concept to ensure safety, reliability and efficiency in operations, and this understanding is acquired with the use of Materials Test Reactors (MTRs) such as the Advanced Test Reactor (ATR) and the Transient Reactor Test Facility (TREAT) at the Idaho National Laboratory (INL) where specialized irradiation tests and targeted measurements are made possible.[86–88] Current in-pile instrumentation efforts look to assess, verify, and increase the precision of measurements under irradiation with the development of advanced sensors capable of monitoring temperature, physiochemical conditions, neutron flux/dose, pressure, and multi-physics field properties. To maximize time, resources, and data collection, advanced and miniaturized instrumentation is needed to accurately measure such properties in the extreme and complex environment of nuclear test reactors.

Such instruments must not only be miniaturized but they must also be robust to the nuclear reactor environment and would preferably provide real-time data aligned with user needs. Towards this end, advanced manufacturing (AM) techniques such as DWT have demonstrated significant potential for the development of advanced in-pile instrumentation. The database of materials available for DWT is rapidly expanding and benefitting greatly from emerging nanomaterials development. Hence, it is imperative to

understand the nuclear related capabilities of DWT and their associated materials, which may be used in the fabrication of future nuclear relevant components, sensors and systems. With a focus on evaluating the irradiation behavior of DWT materials, our results have a much larger and crosscutting impact across multiple DOE-NE programs. As such, the results of this project will be highly relevant to the Department of Energy – Nuclear Energy (DOE-NE) programs in Advanced Reactor Technologies, Nuclear Energy Enabling Technologies (NEET), and Small Modular Nuclear Reactors (SMR) which all stand to benefit from advanced manufacturing methods, and developments in advanced manufacturing techniques for applications in printable electronic devices will significantly decrease the nuclear innovation cycle time.

On a fundamental level, safety in nuclear reactor operations requires an in-depth understanding of how nuclear fuels and structural elements behave within a reactor environment.[89] Furthermore, the development of advanced reactor technologies will require materials to have the ability to withstand even higher temperatures and radiation flux than ever before and requires a greater understanding of irradiation effects on fuels and material behavior. The ability to develop an understanding of material behavior under normal and transient reactor conditions is accomplished with irradiation experiments conducted within MTRs.

1.2.1.1 Materials Test Reactors

Materials Test Reactors or research reactors are distinctly different from power reactors, as they are not used for power generation. Currently there are about 220 research reactors operating in 53 countries and they are used as a neutron source for research and training, neutron activation analysis, irradiation testing of materials,

radiography or the production of radioisotopes for medicine and industry.[90] These reactors are ideal for research activities as they are versatile in their operating modes (steady or pulsed), and most are more simple than typical power reactors and they have a very different set of safety-related parameters since they operate at lower temperatures and lower power than typical power reactors. With notable exception being the Advanced Test Reactor, which will be addressed in section 1.2.1.2.

These reactors differ dramatically in their capabilities and their design, and common research reactor designs include pool-type, tank-type and tank-in-pool reactors, and fast reactors. The Idaho National Laboratory is currently home to a few research reactors the Advanced Test Reactor (ATR), the Advanced Test Reactor Critical Facility (ATR-C), the Neutron Radiography Reactor (NRAD), and the Transient Reactor Test Facility (TREAT), which are all very different types of research reactors with regards to their capabilities. For the scope of this work, the ATR and TREAT are highlighted in the following sections.

### 1.2.1.1.1 Advanced Test Reactor

Known as one of the world's premier test reactors for studying the effects of intense neutron radiation on reactor materials and fuels, ATR began operation in 1967 and has continued to operate on average of 250 days per year. This test reactor was designed to evaluate the effects of intensive radiation on material samples, especially nuclear fuels, and is the highest power and most versatile test reactor operating in the world. In 2007, DOE designated the ATR as a National Science User Facility (NSUF) to promote accessibility to the broader community and INL, and with that the goals of ATR NSUF were to:[91]

1. Define the cutting edge of nuclear research technology in high temperature and high radiation environments.

2. To contribute to improved industry performance of current and future light water reactors

3. To stimulate cooperative research between those conducting basic and applied research.

The ATR is a pressurized light water moderated and cooled, beryllium reflected, highly-enriched uranium fueled, nuclear research reactor with a maximum operating power of 250 MWth.[92] The core cross-section is shown in **Figure 1.7**, and consists of 40 curved fuel elements configured into ATR's characteristic serpentine arrangement around a 3x3 array having nine prime high intensity irradiation locations in the core, which are known as flux traps.[93–95] Additionally, the ATR core is divided into five different operation lobes (four corner lobes and the center lobe), and each of these may be operated at a different power level (within specific limitations) during each reactor cycle. In addition to the nine flux traps, there are 66 irradiation positions inside the core reflector tank and two capsule irradiation tanks outside the core with 34 low-flux irradiation positions.[96] As ATR offers a large number of test positions, the primary operating characteristics have been provided in Table 1.1.[97]

**Table 1.1.**     **ATR General Characteristics**[97]

| Reactor: | |
|---|---|
| Maximum thermal power | 250 MW(Th)[a] |
| Maximum power density | 1.0 MW/L |
| Maximum thermal neutron flux | $1.0 \times 10^{15}$ n/cm$^2$-sec[b] |
| Maximum fast flux | $5.0 \times 10^{14}$ n/cm$^2$-sec[b] |
| Number of flux traps | 9 |
| Number of experiment positions | 77[c] |
| **Core:** | |
| Number of fuel assemblies | 40 |
| Active length of assemblies | 1.2 m (4 feet) |
| Number of fuel plates per assembly | 19 |
| **Reactor Coolant:** | |
| Operating pressure | 2.5 Mpa (360 psig) |
| Design temperature | 115°C (240°C) |
| Light water maximum coolant flow | 3.09 m$^3$/s (49,000 gpm) |
| Coolant temperature (operating) | <52°C (125°F) inlet, 71°C (160°F) outlet |

a. Maximum design power. ATR typically operates near the 110 MW(Th) level.
b. Parameters are based on the full 250 MW(Th) power level and will be proportionally reduced for lower reactor power levels
c. Only 70 of the 77 are potentially available for experiments.
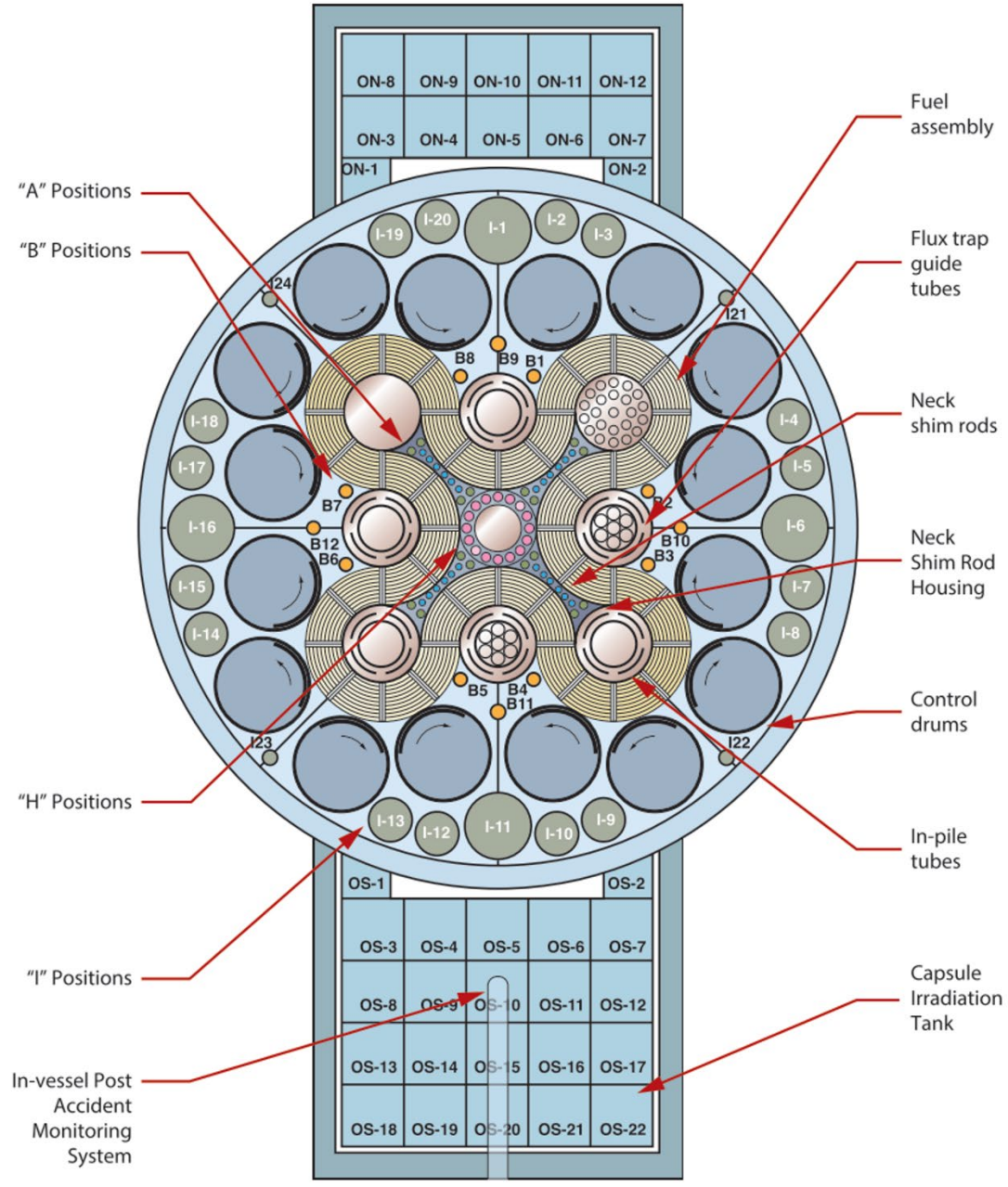
**Figure 1.7    Core cross-section of Advanced Test Reactor.**[97]

The ATR is a versatile test reactor that can accommodate a variety of test assembly configurations.[96] A brief overview of the experiment capabilities within ATR is provided below. More information regarding these tests may be found in the ATR user guide.[97]

1. *Hydraulic Shuttle Irradiation System Experiment*:[96] This system allows irradiations of small capsules in selected positions within the Large B Position of the reactor to support materials research, rapid activations, and isotope production. Utilizing this type of experiment affords researchers the ability to insert and remove specimens while the ATR is in operation. The maximum amount of material allowed for the experiments is 25 grams, and up to 14 shuttle capsules can be tested to form a "train" to be inserted into ATR at one time.

2. *Static capsule experiment*:[98] The most simple type of irradiation test at ATR. Sealed, typically self-contained experiment encapsulations with an inert gas surrounding the irradiation specimens. For those experiments that are not sealed, experiment specimens can come in contact with the primary reactor coolant to minimize the risk of achieving excessive temperatures during irradiation. Instrumentation for these types of experiments typically include passive monitors of melt wires for peak temperature monitoring and flux wires for neutron fluence. The main advantage of utilizing a static capsule experiment is the ease of removal from and replacement into the reactor vessel.

3. *Instrumented lead experiment*:[92] This type of irradiation test is a step up in complexity from static capsule experiments. This type of experiment incorporates active instrumentation for continuous monitoring and control of specific experiment parameters during irradiation to provide a real time display of experiment parameters. The experiment capsule for these experiments is similar to that of the static capsule experiment but requires the incorporation of an umbilical tube that connects the experiment to a control system outside of the reactor vessel. Parameters that can be

monitored are temperature for temperature control through a gas feedback system that will provide the necessary gas cooling mixture to the experiments to achieve the desired experiment conditions. Also, the gas composition can be monitored to elucidate any changes in experiment conditions.

4. *Pressurized water loop experiment*: This is the most complex and comprehensive type of irradiation test provided at ATR.[87] Within the ATR core, six of the nine ATR flux traps contain in-pile tubes that are connected to pressurized water loops, and provide a barrier between the reactor primary coolant and a secondary pressurized water loop coolant system. Within the secondary cooling system are pumps, coolers, ion exchangers, heaters to control experiment temperature, and chemistry control systems. All of these parameters are continuously monitored during an irradiation experiment to provide the most precise monitoring and control of experiment parameters during irradiation. Additionally, continuous monitoring of these parameters provides insight towards specimen performance during irradiation.

### 1.2.1.1.2 Transient Reactor Test Facility

According to the United States Nuclear Regulatory Commission (U.S.NRC) a transient event is one where a change in the reactor coolant system temperature, pressure, or both, is attributed to a change in the reactors power output. Furthermore, transients can be caused by adding or removing neutron poisons, by increasing or decreasing electrical load on the turbine generator, or with accident conditions. These changes can be brief in duration or reactor condition changes could be instantaneous.[99] TREAT is housed at the INL, and was one of the first reactor facilities built to enable nuclear transient testing by providing a facility in which the core meltdown problem could be studied in-pile.[100] The

first criticality was achieved in 1959, and after hosting numerous irradiation experiments, it was placed in standby mode in 1994.[101] In 2017 efforts to restart TREAT were initiated, and in 2018 they were completed with the main focus of supporting the critical development and characterization of accident tolerant fuel that can tolerate power-cooling mismatches better than current fuels. Furthermore, accident toleration fuels were a fuel form mandated by Congress following the events at Fukushima.[86,102]

This is a unique research reactor (**Figure 1.8**), as it is an air-cooled, pulsed, and graphite moderated reactor capable of safely generating very large integrated bursts of thermal neutrons over a large sample volume.[99] The reactor has 350 4-inch by 4-inch by 8 foot Zircaloy fuel assemblies that contain one part of high-enriched uranium to 10,000 parts graphite, and is capable of producing up to 20 gigawatts thermal for a transient pulse that can last up to 100 msec.[102] Additionally, it is capable of variable power and variable temperature computer-controlled transients lasting a minute or more.[103]

The graphite-uranium fuel composition provides unique capabilities because it produces a large negative reactivity temperature coefficient, and it is this large negative temperature coefficient that gives TREAT its characteristic ability to allow for flexibility in experimental conditions and techniques to enable rapid heating that would lead to the destruction of mockups of fast reactor fuel elements *under controlled conditions*, without harm to the reactor itself.[100] The transient testing of nuclear fuel is a proactive effort in preparation for the worst nuclear reactor scenarios, as it is designed to test for and establish the highest safety standards.[102] More specifically, these efforts are to ensure that the entire nuclear energy system can be operated safely. The restart of TREAT brought

back significant transient testing capabilities to the United States and gives further

evidence of the commitment to safety in operations for nuclear power applications.
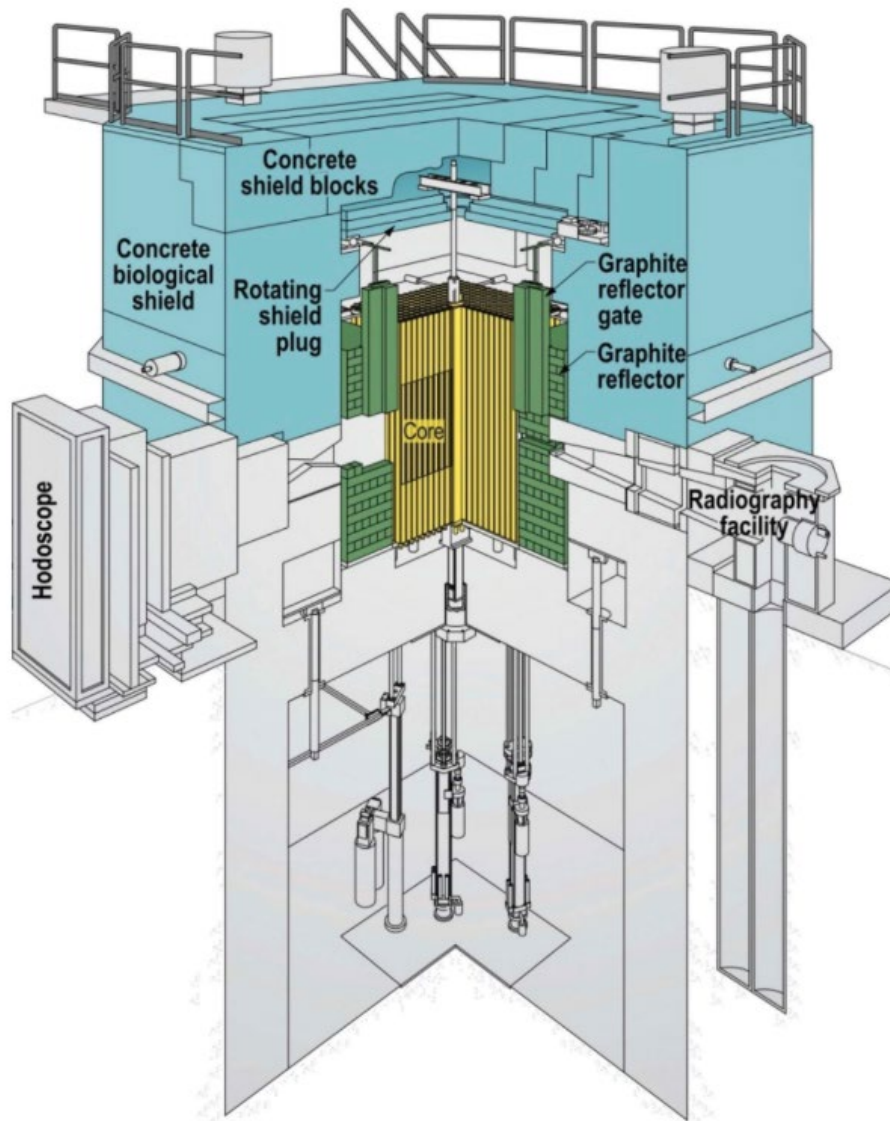


**Figure 1.8    Isometric overview of TREAT features (three-quarters section view).**[104]

This facility is used to study fuel melting behavior, interactions between fuel and coolant, and the potential for propagation of failure to adjacent fuel pins under conditions ranging from mild upsets to severe accidents.[99] The TREAT facility's transient operations are capable of, but not limited to, steady-state operations, shaped transients (including ramp reactivity insertion and preheated transients), natural pulses (also known as temperature-limited transients), and clipped pulses, where control rod movement reduces the total energy deposition as compared to an equivalent reactivity insertion for a natural transient.[105] Additionally, it has shown the ability to provide a reactor profile similar to one that occurs during a loss-of-coolant accident.[106] Basic capabilities and key instrument capabilities include:[107]

- Ability to produce 2500 MJ of energy

- High intensity (20 GW), short duration (<100 ms) neutron pulses for severe accident testing.

- Shaped transients at intermediate powers and times (flexible power shapes up to several minutes in duration).

- 120 kW steady state operation

- Testing capability for static capsules, sodium loops and water loops

- Neutron-radiography facility

- The ability to perform nondestructive examination of assemblies up to 15 feet long in steady state operating mode by neutron radiography

- Neutron hodoscope providing real-time imaging of fuel motion during testing

- Open core design suitable to instrument experiments during testing

Currently, computational modeling campaigns are underway to establish a method to provide 3-D modeling capabilities and to predict the amount of energy deposited in an irradiation experiment during a power excursion, along with its axial distribution.[108] As these factors are dependent a large number of different variables including (but not limited to): core configuration, the experiment vehicle design, instrumentation and containment, the nature of the fuels sample or samples themselves, coolant/moderator, control rod positions and motion history, and temperature changes during the transient. [108] With the lack of 3-D modeling capabilities prior to being placed in standby mode, it was impossible to predict energy deposition in a test sample before an experiment. To validate 3-D simulations, experiments targeted towards physics measurements to provide 3-D temperature, 3-D flux, fission wire and spectral measurements must be performed, and current efforts within advanced manufactured in-pile sensors have significant potential to support these activities.

### 1.2.1.2 Passive Peak Temperature Monitoring in MTRs

A key parameter during irradiation tests is temperature. Temperature monitoring is currently accomplished through both passive- and active-monitoring techniques.[94] Active-monitoring techniques, such as thermocouples, provide real-time data and are typically expensive because they require the implementation of instrumentation leads. On the other hand, passive-monitoring techniques are typically used in static irradiation capsules, and can provide insight toward peak temperatures.[109] For those instances where irradiation tests are seeking a less-expensive measurement method and/or the experiment requires instrumentation without leads such as static capsule experiments, passive techniques are the preferred method for temperature monitoring.[87]

Melt wires are a passive monitoring technique that enables experimenters to identify the peak temperature achieved during an irradiation test.[110] This method involves placing wires that have both a known composition and well-characterized melting temperature within an experimental test rig designed for materials testing. The peak test temperature is then inferred during post-test examination or post-irradiation examination (PIE) as the wire is inspected for visual signs of melting. If the material shows signs of melting it can then be reasoned that the peak temperature during testing exceeded the melting point of melt wire material. On the other hand, it is determined that the peak test temperature remained below the melting point of the wire material if the wire does not show signs of melting. Currently the method for selecting materials includes the identification of those materials having a low neutron-absorption cross-section while exhibiting distinct and reproducible melting behavior when they have been exposed to temperatures beyond their respective melting point.

Current state-of-the art for melt wires can be referred to as classical melt wires, and these melt wires have been matured through a meticulous material selection process and the development of validation procedures. The process for classical melt-wire fabrication includes the ability to encapsulate multiple wire materials into one small-diameter unit.[111] The library of qualified materials for melt-wire selection contains more than 40 useful materials with a detection range between 29.73 and 1535°C.[111] Wire materials are chosen based on expected irradiation test temperatures and required resolution.[110] While classical melt wires are commonly used in test-reactor experiments, such as those conducted in the Advanced Test Reactor (ATR), some test designs have limited space due to predesigned capsules that may only be a couple of millimeters in

diameter. As multiple specimens are contained within the capsules at once, this can leave little or no space for passive and / or active instrumentation. Additional limitations of classical melt wires are in their temperature resolution, as large gaps between identifiable peak temperatures currently exist (**Fig. 1.9**).

**MATERIALS AND MELTING TEMPERATURES IN INL LIBRARY**

| Material (wt% of components) | Melt Onset, °C |
|---|---|
| 56.2Bi 33.8Pb 10Sn | 85.0 |
| 65Bi35In | 110.6 |
| 55.2Bi 44.8Pb | 126.4 |
| 57Bi43Sn | 139.4 |
| 100Sn | 231.8 |
| 95Sn/5Sb | 238.6 |
| 90Pb/10Sb | 252.4 |
| 80Au 20Sn | 279.5 |
| 90Pb 7.5Sn 2.5Ag | 290.0 |
| 97.5Pb5Ag5Sn | 302.9 |
| 97.5Pb2.5Ag | 304.0 |
| 97.5Pb1 .75Sn 1.75Ag | 309.3 |
| 100Pb | 327.5 |
| 100Zn | 419.6 |
| 80Sb20Zn | 507.8 |
| 100Al | 660.5 |
| 49Ag16Cu23Zn7.5Mn4.5Ni | 681.3 |
| 40Ti20Zr20Cu20Ni | 850.7 |
| 98.2Cu1.8Be | 865.1 |
| 100Ge | 938.3 |
| 82Au 18Ni | 955.0 |
| 100Ag | 961.9 |
| 65Cu35Au | 995.6 |
| 100Au | 1064.0 |
| 100Cu | 1084.6 |
| 70Cu30Ni | 1191.0 |
| 28Mo69Ni2Fe1Co1Cr | 1370.0 |
| 100Ni | 1455.0 |

Δ 92.4 °C (between 57Bi43Sn and 100Sn)
Δ 152.7 °C (between 80Sb20Zn and 100Al)
Δ 169.4 °C (between 49Ag16Cu23Zn7.5Mn4.5Ni and 40Ti20Zr20Cu20Ni)
Δ 176 °C (between 70Cu30Ni and 28Mo69Ni2Fe1Co1Cr)

**Figure 1.9**     **Current library of materials available for classical melt wires.**[111]

To demonstrate the utility and novelty afforded with the incorporation of additive manufacturing techniques for the fabrication of melt wires various AM methods will be used to develop and test miniaturized melt arrays having better temperature resolution than their classical counterparts.

### 1.2.1.3 Flux Foils for Reactor Metrology

Neutron flux sensors are required for reactor dosimetry, as they can be used to determine is the determination of the energy dependent neutron flux within a reactor during a given time, which is a critical input for safe operation and for material evaluation experiments in MTRs.[112] Accurate detection of in-core neutron activity is needed to evaluate tests being conducted at facilities such as the Advanced Test Reactor



**Figure 1.10    From *Unruh, T. et al*, Representative current state-of-the-art activation wires and foils**

(ATR) and Transient Test Reactor Test Facility (TREAT).  Currently, passive methods are used to measure the neutron spectrum of an experiment location after the sample has been removed from the reactor. Determination of neutron flux during an irradiation experiment is based on the understanding that each isotope has a different neutron sensitivity, interaction and cross-section. A flux wire or foil is fabricated using a material of known composition and mass that is placed in a neutron field and later characterized and correlated to the integral incident neutron exposure.[113]  For an irradiation experiment,

a variety of materials having different neutron sensitivities as a function of neutron energy are used **(Fig. 1.10)**.

Post irradiation examination of neutron activation foils includes gamma-ray spectrometry using a high-purity germanium detector, which is then used to calculate number of fissions or the activity per gram of each irradiated flux wire by counting the gamma-rays emitted in characteristic peaks using Eq.(1), where the parameters are defined in Table 1.2.[106]

$$A = \frac{\lambda C e^{\lambda t_d}}{\eta \varepsilon g m (1 - e^{-\lambda t_r}}$$
Eq.(1)

**Table 1.2      Parameters used for Flux Foil/wire Fission Calculations**

| Variable | Description |
|---|---|
| A | Activity per gram of parent isotope (Bq/g) |
| $\lambda$ | Decay constant (sec$^{-1}$) |
| $\varepsilon$ | Absolute efficiency of detector at photopeak energy |
| $\eta$ | Quantum yield of gamma-ray per disintegration |
| C | Counts in photopeak for radionuclide |
| g | Self-shielding factor |
| m | Mass of parent isotope (g) |
| $t_r$ | Real counting time (sec) |
| $t_d$ | Decay time between beginning of irradiation to beginning of detector measurement (sec) |

Disadvantages of classical neutron flux foils and wires include:

1.  They can only detect thermal or fast fluence

2. They require post irradiation analysis

3. Passive technique

4. Does not allow for directional flux measurements in reactors where neutron flux is

   non-uniform.

Additive manufacturing of neutron flux foils stands to reduce cost and enhance performance by exploring unique geometries and miniaturization of these activation foils with these methods. More specifically, the development of advanced manufactured dosimeters will target the fourth disadvantage, by introducing the ability to perform directional flux measurements.

To evaluate the utility of additive manufacturing for neutron flux dosimeter fabrication requires that the neutron response of additively manufactured foils be compared to those created from their bulk counterparts. Foil/wire activation is based on the formation of a radioisotope by neutron capture, and this interaction can be predicted with well-known neutron absorption cross-sections. Active detection of neutrons is difficult, which requires that secondary charged particles by elastic scattering, inelastic scattering, or transmutation, which are detected by counting the gamma and beta particles produced during transmutation.[114] Generally, the cross-section is higher for thermal neutrons than for fast neutrons, and the characteristics of the thermal neutron flux field is best described as an ideal gas of neutrons whose kinetic energy spectrum is determined by the temperature. Like that of an ideal gas, the velocities of the particles are described by a Maxwell-Boltzmann distribution, which has been well characterized for U-235.[114,115]

Currently inks created with nanoparticle dispersions of materials whose bulk counterparts are known to have with a variety of neutron energy sensitivities (thermal,

epithermal and fast) are available. Initial materials evaluation will be performed by using two different additive manufacturing techniques of DLP to produce unique substrate and encapsulation geometries and DWT for the fabrication of neutron flux foils.

<u>1.2.2 Space Exploration</u>

Like the inside of a nuclear reactor, space is another environment classified as extreme. This is due to the extremes in temperature, both hot and cold, it being near vacuum, and the large amount of high energy radiation present in space. However, as we continue efforts here to preserve the Earth and its natural resources, other efforts are looking to build a new future in space. In 2005, the NASA Authorization Act was endorsed by Congress which included guidance from the Vision for Space Exploration. In 2006, NASA worked with 13 of the world's space agencies to develop the Global Exploration Strategy, and the United States announced plans to return to the Moon to set up a base with the Lunar Architecture announcement.[116]

> *The Global Exploration Strategy resulted in themes, and these*
>
> *crystallized into six themes, and that includes extending sustained*
>
> *presence, human presence on the Moon, international collaboration,*
>
> *the Moon's usefulness as a unique laboratory, economic advancement*
>
> *and technological innovation that will be important to space*
>
> *exploration as well as benefitting people here on Earth, preparing for*
>
> *future human and robot missions to Mars and other destinations, and*
>
> *also pursuing a vibrant exploration program that will engage and*
>
> *inspire and educate the public, bringing hope to young and old alike.*
>
> *-NASA Deputy Administrator Shana Dale (2006)*

### 1.2.2.1 Structural Health Monitoring of Inflatable Habitats

Structural mass is one of the biggest challenges that NASA faces in achieving its deep space exploration goals.[117] To support space exploration activities, inflatable and deployable structures that utilize soft structural textiles are practical and promising candidates for a variety of applications including solar sails, antennas, space suits, and they are especially promising for use in developing Lunar and Mars habitats.[117–119] Soft structural textiles that are lightweight with high strength, such as Kevlar and Vectran, are of particular interest to the space industry for inflatable habitats, parachutes and decelerating systems. The advantages of these technical textiles over traditional structural materials such as metal alloys and rigid composites are found in the significant mass and volume savings that they provide.[120] Benefits aside, complexities emerge from the need to incorporate non-destructive/non-invasive testing methods for structural health monitoring (SHM) which requires monitoring systems capable of measuring very high rates of strain.[121] The high rates of strain result in breakage of typical strain gauges, which are designed for use with metals. Beyond being designed for more rigid strain monitoring applications, typical resistive strain gauges show hysteresis over time and cannot hold a signal for long periods of time. SHM systems for inflatable habitats, parachutes and decelerating systems are used to ensure the safety of crewmembers, aim to establish an emergency notification system, and enable smart entry, descent and landing (EDL) operations.

Design requirements for SHM systems for these applications (provided by NASA Johnson Space Center) would provide continuous and real time monitoring of strain/load to detect, diagnose and locate damage both in real time and after incident. Additional

constraints for these strain gauges include the need to elongate up to 25% of original length, they must show the ability to cycle a minimum of 20 times showing no signs of hysteresis or loss of signal. Finally, these devices must fit within a 1 in. x 1 in. dimensions.

Focusing on the development of a flexible strain monitoring device capable of withstanding the high rates of strain will support structural health monitoring applications that extend beyond those for deep space exploration missions. Inflatable habitats or structural members are known to have military, disaster relief and aerospace applications, as these structures significant load carrying capacity and can be packaged into a relatively small volume and raised quickly.[120,122,123]

### 1.3 Objectives

In this dissertation, we investigated the feasibility of incorporating AM methods for the development of sensors and instrumentation for applications within extreme environments such as those found in nuclear and aerospace industries. This will enable the acceleration, modernization and enhanced functionality of the nuclear and aerospace industries sensors and instrumentation; in-turn enhancing the safety and efficiency of nuclear reactors while also enhancing our ability to monitor strain/load of soft structural materials to diagnose and locate damage both in real time and after incident. The main objectives of this project are to integrate additive manufacturing methods for the development of advanced sensors and instrumentation for the nuclear and aerospace industries from the following:

1. The development of strain sensors for use with soft structural materials capable of withstanding high strain loads while exhibiting minimal hysteresis

to address technology gaps in structural health monitoring for inflatable habitats.

2. The development of passive AM sensors for detection of peak temperature to enhance the temperature resolution while facilitating an expansion of the irradiation experiments and designs that these passive monitors can be integrated in through device miniaturization.

3. The development of advanced manufactured dosimeters to advance the capabilities of neutron dosimeters used in reactor dosimetry to enable directional flux monitoring within the reactor core, which cannot be accomplished with classical neutron dosimeters due to geometry constraints.

Additive manufacturing will enable the development of miniaturized, robust and high-fidelity sensors necessary to collect detailed data to characterize fuels and materials intended for use in extreme conditions. The following includes exploratory work to investigate the use of innovative techniques to support advancement in the nuclear and aerospace industries, which has served to open the door of possibilities for advanced manufactured sensors for applications in extreme environments.

### 1.4 Dissertation Outline

The subsequent chapters of this dissertation include my first author publications (Chapters 2-4) followed by a conclusion (Chapter 5), which provides a summary of the work and suggests some potential future directions for the work. To elaborate, Chapter 2 contains our first demonstration of a sensor fabricated for extreme environments within the aerospace industry. In this study we develop an AJP fabricated capacitive strain gauge for structural health monitoring of inflatable habitats to support space exploration

missions. Such habitats require structural health monitoring systems that are not temperature sensitive, are capable of withstanding high strain loading, and do not exhibit hysteresis over time. Static, dynamic and cyclic loading of AJP flexible capacitance based strain gauges were tested at high strain loads on Kevlar webbing and their performance was compared to that of their resistance based counterparts.

Chapter 3 turns the focus from the aerospace industry to another industry associated with having extreme environments, nuclear energy. In this chapter, development efforts to facilitate the integration of AM to advance the peak temperature technology available for in-pile applications is detailed. For this work, advanced manufactured melt wires were fabricated with the use of AJP to demonstrate the potential for enhancing the temperature resolution of melt wires while also enabling the integration of melt wires within even more radiation experiments from significant device miniaturization efforts afforded through additive manufacturing techniques.

Chapter 4, keeps the sensor application within the nuclear industry, but shifts focus with a study on the development of advanced manufactured dosimeters that provided for the first time the ability to monitor directional flux within the Transient Reactor Test Facility. Chapter 5 presents the conclusions of this dissertation by providing a high-level summary of the research efforts contained within chapters 2 to 4, and also provides potential activities for future research/work within the area of additive manufacturing of sensors for extreme environments.

## 1.5 References

1. King, B. H. & Renn, M. J. Aerosol Jet® Direct Write Printing for Mil-Aero Electronic Applications. *WHITEPAPER - Optomec* (2008). at <http://166.21.32.80/data/assets/ssc/atc/2009-04-09article.pdf%5Cnhttp://www.optomec.com/downloads/Optomec_Aerosol_Jet_Direct_Write_Printing_for_Mil_Aero_Electronic_Apps.pdf>

2. Paulsen, J. A., Renn, M., Christenson, K. & Plourde, R. Printing conformal electronics on 3D structures with aerosol jet technology. *FIIW 2012 - 2012 Futur. Instrum. Int. Work. Proc.* 47–50 (2012). doi:10.1109/FIIW.2012.6378343

3. ISO/ASTM International. ISO/ASTM 52900: Additive manufacturing - General principles and Terminology. *Int. Stand.* **5,** 1–26 (2015).

4. Lu, B., Li, D. & Tian, X. Development Trends in Additive Manufacturing and 3D Printing. *Engineering* **1,** 085–089 (2015).

5. Gandhiraman, R. P., Jayan, V., Han, J. W., Chen, B., Koehne, J. E. & Meyyappan, M. Plasma jet printing of electronic materials on flexible and nonconformal objects. *ACS Appl. Mater. Interfaces* **6,** 20860–20867 (2014).

6. Chen, M. Y., Lu, X., Subbaraman, H. & Chen, R. T. Fully printed phased-array antenna for space communications. *Micro- Nanotechnol. Sensors, Syst. Appl.* **7318,** 731814 (2009).

7. Mondal, K., Fujimoto, K. & McMurtrey, M. Non-visual analysis of miniaturized melt wire arrays for in-pile measurement of peak irradiation temperature. (2020). at <https://www.osti.gov/servlets/purl/1668675/>

8. Mondal, K., Fujimoto, K. & McMurtrey, M. D. Advanced Manufacturing of Printed Melt Wire Chips for Cheap, Compact Passive In-Pile Temperature Sensors. *Jom* **72,** 4196–4201 (2020).

9. Rahman, M. T., McCloy, J., Ramana, C. V. & Panat, R. Structure, electrical characteristics, and high-temperature stability of aerosol jet printed silver nanoparticle films. *J. Appl. Phys.* **120,** (2016).

10. Park, S. H. & Kim, H. S. Flash light sintering of nickel nanoparticles for printed electronics. *Thin Solid Films* **550,** 575–581 (2014).

11. Paulsen, J. A., Renn, M., Christenson, K. & Plourde, R. Printing conformal electronics on 3D structures with aerosol jet technology. *FIIW 2012 - 2012 Futur. Instrum. Int. Work. Proc.* 47–50 (2012). doi:10.1109/FIIW.2012.6378343

12. Joo, M., Lee, B., Jeong, S. & Lee, M. Laser sintering of Cu paste film printed on polyimide substrate. *Appl. Surf. Sci.* **258,** 521–524 (2011).

13. Danaei, R., Varghese, T., Ahmadzadeh, M., McCloy, J., Hollar, C., Sadeq Saleh, M., Park, J., Zhang, Y. & Panat, R. Ultrafast Fabrication of Thermoelectric Films by Pulsed Light Sintering of Colloidal Nanoparticles on Flexible and Rigid Substrates. *Adv. Eng. Mater.* **21,** 1–6 (2019).

14. Rahman, M. T. & Panat, R. Aerosol jet 3D printing and high temperature characterization of nickel nanoparticle films. *Manuf. Lett.* **29,** 5–10 (2021).

15. Rahman, M. T., Cheng, C. Y., Karagoz, B., Renn, M., Schrandt, M., Gellman, A. & Panat, R. High Performance Flexible Temperature Sensors via Nanoparticle Printing. *ACS Appl. Nano Mater.* **2,** 3280–3291 (2019).

16. Chang, Y. T., Hung, K. Y., Young, H. T., Li, K. M. & Chen, R. K. Aerosol jet printing of nickel oxide nanoparticle ink with ultraviolet radiation curing for thin-film temperature sensors. *Int. J. Adv. Manuf. Technol.* **118,** 1957–1965 (2022).

17. Filippidou, M. K., Tegou, E., Tsouti, V. & Chatzandroulis, S. A flexible strain sensor made of graphene nanoplatelets/polydimethylsiloxane nanocomposite. *Microelectron. Eng.* **142,** 7–11 (2015).

18. Liu, R., Ding, H., Lin, J., Shen, F., Cui, Z. & Zhang, T. Fabrication of platinum-decorated single-walled carbon nanotube based hydrogen sensors by aerosol jet printing. *Nanotechnology* **23,** (2012).

19. Zhao, D., Liu, T., Zhang, M., Liang, R. & Wang, B. Fabrication and characterization of aerosol-jet printed strain sensors for multifunctional composite structures. *Smart Mater. Struct.* **21,** (2012).

20. Rahman, M. T., Rahimi, A., Gupta, S. & Panat, R. Microscale additive manufacturing and modeling of interdigitated capacitive touch sensors. *Sensors Actuators, A Phys.* **248,** 94–103 (2016).

21. Fapanni, T., Sardini, E., Serpelloni, M. & Tonello, S. 3D Electrochemical Sensor and Microstructuration Using Aerosol Jet Printing. *Sensors* **21,** (2021).

22. Optomec. AEROSOL JET Materials FAQs. 2 (2017). at <http://www.optomec.com>

23. Wilkinson, N. J., Smith, M. A. A., Kay, R. W. & Harris, R. A. A review of aerosol jet printing—a non-traditional hybrid process for micro-manufacturing. *Int. J. Adv. Manuf. Technol.* **105,** 4599–4619 (2019).

24. Alhendi, M., Sivasubramony, R. S., Weerawarne, D. L., Iannotti, J., Borgesen, P. & Poliks, M. D. Assessing Current-Carrying Capacity of Aerosol Jet Printed Conductors. *Adv. Eng. Mater.* **22,** 1–9 (2020).

25. Ramamurti, R., Gandhiraman, R. P., Lopez, A., Doshi, P., Nordlund, D., Kim, B. & Meyyappan, M. Atmospheric pressure plasma printing of nanomaterials for IoT applications. *IEEE Open J. Nanotechnol.* **1,** 47–56 (2020).

26. Dey, A., Lopez, A., Filipič, G., Jayan, A., Nordlund, D., Koehne, J., Krishnamurthy, S., Gandhiraman, R. P. & Meyyappan, M. Plasma jet based in situ reduction of copper oxide in direct write printing . *J. Vac. Sci. Technol. B* **37,** 031203 (2019).

27. Pandhi, T., Cornwell, C., Fujimoto, K., Barnes, P., Cox, J., Xiong, H., Davis, P. H., Subbaraman, H., Koehne, J. E. & Estrada, D. Fully inkjet-printed multilayered graphene-based flexible electrodes for repeatable electrochemical response. *RSC Adv.* **10,** 38205–38219 (2020).

28. Ali, S., Hassan, A., Hassan, G., Bae, J. & Lee, C. H. All-printed humidity sensor based on gmethyl-red/methyl-red composite with high sensitivity. *Carbon N. Y.* **105,** 23–32 (2016).

29. Moya, A., Gabriel, G., Villa, R. & Javier del Campo, F. Inkjet-printed electrochemical sensors. *Curr. Opin. Electrochem.* **3,** 29–39 (2017).

30. Liew, Q. J., Aziz, A. S. A., Lee, H. W., Lee, M. W., Hawari, H. F. & Md Khir, M. H. Inkjet-Printed Flexible Temperature Sensor Based on Silver Nanoparticles Ink. 3 (2020). doi:10.3390/ecsa-7-08216

31. Zhang, Y., Anderson, N., Bland, S., Nutt, S., Jursich, G. & Joshi, S. All-printed strain sensors: Building blocks of the aircraft structural health monitoring system. *Sensors Actuators, A Phys.* **253,** 165–172 (2017).

32. Correia, V., Caparros, C., Casellas, C., Francesch, L., Rocha, J. G. & Lanceros-Mendez, S. Development of inkjet printed strain sensors. *Smart Mater. Struct.* **22,** (2013).

33. Vasiljevic, D. Z., Mansouri, A., Anzi, L., Sordan, R. & Stojanovic, G. M. Performance Analysis of Flexible Ink-Jet Printed Humidity Sensors Based on Graphene Oxide. *IEEE Sens. J.* **18,** 4378–4383 (2018).

34. FernÃindez-Ramos, M. D., Pageo-Cabrera, M., CapitÃin-Vallvey, L. F. & Pãrez De Vargas-Sansalvador, I. M. Inkjet-printed O2gas sensors in intelligent packaging. *Analyst* **146,** 3177–3184 (2021).

35. Ali, S., Khan, S. & Bermak, A. Inkjet-Printed Human Body Temperature Sensor for Wearable Electronics. *IEEE Access* **7,** 163981–163987 (2019).

36. Tan, H. W., Tran, T. & Chua, C. K. A review of printed passive electronic components through fully additive manufacturing methods. *Virtual Phys. Prototyp.* **11,** 271–288 (2016).

37. Martin, G. D. & Hutchings, I. M. Fundamentals of Inkjet Technology. *Inkjet Technol. Digit. Fabr.* 21–44 (2012). doi:10.1002/9781118452943.ch2

38. Lan, L., Zou, J., Jiang, C., Liu, B., Wang, L. & Peng, J. Inkjet printing for electroluminescent devices: emissive materials, film formation, and display prototypes. *Front. Optoelectron.* **10,** 329–352 (2017).

39. Shi, J. & Wagih, M. Flexible Direct-Write Printed RF Sensor for RF Ice Sensing. *FLEPS 2021 - IEEE Int. Conf. Flex. Printable Sensors Syst.* 0–3 (2021). doi:10.1109/FLEPS51544.2021.9469841

40. Dong, Y., Min, X. & Kim, W. S. A 3-D-Printed Integrated PCB-Based Electrochemical Sensor System. *IEEE Sens. J.* **18,** 2959–2966 (2018).

41. Dudala, S., Srikanth, S., Dubey, S. K., Javed, A. & Goel, S. Rapid inkjet-printed miniaturized interdigitated electrodes for electrochemical sensing of nitrite and taste stimuli. *Micromachines* **12,** 1–13 (2021).

42. Sappati, K. K. & Bhadra, S. Printed Polymer based Acoustic Sensor for Temperature Monitoring. *FLEPS 2020 - IEEE Int. Conf. Flex. Printable Sensors Syst.* 2020–2023 (2020). doi:10.1109/FLEPS49123.2020.9239521

43. Chen, Y. & Bhadra, S. A Flexible Printed Potentiometric Sensor for Potassium Ion Sensing. *FLEPS 2021 - IEEE Int. Conf. Flex. Printable Sensors Syst.* 33–36 (2021). doi:10.1109/FLEPS51544.2021.9469790

44. Lu, B. H., Lan, H. B. & Liu, H. Z. Additive manufacturing frontier: 3D printing electronics. *Opto-Electronic Adv.* **1,** 1–10 (2018).

45. Shen, A., Kim, S. B., Bailey, C., Ma, A. W. K. & Dardona, S. Direct Write Fabrication of Platinum-Based Thick-Film Resistive Temperature Detectors. *IEEE Sens. J.* **18,** 9105–9111 (2018).

46. Aga, R. S., Webb, T. M., Pandhi, T., Aga, R., Estrada, D., Burzynski, K. M., Bartsch, C. M. & Heckman, E. M. Laser-defined graphene strain sensor directly fabricated on 3D-printed structure. *Flex. Print. Electron.* **6,** (2021).

47. La, T. G., Qiu, S., Scott, D. K., Bakhtiari, R., Kuziek, J. W. P., Mathewson, K. E., Rieger, J. & Chung, H. J. Two-Layered and Stretchable e-Textile Patches for Wearable Healthcare Electronics. *Adv. Healthc. Mater.* **7,** 1–11 (2018).

48. Izak, P., Mastalska-Poplawska, J. & Stempkowska, A. Modification of the rheological properties of screen printing ceramic paints containing gold. *J. Phys. Conf. Ser.* **790,** 012011 (2017).

49. Yan, L. K. Q., Tam, S. K., Fung, K. Y. & Ng, K. M. Product design: Formulation of a screen-printable sintering-type conductive paste. *AIChE J.* **66,** 1–16 (2020).

50.  Chua, C. K., Yeong, W. Y., Hong, Y. L., Tran, T. & Ong, W. T. *3D Printing and Additive Manufacturing of Electronics: Principles and Applications*. (World Scientific Seris in 3D Printing, 2021).

51.  Gonzalez-Gutierrez, J., Cano, S., Schuschnigg, S., Kukla, C., Sapkota, J. & Holzer, C. Additive manufacturing of metallic and ceramic components by the material extrusion of highly-filled polymers: A review and future perspectives. *Materials (Basel).* **11,** (2018).

52.  Datar, A. Micro-extrusion Process Parameter Modeling. (2012).

53.  Gomez, F. in *Encycl. Astrobiol.* (eds. Gargaud, M., Irvine, W. M., Amils, R., Cleaves, H. J. (Jim), Pinti, D. L., Quintanilla, J. C., Rouan, D., Spohn, T., Tirard, S. & Viso, M.) 828–830 (Springer Berlin Heidelberg, 2015). doi:10.1007/978-3-662-44185-5_566

54.  Busby, J. T., Nanstad, R. K., Stoller, R. E., Feng, Z. & Naus, D. J. Materials degradation in light water reactors: life after 60. *ORNL Report, ORNL/TM-2008/170* 1–11 (2008).

55.  Bogue, R. Sensors for extreme environments. *Sens. Rev.* **32,** 267–272 (2012).

56.  Fahrner, W. R., Job, R. & Werner, M. Sensors and smart electronics in harsh environment applications. *Microsyst. Technol.* **7,** 138–144 (2001).

57.  Balint, T. S., Kolawa, E. A., Cutts, J. A. & Peterson, C. E. Extreme environment technologies for NASA's robotic planetary exploration. *Acta Astronaut.* **63,** 285–298 (2008).

58.  Tjong, S. C. Novel nanoparticle-reinforced metal matrix composites with enhanced mechanical properties. *Adv. Eng. Mater.* **9,** 639–652 (2007).

59.  Yadav, M. C. Role of Sensors (Nano) in Nuclear Technology. *J. Phys. Conf. Ser.* **1198,** (2019).

60. Pandhi, T., Kreit, E., Aga, R., Fujimoto, K., Sharbati, M. T., Khademi, S., Chang, A. N., Xiong, F., Koehne, J., Heckman, E. M. & Estrada, D. Electrical Transport and Power Dissipation in Aerosol-Jet-Printed Graphene Interconnects. **8,** 1–10 (2018).

61. Zinkle, S. J. & Was, G. S. Materials challenges in nuclear energy. *Acta Mater.* **61,** 735–758 (2013).

62. Ahmed Simon, A., Badamchi, B., Subbaraman, H., Sakaguchi, Y., Jones, L., Kunold, H., J. van Rooyen, I. & Mitkova, M. Introduction of Chalcogenide Glasses to Additive Manufacturing: Nanoparticle Ink Formulation, Inkjet Printing, and Phase Change Devices Fabrication. *Sci. Rep.* **11,** 1–15 (2021).

63. Fujimoto, K. & Mcmurtrey, M. *Development of Bismuth and Platinum Bi-Metallic Nanoparticles to Enhance Melt Wire Temperature Resolution*. (2021). at <https://inldigitallibrary.inl.gov/sites/sti/sti/Sort_47429.pdf>

64. Hollar, C., Lin, Z., Kongara, M., Varghese, T., Karthik, C., Schimpf, J., Eixenberger, J., Davis, P. H., Wu, Y., Duan, X., Zhang, Y. & Estrada, D. High-Performance Flexible Bismuth Telluride Thin Film from Solution Processed Colloidal Nanoplates. *Adv. Mater. Technol.* **5,** 1–8 (2020).

65. Menyah, K. & Wolde-Rufael, Y. CO2 emissions, nuclear energy, renewable energy and economic growth in the US. *Energy Policy* **38,** 2911–2915 (2010).

66. Yoro, K. O. & Daramola, M. O. *CO2 emission sources, greenhouse gases, and the global warming effect. Adv. Carbon Capture* (Elsevier Inc., 2020). doi:10.1016/b978-0-12-819657-1.00001-3

67. Myhrvold, N. P. & Caldeira, K. Greenhouse gases, climate change and the transition from coal to low-carbon electricity. *Environ. Res. Lett.* **7,** (2012).

68. Rosa, E. A. & Dietz, T. Human drivers of national greenhouse-gas emissions. *Nat. Clim. Chang.* **2,** 581–586 (2012).

69. Schurer, A. P., Cowtan, K., Hawkins, E., Mann, M. E., Scott, V. & Tett, S. F. B. Interpretations of the Paris climate target. *Nat. Geosci.* **11,** 220–221 (2018).

70. IEA. Net Zero by 2050 A Roadmap for the. 222 (2021). at <www.iea.org/t&c/%0Awww.iea.org/t&c/no need for>

71. Bragg-Sitton, S. M., Boardman, R., Rabiti, C. & O'Brien, J. Reimagining future energy systems: Overview of the US program to maximize energy utilization via integrated nuclear-renewable energy systems. *Int. J. Energy Res.* **44,** 8156–8169 (2020).

72. Olander, D. Nuclear fuels - Present and future. *J. Nucl. Mater.* **389,** 1–22 (2009).

73. Humphrey, U. E. & Khandaker, M. U. Viability of thorium-based nuclear fuel cycle for the next generation nuclear reactor: Issues and prospects. *Renew. Sustain. Energy Rev.* **97,** 259–275 (2018).

74. Brodsky, M. B., Boyle, D. R. O., Zegler, S. T., Laboratu, L. A. S. & Nelson, R. D. KITTEL, J. E. AYER, W. N. BECK, M. B. BRODSKY, D. R. O'BOYLE, and S. T. ZEGLER. **15,** 373–440 (1971).

75. Zinkle, S. J. & Was, G. S. Materials challenges in nuclear energy. *Acta Mater.* **61,** 735–758 (2013).

76. Murray, R. L. & Holbert, K. E. The History of Nuclear Energy. *Nucl. Energy* 127–141 (2020). doi:10.1016/b978-0-12-812881-7.00008-3

77. Michal, R. Fifty years ago in December : Atomic reactor EBR-I produced first electricity. *Nucl. News* **44,** 28–29 (2001).

78. Haroldsen, R. THE STORY OF THE And the EBR-I Meltdown.

79. IEA. Key World Energy Statistics 2020. (2020). at <https://www.iea.org/reports/key-world-energy-statistics-2020>

80. Locatelli, G., Mancini, M. & Todeschini, N. Generation IV nuclear reactors: Current status and future prospects. *Energy Policy* **61,** 1503–1520 (2013).

81. Was, G. S., Petti, D., Ukai, S. & Zinkle, S. Materials for future nuclear energy systems. *J. Nucl. Mater.* **527,** 151837 (2019).

82. Brook, B. W., Alonso, A., Meneley, D. A., Misak, J., Blees, T. & van Erp, J. B. Why nuclear energy is sustainable and has to be part of the energy mix. *Sustain. Mater. Technol.* **1,** 8–16 (2014).

83. Carmack, J., Goldner, F., Shannon M, B. S. & Snead, L. L. Overview of the U.S. DOE accident tolerant fuel development program. *LWR Fuel Perform. Meet. Top Fuel 2013* **2,** 734–739 (2013).

84. Terrani, K. A. Accident tolerant fuel cladding development: Promise, status, and challenges. *J. Nucl. Mater.* **501,** 13–30 (2018).

85. Calderoni, P., Hurley, D., Daw, J., Fleming, A. & McCary, K. Innovative sensing technologies for nuclear instrumentation. *I2MTC 2019 - 2019 IEEE Int. Instrum. Meas. Technol. Conf. Proc.* **2019-May,** (2019).

86. Pope, C. L., Jensen, C. B., Gerstner, D. M. & Parry, J. R. Transient Reactor Test (TREAT) Facility Design and Experiment Capability. *Nucl. Technol.* **205,** 1378–1386 (2019).

87. Marshall, F. M. Advanced Test Reactor Capabilities and Future Operating Plans. *Variety* **INL/CON-05,** 1–8 (2005).

88. Marshall, F. M., Allen, T. R., Benson, J. B. & Thelen, M. C. Advanced test reactor national scientific user facility partnerships. *Trans. Am. Nucl. Soc.* **105,** 121–122 (2011).

89. Bong Goo, K., Rempe, J. L., Villard, J. F. & Solstad, S. Review of instrumentation for irradiation testing of nuclear fuels and materials. *Nucl. Technol.* **176,** 155–187 (2011).

90. World Nuclear Association. Research Reactors. (2021). at <https://world-nuclear.org/information-library/non-power-nuclear-applications/radioisotopes-research/research-reactors.aspx>

91. Marshall, F. M. Advanced Test Reactor Capabilities and Future Operating Plans. in (2005).

92. Marshall, F. M. & Palmer, A. J. Advanced test reactor national scientific user facility 'new user' experiment. *Trans. Am. Nucl. Soc.* **109,** 235–236 (2013).

93. Grover, S. B. & Furstenau, R. V. The Advanced Test Reactor Irradiation Facilities and Capabilities. *PHYTRA1 First Int. Conf. Phys. Technol. React. Appl.* (2007). at <https://digital.library.unt.edu/ark:/67531/metadc890528/m2/1/high_res_d/91192 2.pdf>

94. Rempe, J. L., Knudson, D. L., Daw, J. E., Condie, K. G. & Curtis Wilkins, S. New sensors for in-pile temperature measurement at the advanced test reactor national scientific user facility. *Nucl. Technol.* **175,** 681–691 (2011).

95. Chang, G. S., Ambrosek, R. G. & Lillo, M. A. ADVANCED TEST REACTOR LEU FUEL CONVERSION FEASIBILITY STUDY ( 2006 Annual Report ) Validation of the Detailed Plate-by-Plate MCNP ATR Full Core Model. (2006).

96. INL. FY 2009 Advanced Test Reactor National Scientific User Facility Users' Guide. *Qual. Assur.* (2009).

97. Grover, S. B. & Marshall, F. M. Advanced Test Reactor. *INL Present.* (1860).

98. Grover, S. B. & Furstenau, R. V. Capabilities and Facilities Available at the Advanced Test Reactor to Support Development of the Next Generation Reactors. *Test* (2005).

99. Woolstenhulme, N. E., Baker, C. C., Bess, J. D., Davis, C. B., Hill, C. M., Housley, G. K., Jensen, C. B., Jerred, N. D., O'Brien, R. C., Snow, S. D. & Wachs, D. M. Capabilities development for transient testing of advanced nuclear fuels at TREAT. *Top Fuel 2016 LWR Fuels with Enhanc. Saf. Perform.* 67–76 (2016).

100. Okrent, D., Dickerman, C. E., Gasidlo, J., O'Shea, D. M. & Schoeberle, D. F. the Reactor Kinetics of the Transient Reactor Test Facility (Treat). (1960). at <http://www.osti.gov/servlets/purl/4117807/>

101. Heath, B. K. & Race, C. C. TREAT Restart Project. *Nucl. Technol.* **205,** 1369–1377 (2019).

102.    Bumgardner, J. D. & Wachs, D. M. Restarting the Transient Reactor Test (TREAT) Facility Reactor for Nuclear Transient Testing Science: A Special Issue of Nuclear Technology. *Nucl. Technol.* **205,** iv–v (2019).

103.    Wachs, D. M. Transient testing of nuclear fuels and materials in the United States. *Jom* **64,** 1396–1402 (2012).

104.    Bess, J. D. & DeHart, M. D. Development of a baseline assessment of treat for modeling and analysis needs. *Trans. Am. Nucl. Soc.* **113,** 1616–1619 (2015).

105.    Holschuh, T., Woolstenhulme, N., Baker, B., Bess, J., Davis, C. & Parry, J. Transient Reactor Test Facility Advanced Transient Shapes. *Nucl. Technol.* **205,** 1346–1353 (2019).

106.    Holschuh, T., Watson, S. & Chichester, D. Metrology for Transient Reactor Characterization Using Uranium Wires. *Nucl. Technol.* **205,** 1336–1345 (2019).

107.    Jensen, C. Transient reactor test facility achieves criticality. *Nature* **183,** 862–863 (1959).

108.    DeHart, M. D., Baker, B. A. & Ortensi, J. Interpretation of energy deposition data from historical operation of the transient test facility (TREAT). *Nucl. Eng. Des.* **322,** 504–521 (2017).

109.    Bong Goo, K., Rempe, J. L., Villard, J. F. & Solstad, S. Review of instrumentation for irradiation testing of nuclear fuels and materials. *Nucl. Technol.* **176,** 155–187 (2011).

110.    Daw, J. E., Rempe, J. L., Knudson, D. L., Unruh, T. C., Chase, B. M., Davis, K. L. & Palmer, A. J. Temperature monitoring options available at the Idaho national laboratory advanced test reactor. *AIP Conf. Proc.* **1552 8,** 970–975 (2013).

111.    Davis, K. L., Knudson, D. L., Daw, J. E., Rempe, J. L. & Palmer, A. J. Melt wire sensors available to determine peak temperatures in ATR irradiation testing. *8th Int. Top. Meet. Nucl. Plant Instrumentation, Control. Human-Machine Interface Technol. 2012, NPIC HMIT 2012 Enabling Futur. Nucl. Energy* **1,** 427–434 (2012).

112. Ballesteros, A., Debarberis, L., Voorbraak, W., Wagemans, J. & D'hondt, P. Open issues in reactor dosimetry. *Prog. Nucl. Energy* **52,** 615–619 (2010).

113. Unruh, T., Chase, B., Rempe, J., Nigg, D., Imel, G., Harris, J., Sherman, T. & Villard, J. F. In-core flux sensor evaluations at the ATR critical facility. *Nucl. Technol.* **187,** 308–315 (2014).

114. Akhlaghi, P., Rafat-Motavalli, L. & Miri-Hakimabad, S. H. The measurements of thermal neutron flux distribution in a paraffin phantom. *Pramana - J. Phys.* **80,** 873–885 (2013).

115. Kapoor, S. S., Ramanna, R. & Rao, P. N. R. Emission of prompt neutrons in the thermal neutron fission of U235. *Phys. Rev.* **131,** 283–296 (1963).

116. Bainbridge, W. S. Motivations for space exploration. *Futures* **41,** 514–522 (2009).

117. Litteken, D. in *58th AIAA/ASCE/AHS/ASC Struct. Struct. Dyn. Mater. Conf.* (American Institute of Aeronautics and Astronautics, 2017). doi:doi:10.2514/6.2017-0426

118. Wang, L., Gupta, S., Loh, K. J. & Koo, H. S. Nanocomposite fabric sensors for monitoring inflatable and deployable space structures. *ASME 2016 Conf. Smart Mater. Adapt. Struct. Intell. Syst. SMASIS 2016* **1,** 1–8 (2016).

119. Gerard Valle, Doug Litteken, T. J. Review of Habitable Softgoods Inflatable Design, Analysis, Testing, and Potential Space Applications. *AIAA Scitech 2019 Forum* 1–15 (2019).

120. Young, A. C., Davids, W. G., Whitney, D. J., Clapp, J. D. & Goupee, A. J. Structural testing and analysis of a braided, inflatable fabric torus structure. *Acta Astronaut.* **139,** 189–200 (2017).

121. Kim, S. R., Kim, J. H. & Park, J. W. Wearable and Transparent Capacitive Strain Sensor with High Sensitivity Based on Patterned Ag Nanowire Networks. *ACS Appl. Mater. Interfaces* **9,** 26407–26416 (2017).

122. Verge, A. S. Rapidly Deployable Structures in Collective Protection Systems. 1–18 (9999).

123.  Zheng, F., Chen, M., Li, W. & Yang, P. Conceptual design of a new huge deployable antenna structure for space application. *IEEE Aerosp. Conf. Proc.* 1–7 (2008). doi:10.1109/AERO.2008.4526312

# CHAPTER TWO: AEROSOL JET PRINTED CAPACITIVE STRAIN GAUGE FOR SOFT STRUCTURAL MATERIALS

This chapter has been published in Nature Partner Journals – Flexible Electronics.

Reference:

Fujimoto, K. T., Watkins, J. K., Phero, T., Litteken, D., Tsai, K., Bingham, T., Ranganatha, K. L., Johnson, B. C., Deng, Z., Jaques, B. & Estrada, D. Aerosol jet printed capacitive strain gauge for soft structural materials. *npj Flex. Electron.* **4,** (2020). https://doi.org/10.1038/s41528-020-00095-4

AEROSOL JET PRINTED CAPACITIVE STRAIN GAUGE FOR SOFT

STRUCTURAL MATERIALS


## 2.1 Abstract

Soft structural textiles, or softgoods, are used within the space industry for

inflatable habitats, parachutes and decelerator systems.  Evaluating the safety and

structural integrity of these systems occurs through structural health monitoring systems

(SHM), which integrate non-invasive/non-destructive testing methods to detect, diagnose,

and locate damage. Strain/load monitoring of these systems is limited while utilizing

traditional strain gauges as these gauges are typically stiff, operate at low temperatures,

and fail when subjected to high strain that is a result of high loading classifying them as

unsuitable for SHM of soft structural textiles. For this work, a capacitance based strain

gauge (CSG) was fabricated via aerosol jet printing (AJP) using silver nanoparticle ink

on a flexible polymer substrate.  Printed strain gauges were then compared to a

commercially available high elongation resistance based strain gauge (HE-RSG) for their

ability to monitor strained Kevlar straps having a 26.7 kN (6 klbf) load. Dynamic, static

and cyclic loads were used to characterize both types of strain monitoring devices.

Printed CSGs demonstrated superior performance for high elongation strain

measurements when compared to commonly used HE-RSGs, and were observed to

operate with a gauge factor of 5.2 when the electrode arrangement was perpendicular to

the direction of strain.

## 2.2 Introduction

Soft structural textiles, also known as softgoods, that are lightweight while also exhibiting high strength are of particular interest to the space industry for inflatable habitats, parachutes and decelerator systems. The advantages of these technical textiles over traditional structural materials such as metal alloys and rigid composites are found in the significant mass and volume savings that they provide.[1] Benefits aside, complexities emerge from the need to incorporate non-destructive/non-invasive testing methods for structural health monitoring (SHM), which requires monitoring systems capable of measuring very high rates of strain.[2] SHM systems for inflatable habitats, parachutes and decelerating systems are used to ensure the safety of crewmembers, aim to establish an emergency notification system, and enable smart entry, descent, and landing (EDL) operations. Ideally, SHM systems for these applications would provide continuous monitoring of strain/load to detect, diagnose and locate damage in real time for continuous monitoring and also after incident.[3]

Detecting mechanical deformations is achieved with a variety of sensing mechanisms such as capacitance, resistance or piezoelectric properties. However, the most widely used strain sensing devices, are resistance-based strain gauges (RSG)[4]. Traditionally, strain gauges are intended for use with metals, they employ relatively stiff substrates, operate most effectively at room temperature before corrections must be incorporated, experience strains under 5%, display hysteresis in long-term testing, and undergo mechanical failure at higher strains.[2–5] When considering soft structural materials strain gauges must be capable of withstanding high rates of strain (5-50%) associated with materials being under high load, but the inherent stiffness of traditional

strain gauges results in device failure, and classifies them as unsuitable for the inspection of soft structural materials.[3,5] Additional limitations of the more popular RSGs are found in the dependence of resistivity upon operating temperature and applied strain.[4,6,7] Dependencies such as this result in a non-linear strain response and device hysteresis caused by variable sensitivity as the gauge factor does not remain constant during testing.[6–8] Finally, the fabrication of traditional strain sensors involves complex preparation processes resulting in high fabrication cost and material waste, which can limit their application and development. Hence, developing strain sensing methods for soft structural materials requires the ability to fabricate devices having high flexibility and a robustness that enables them to withstand harsh environments to include high strain and high temperatures.

Capacitance based strain gauges (CSGs) provide a robust sensing mechanism capable of addressing the performance issues associated with resistivity hysteresis of RSGs. CSGs are largely dependent on geometry changes between the electrodes and the dielectric layer which typically do not suffer permanent plastic deformation during cyclical testing.[2,9] These devices, in general, include parallel-plate capacitors or an interdigitated electrode design.[4,5,10,11] CSGs can be used for many of the same applications as RSGs, and typically display higher gauge factors of 15-30, while also having reduced sensitivity to noise and temperature[2]. Currently, commercial CSGs are available, and typically consist of a parallel plate design restricting strain measurements to those that are perpendicular to the gauge direction, are limited in the geometries they can monitor, or require bulky electromechanical devices for mechanical attachment.[2,12] These issues can be overcome by using CSGs having an interdigitated electrode

design.[13,24] Interdigitated electrodes preserve the advantages associated with CSGs vs RSGs in harsh environments, while also providing a vehicle by which CSGs can integrate directly onto structural components. Previous testing has been conducted on Kevlar webbing with flexible strain gauges and it was concluded that CSGs performed better than RSGs in dynamic and long term loading conditions similar to those that were investigated within this work[3]. Finally, using capacitance as the sensing mechanism makes the sensor more suitable for applications where wireless strain sensor measurements are required.[10,14] This would be tremendously advantageous for SHM during smart EDL operations.

Introducing the flexibility needed for SHM of soft structural materials can be achieved by making use of recent advances in additive manufacturing for printed and flexible electronics. Additive manufacturing techniques such as aerosol jet printing (AJP) are relatively simple and low-cost manufacturing processes that can be used to fabricate flexible CSGs where typical substrates employed for flexible applications include polyimide, polyethylene terephthalate and polydimethylsiloxane.[2,15–18] Printed electronics involve the use of a functional material in the form of a nanoparticle suspension, or ink, that is then deposited onto a flexible polymer backing. After deposition, the solvent and dispersing/capping agents are removed to produce a functional device, which is then attached to either the users clothing or skin. This cross-cutting technology demonstrates significant potential for SHM of soft structural materials as the functionality of these devices are dependent upon their high flexibility, long durability, fast response, fast recovery time and high sensitivity to strain.

The AJP technology is a non-contact deposition based on the atomization of inks to form a fine mist or aerosol that is deposited on a substrate. The aerosol jet process eliminates many of the limitations associated with conventional fabrication methods by introducing the ability to print with a wide range of materials such as metal nanoparticles, carbon nanomaterial, functional ceramics, semiconductors, biological molecules and other functional materials as inks can range from 1-2500 cP.[15,19–23] Additionally, device designs are no longer material or geometry limited as AJP introduces the ability to print on a variety of substrates/surfaces, and provides a wide range of feature sizes that span 10 μm to 5 mm.[24–27]  With the ability to achieve higher print resolutions, AJP has the potential to enhance device sensitivity by maximizing the design space of structural health monitoring systems, and provides a low-cost option for sensor fabrication.[28,29,30]

In this work we report, for the first time, on the response of aerosol jet printed flexible CSGs having an interdigitated electrode design (adapted from Hu *et al.*) targeted for use on soft structural materials.[31] The strain response of these printed gauges was then compared to that of commercially available high elongation resistance-based foil strain gauges (HE-RSG). This comparison was used to evaluate the benefits of utilizing the advanced manufacturing technique of AJP to fabricate a robust and flexible strain gauge, while also serving to validate the advantages of a capacitive sensor for measuring the strain of soft structural materials. Flexible CSGs were fabricated via AJP using silver nanoparticle ink and a flexible polymer substrate to monitor military grade Kevlar webbing under high load as this material is typically used in EDL operations and inflatable habitat structures. However, the focus of this work was towards inflatable habitats. Dynamic, static, and cyclic loads were used to characterize both types of strain

monitoring devices. Printed CSGs demonstrated superior performance for high

elongation strain measurements of Kevlar webbing when under high load when compared

to commonly used HE-RSGs and were observed to operate with a gauge factor of 5.2

when an electrode arrangement perpendicular to the direction of strain was used.

## 2.3 Results and Discussion

2.3.1 Interdigitated Electrode Geometry

      Military grade Kevlar webbing is used for the construction of inflatable habitats

and parachutes, and the ability to measure the strain experienced by these structures is a

challenge for NASA.[3] To produce a capacitive strain gauge, an interdigitated structure

was employed, which operates in a similar manner to having multiple parallel plate

capacitors in series. A schematic representation of the device layout can be found in

**Figure 2.1a**, and an optical image of the actual printed sensor in **Figure 2.1b**.

Capacitance was a result of an interdigitated structure spanning 3.6 cm and 1.6 cm with

50 digit pairs or 100 total electrodes. These specific design parameters were chosen in

order to maximize both the theoretical capacitance and the sensing area.  Additionally,

size limitations were associated with the capabilities of the aerosol jet printing

technology, and the 2.54 cm wide Kevlar webbing. Silver epoxy was used to attach

copper wire leads to the device, and poly methyl methacrylate (PMMA), having a

dielectric constant of 5.70, was used both as a protective layer and as the dielectric

between the electrodes to enhance the device capacitance over what could be achieved if

air served the same function.[20] Finally, Kapton (FPC 5 mil, 125 μm) was selected as the

flexible substrate as it is capable of withstanding elongation that is significantly higher

than the maximum elongation of the Kevlar straps when subjected to maximum loading capacity.[32]
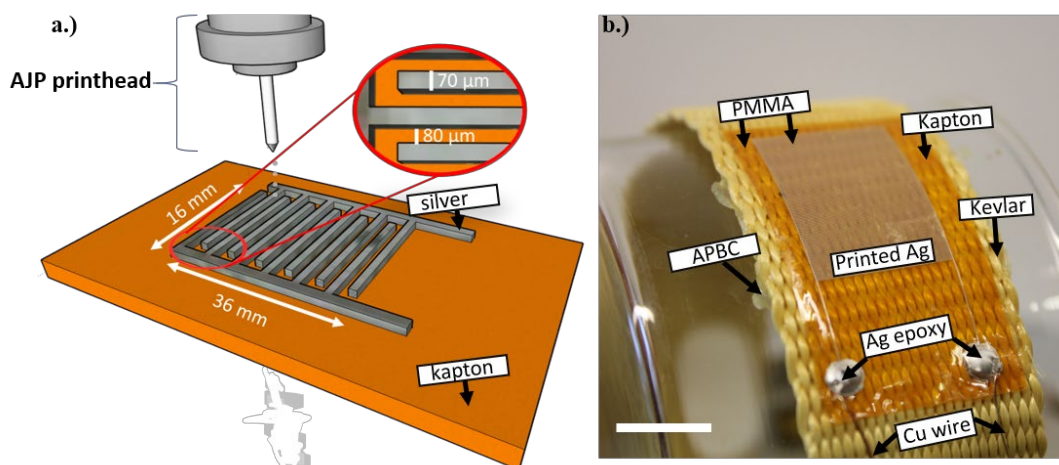


**Figure 2.1.** **Design of printed flexible interdigitated electrode capacitive strain gauge. a.) Schematic representation of the sensor configuration with an interdigitated electrode structure containing 50 digit pairs, b.) Optical image of capacitive strain gauge on Kapton substrate attached to Kevlar strap (scale bar represents 1 cm).**

In **Figure 2.2**, representative higher magnification images of the digits **Figure 2.2a.** center and **Figure 2.2b**. ends along with their respective height profiles shown in Figure **Figure 2.2c**. As depicted, the electrode morphology varies due to the formation of a bulb-like structure at the electrode ends where variation is seen in both height and width. Rahman *et al.* reported the formation of a similar feature at the ends of their printed electrodes while also stating that this change in morphology could be controlled by increasing the printer's shutter speed while using Clariant Prelect TPS 50G2 with the ultrasonic atomizer.[33]

For this study, devices were printed using the pneumatic atomizer for a silver nanoparticle based ink, PvNanoCell Sicrys™ 160PM-116, known for having excellent adhesive properties with a variety of substrates, and near bulk resistivity ($10^{-6}$ $\Omega \cdot$cm). During the printing process the shutter speed is ultimately controlled by the "rapid"

process speed, which controls the speed at which the printer platen moves between depositions. For the fabrication of the CSGs the maximum rapid speed was used, but the formation of the bulb resulted despite modifications to other print parameters such as atomizer, exhaust, and sheath flow rates. This demonstrates that the quality of the print and ultimately the device is dependent upon the ink and atomization process being used.
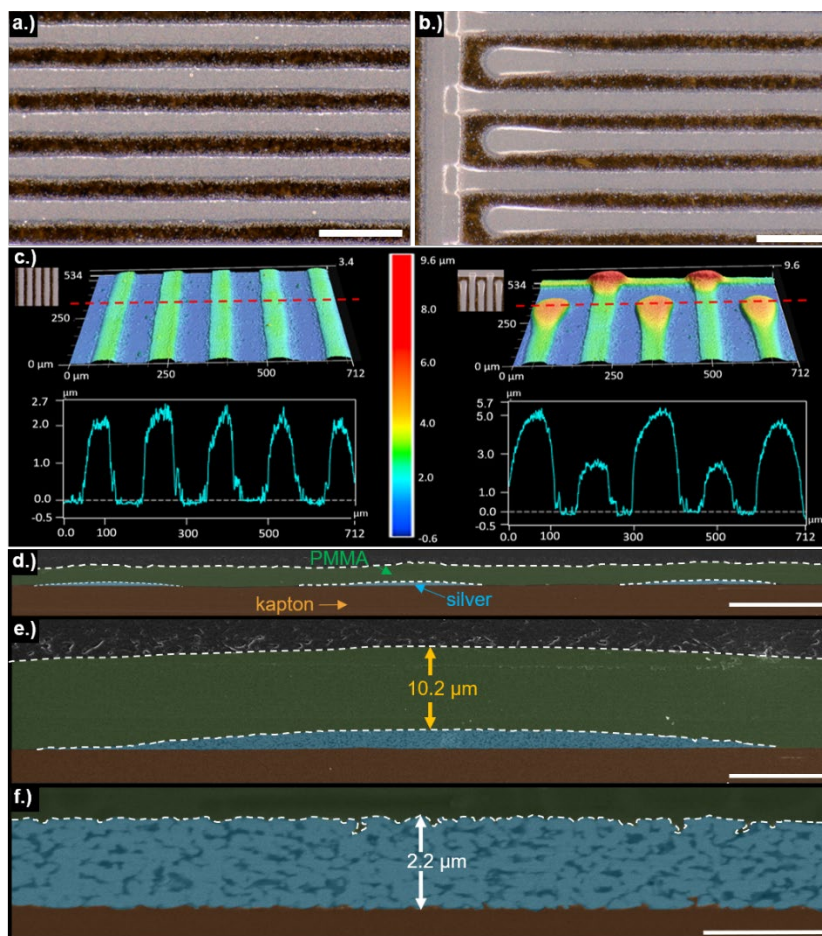


**Figure 2.2.** **Micrographs depicting the morphology of silver lines deposited with aerosol jet printing. a,b.) Optical microscope images of silver strain gauge on polyimide substrate (Scale bar represents 250 μm), and the c.) optical profilometry of AJP deposited silver electrodes on polyimide. Cross-sectional scanning electron microscopy characterization to show d.) silver electrodes representative of AJP deposited strain gauges (scale bar represents 50 μm), e.) PMMA dielectric thickness (scale bar represents 10 μm and f.) printed silver thickness (scale bar represents 2.5 μm).**

2.3.2 CSG Structure

  To further characterize the structure of the printed CSG, cross-sectional SEM was performed to investigate both the quality of the printed CSG and that of the dielectric layer (**Figure 2.2d**.).  Preparing the sample for imaging required the device to be mounted in Quickstick 135 mounting wax prior to slicing with a microtome, and finally the cross-section was carbon coated to minimize surface charging while imaging.  A top-down view of the overspray is provided in **Figure 2.2a**, and a cross-section view is presented in **Figure 2.2e**. with the overspray creating a "tail" on either end of the digit. From **Figure 2.2e.**, the overspray is more pronounced on the left side of the digit, which indicates that $N_2$ flow was not symmetrical through the nozzle and/or the virtual impactor. The PMMA layer was uniform having a thickness of $10.2 \pm 0.1$ µm demonstrating that the drop cast method is an effective way of encapsulating the digits, which is crucial for maximizing the measured capacitance of CSG devices.  The maximum thickness of the digit was $2.7 \pm 0.1$ µm, which is in good agreement with results obtained from stylus profilometry ($2.2 \pm 0.5$ µm).  The cross-section profile shows the porous nature of the printed structure, and with image analysis software the porosity was determined to be $16.1 \pm 0.4\%$ of the total electrode volume.  Gaps/voids providing a porous structure are an inherent feature found within AM devices that is highly dependent upon the ink being printed.[26]

2.3.2.1 Electrical Characterization

  The theoretical initial capacitance, $C_0$, and theoretical strained capacitance, $C_N$, were derived from previous work by Hu *et al.* and Kim *et al.*, and are expressed by[4,31]

$$C_0 = pt(2l - a + 2w)\left(\frac{2n-1}{d}\right)\varepsilon_0 \qquad\qquad (1)$$

$$C_{perpendicular} = pt(1 - ve)((1 - ve)(2l - a + 2w))\left(\frac{2n-1}{d(1+e)}\right)\varepsilon_0 \quad (2)$$

$$C_{parallel} = pt(1 - ve)((1 + ve)(2l - a + 2w))\left(\frac{2n-1}{d(1-e)}\right)\varepsilon_0 \quad (3)$$

where $p$ is dielectric constant of PMMA, $t$ is the thickness of the printed silver

digit, $l$ is the length of the digit, $a$ is the total width of the interdigitated electrodes, $w$ is

the width of the digit, $n$ is the number of digit pairs, $d$ is the spacing between the digits of

the electrodes, e is the strain in the sensitive axis of the strain sensor and $\varepsilon_0$ is the

permittivity of free space. The expected change in capacitance resulting from a strain

incident perpendicular and parallel to electrode orientation is depicted in eq(2) and eq(3),

respectively. Briefly, when the device experiences strain perpendicular to electrode

orientation the spacing between electrodes is expected to increase by a factor of $d_0(1+e)$.

However, due to poisson contraction, it is expected that $a, w$ $and$ $l$ will change by a factor

of (1+ve) from their original values, where v is the poisson ratio of the encapsulating

polymer. For the printed CSGs, the encapsulating material is PMMA with a poisson ratio

of 0.37[34]. With this phenomenon it is expected that as the PMMA is elongated in one

direction it compresses in the two directions perpendicular to the direction of strain.[4] A

schematic detailing the variables used in eq(1) and eq(2) is provided in **Figure 2.3a**, and

the associated dimensions are found within **Figure 2.3b.** From the device dimensions, the

initial capacitance of the printed CSGs is expected to range from 4.56-6.70 pF. However,

the from theoretical capacitance is attributed to the unique geometry of the digit

a.)

b.)

| Symbol | Value |
|--------|-------|
| p | 5.7 |
| t | $2.7 \pm 0.2$ μm |
| w | $71 \pm 4$ μm |
| l | $15.74 \pm 0.02$ mm |
| d | $78 \pm 3$ μm |
| a | $16.07 \pm 0.01$ mm |
| n | 50 |
| $\varepsilon_0$ | $8.85418782 \times 10^{-12}$ F/m |
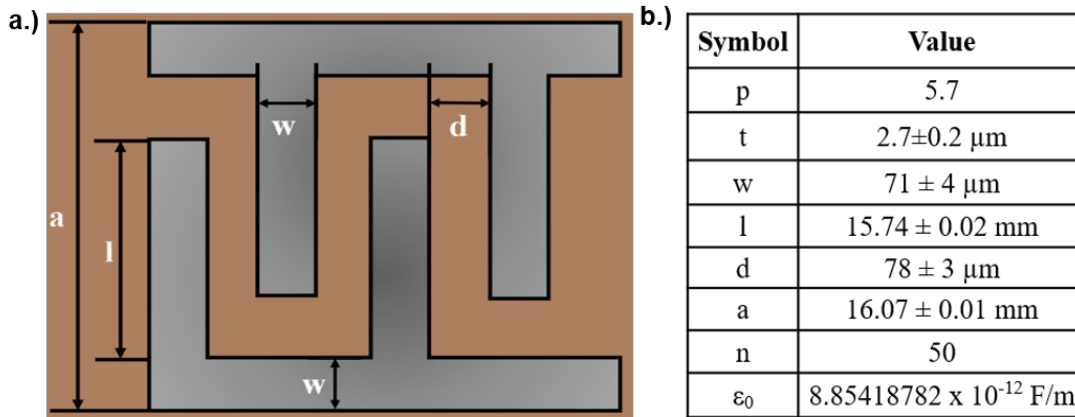
**Figure 2.3.** **Device design parameters for printed CSG interdigitated electrode structure. a.) Schematic detailing the variables to calculate theoretical capacitance, and the b.) values associated with these variables, where dimension values are reported as an average including the standard deviation of measurements representative of the entire device.**

introduced by the printing process, which is evident in **Figure 3.2(a.-e.)** where the

electrode structure with trailing ends associated with overspray is observed in addition to

a porous structure.

Overspray is caused by the smallest droplets within the aerosol, and can be

minimized to some extent by varying the sheath, exhaust, or atomizer flow.[35] However,

overspray, like void formation, is an inherent feature of aerosol jet printed devices and

was found to contribute between 5-25 μm of additional width to the digits. Additionally,

an internal capacitance may exist within the digits themselves which is associated with

the structure voids themselves with air serving as the dielectric. While AJP provides

significant versatility from its compatibility with a broad range of materials, consistency

actual capacitance was measured to range between 42 pF and 15 nF, and the initial

capacitance values for each device can be found in Table 2.1. The significant deviation

and reproducibility are challenges that need to be overcome.  For experienced users,

optimizing print parameters to mitigate these challenges can require extreme measures

which include, but are not limited to, frequent replacement of ink and extensive time spent towards empirical optimization for this sensitive process.[21,23,36–38]

<u>2.3.2.2 Strain Measurements</u>

Capacitance and resistance measurements for printed CSGs and commercial RSGs, respectively, were collected for each sample prior to any load/strain being imparted to the Kevlar strap, and compared to measurements obtained before the samples were mounted into the test system to verify that no damage to the gauge had occurred during transport and setup. For each device that was tested the initial capacitance and resistance measurements can be found in Table 2.1. Final measurements were recorded for each sample at the conclusion of testing after the strain was released and the strap allowed to relax.  However, due to the natural stretch of the Kevlar material the straps did not return to their original dimensions and were permanently elongated after tensile. loading.

**Table 2.1.    Capacitive Strain Gauge Summary of Experiments**

| Device | Device type | Test Type | Electrode Orientation Relative to Strain Direction | $C_0$ or $R_0$ | Figure # |
|---|---|---|---|---|---|
| a | Capacitive | Dynamic, Static | Perpendicular | $46.436 \pm 0.002$ pF | 4a, 4c |
| b | Capacitive | Dynamic, Static | Perpendicular | $15.22 \pm 0.03$ nF | 4a, 4c |
| c | Capacitive | Dynamic, Static | Perpendicular | $9.25 \pm 0.04$ nF | 4a, 4c |
| d | Capacitive | Dynamic, Static | Parallel | $42.51 \pm 0.02$ pF | 4b, 4d |
| e | Capacitive | Dynamic, Static | Parallel | $43.61 \pm 0.02$ pF | 4b, 4d |
| f | Capacitive | Cyclic | Perpendicular | $11.07 \pm 0.03$ nF | 4e |
| g | Capacitive | Cyclic | Perpendicular | $43.57 \pm 0.04$ pF | 4e |
| h | Capacitive | bending | N/A | $6.22 \pm 0.02$ pF | 4f |
| HBM_1 | Resistive | Dynamic, Static | Perpendicular | $353 \pm 2$ Ω | 5a, 5c |
| HBM_2 | Resistive | Dynamic, Static | Perpendicular | $353 \pm 1$ Ω | 5a, 5c |
| HBM_3 | Resistive | Cyclic | Perpendicular | $350$ Ω | 5c |
| HBM_4 | Resistive | Cyclic | Perpendicular | $350$ Ω | 5c |

Printed CSG's exhibited initial capacitance measurements that ranged from ~45 pF to ~15 nF at 10 kHz with a 5 V bias. As the observed range is significant between the printed strain gauges, representative devices from both the pF and nF regime were originally included with both perpendicular and parallel arrangement of electrodes with respect to the direction of strain. However, the device detached during dynamic testing with the representative nF device with electrodes parallel to the direction of strain.

As this work was a result of a collaboration with NASA Johnson Space Center, testing was performed in a manner that was in agreement with previously performed testing procedures[3]. The response of both capacitive and resistive devices was investigated while under dynamic, static, and cyclic loading. Mechanical testing was performed by subjecting the Kevlar webbing to targeted loading conditions rather than strain. This was the method for testing due to the fact that variations in the Kevlar webbing, attributed to the weaving process of these textiles, causes samples subjected to the same loading conditions to exhibit a different strain response between samples.[32] As the webbing is rated according to a maximum loading capacity of 26.7 kN, a peak load of 18.7 kN was selected for dynamic and static testing as it is 70% of the maximum capacity of the Kevlar webbing. Furthermore, cyclic testing was performed at targeting loads of 5.3 kN (1.2 klbf) and 10.7 kN (2.4 klbf) or 20% and 40% of maximum loading capacity of the Kevlar webbing, respectively. The targeted loads for dynamic and static testing resulted in a strain response of > 5%, which still classifies the strain at which these samples were subjected to as relatively high. For reference, a summary of experiments can be found in Table 3.1. Dynamic testing was performed for printed CSGs with electrodes configured perpendicular and parallel to the direction of strain and for HE-

RSGs having electrodes arranged parallel to the direction of strain up to a maximum load

of 18.7 kN (4.2 klbf), which is 70% of the maximum load capacity of the Kevlar webbing

used for testing. Additionally, loading conditions were achieved with a ramp rate of 45

N/sec or (10 lbf/sec). Throughout dynamic testing measurements were collected at 4.4 kN

(1.0 klbf), 8.9 kN (2.0 klbf), 13.3 kN (3.0 klbf), 17.8 kN(4.0 klbf) and 18.7 kN (4.2 klbf).

For CSGs having electrodes arranged perpendicular to the direction of strain an inverse

relationship was observed as depicted in **Figure 2.4a.**, where the MRCC (maximum

relative change in capacitance) was ~20% for devices having a starting capacitance in the

nF regime, and ~3% for a pF starting capacitance. This negative change in capacitance

for electrodes positioned perpendicular to the direction of strain is due to the increasing

elongation of the strap, which increases the distance between the electrodes resulting in a

decrease to the capacitance. The indirect relationship between strain and capacitance was

confirmed through 3D finite element modeling. However, the magnitude of relative

capacitance change is significantly different, and that is attributed to the device features

introduced from the printing process. The results from those efforts can be found in

Appendix A.  During testing, images were captured at each change, targeted load, and/or

time point. Utilizing Digimizer software, and images obtained while testing when

electrodes were perpendicular to the direction of strain, the change in distance between

the top of the first electrode to the bottom of the last electrode from an applied load of

zero to 18.7 kN (4.20 klbF) was determined to be 815 μm. So, as the Kevlar webbing was

under high load, the sensor experienced a strain of 0.037 while the webbing experienced

an average strain of 0.060 ± 0.001. With that, a gauge factor of 5.2 obtained for the

perpendicular orientation with devices having a starting capacitance within the nF
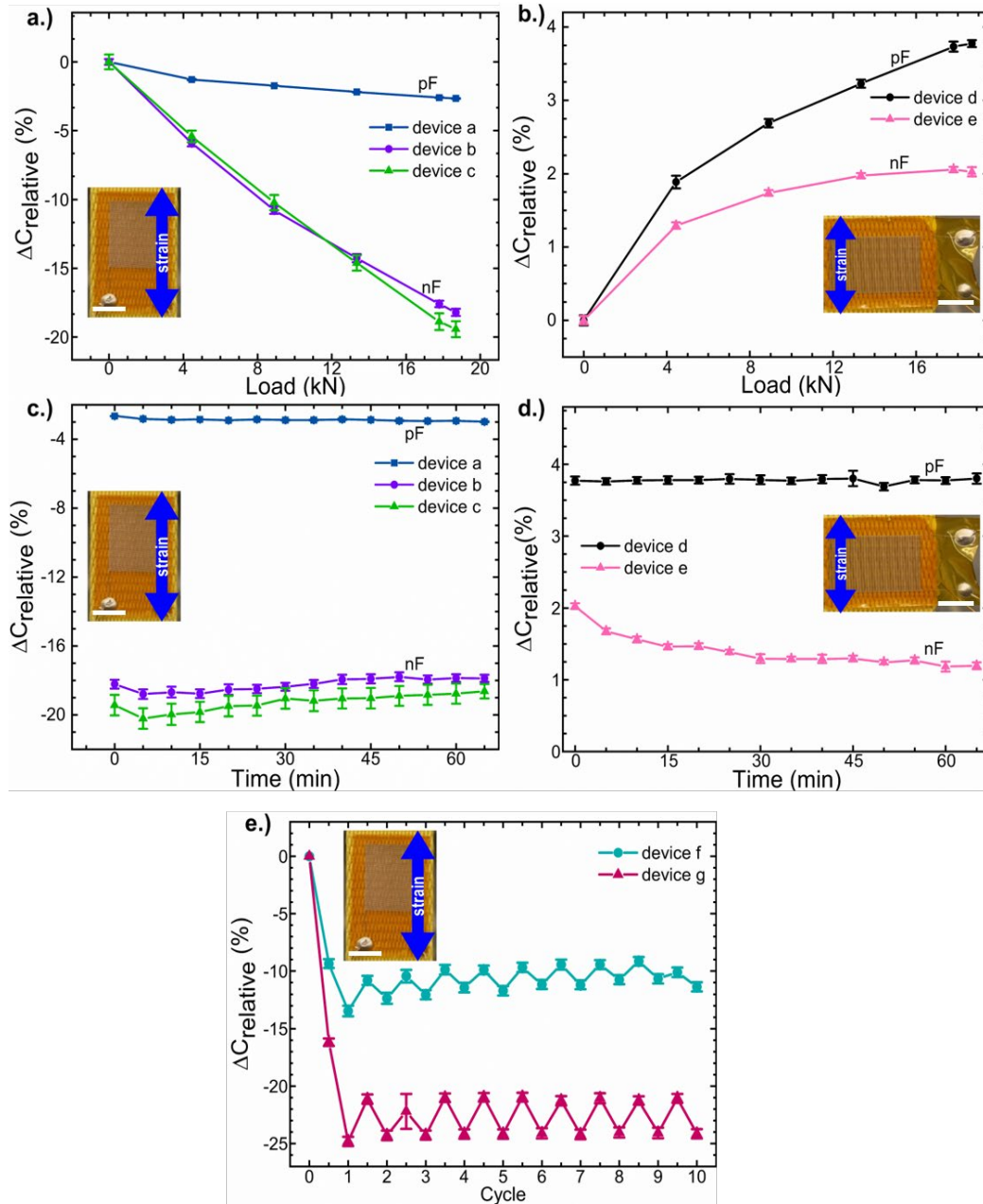
**Figure 2.4.** **Printed capacitance-based strain gauge dynamic, static and cyclic tensile testing results. Relative change in capacitance (%) for printed CSGs where a total of seven different devices were utilized for either dynamic (a-e), static (a-e), or cyclic (f-g) testing. Results for dynamic testing with a target load of 18.7 kN for devices having electrodes a.) perpendicular (devices a-c) and b.) parallel (devices d-e) to the direction of strain. Results for static testing performed at 18.7 kN for those same devices having electrodes c.) perpendicular (devices a-c) and d.) parallel (devices d-e) to the direction of strain, and e.) cyclic testing of two different devices (f-g) having electrodes perpendicular to the direction of strain. Error bars are the estimated experimental uncertainty (Appendix A Discussion). In all images, scale bars represent 1.0 cm.**

range. In contrast, a direct relationship between load and capacitance was observed for devices with electrodes arranged parallel to the direction of strain. As the strap is elongated, and the polyimide substrate is stretched, the spacing between the electrodes is a factor of 2.3 where the MRCC for Device D was 1.6%, and for Device E was 3.7%. Dynamic testing finished immediately after a maximum load of 18.7 kN (4.2 klbF) had been reached, and static testing began. To demonstrate the printed CSGs ability to maintain a signal while under a constant load, the devices were held for a total of 65 minutes with measurements collected in five minute intervals (**Figure 2.4c**). As shown in **Figure 2.4(c.,d.)**, while all devices were able to maintain a signal for the duration of testing, the arrangement with electrodes perpendicular to the direction of strain produced a signal having less hysteresis over the observed timeframe. Finally, cyclic testing was conducted for devices having electrodes arranged perpendicular to the direction of strain by cycling between 5.3 kN (1.2 klbf) and 10.7 kN (4.2 klbf) for a total of ten cycles (**Figure 2.4e**).

For practical application of the printed CSG's it will be necessary to quickly and efficiently obtain the capacitance read out for analysis while minimizing the effects of interference. The ability to accommodate a large capacitance range from printed strain gauges while having a fast and efficient response can be achieved through the use of a digital read out that uses frequency rather than voltage (Please see Appendix A info).

Utilizing the same attachment strategy and testing conditions, the resistance behavior of commercially available HE-RSGs having a similar Kapton backing as the CSGs was investigated to compare and evaluate their suitability for SHM of soft structural materials. For HE-RSGs, per manufacturer instruction, the electrodes were

positioned parallel to the direction of strain. The mechanism for RSG response to strain is explained with the following relationship

$$R = \frac{\rho L}{A}$$

where $R$ is resistance, $\rho$ is a material's resistivity, $L$ is total length foil, and $A$ is the cross-sectional area of the foil. For strain testing of these Kevlar straps, device elongation occurs with strain, and it is expected that the resistance would increase with increasing load. The response of HE-RSGs during dynamic testing is shown in **Figure 2.5a.**, where a direct relationship between resistance and load was observed up to 4.4 kN (1 klbf). While this direct relationship is expected, after the load of 4.4 kN is reached the resistance behavior transitions to an indirect relationship with the applied load at 8.9,13.3,17.8 and 18.7 kN (2, 3, 4, and 4.2 klbf respectively). This behavior indicates that testing conditions may have caused the gauge to exceed its elongation limit, and demonstrates well-known limitations of foil based gauges for high elongation applications.[39,40] For high elongation applications where the plastic elongation conditions are met, the linearity of the strain device can vary as the gauge factor is known to modify using the guideline of 2+ε, where ε is the strain such that the gauge factor at a strain level of 10% is expected to be around 2.1 in tension.[39,33] Immediately after a maximum load of 18.7 kN (4.2 klbf) was achieved with dynamic testing, static testing began for period of 65 minutes (**Figure 2.5b**). Another limitation is revealed during dynamic testing as signal hysteresis is shown to progress over the observed timeframe for all HE-RSG devices, which demonstrates an inability to reliably monitor strain for extended periods of time while under a constant load. Finally, HE-RSGs were subjected to cyclic testing (**Figure 2.5c.**). Cyclic testing provided further support of the aforementioned limitations of HE-

RSGs as similar resistance behavior was observed after the initial target load is achieved,

and signal degradation was apparent for each cycle after equilibrium had been achieved.

The first cycle reveals that an equilibrium must be established prior to conducting strain

measurements as the resistance decreases with the transition from 5.3 kN (1.2 klbf) to

10.7 kN (2.4 klbf). However, the following cycles produce the expected resistance

response where an increase in resistance is observed as the applied load increases, and a

decrease in resistance is observed as the applied also
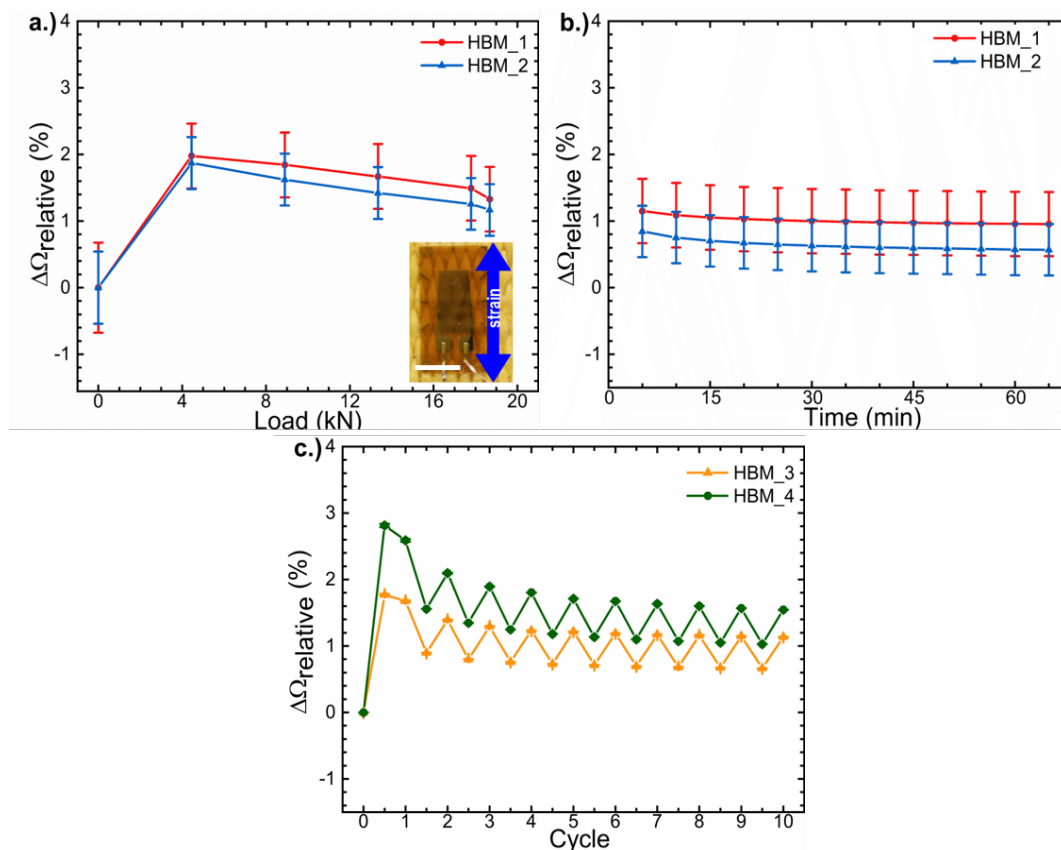


**Figure 2.5.** **Strain response for commercial resistance-based strain gauges. The strain response of commercial RSGs having their electrodes arranged parallel to the direction of strain during a.) dynamic testing with a ramp of 44.5 N/sec, b.) static testing at a load of 18.7 kN and c.) cyclic testing utilizing loads of 5.3 kN and 10.7 kN. Error bars are the estimated experimental uncertainty (Appendix A Discussion). Scale bar**

decreases. Notably, signal hysteresis associated with the HE-RSGs is observed for all three testing conditions and provides evidence that printed CSGs exhibit superior performance with high elongation testing conditions resulting in these devices being considered better suited for SHM for soft structural materials than HE-RSGs.

Finally, variation in initial capacitance values, device response for the first couple of strains, etc., can be compensated for with calibration for the intended application of structural health monitoring of soft structural materials for inflatable habitats. For a crewed, inflatable space habitat, a series of strain sensors would be used in a network for structural health monitoring of the habitat. The sensors would be calibrated on the ground before launch when a precise amount of strain could be applied to the straps. Once the calibration is completed, the strain sensors would be powered off until needed again in space. After launch, deployment, and pressurization, an initial reading would be taken to get a starting strain for the strap material. This strain level would be compared to the levels recorded during the ground calibration testing to ensure no strain changes occurred during the launch phase. While the habitat will stay pressurized during its lifetime, the strain in the straps and in the gage will change over time. This change will be tracked at regular intervals throughout the length of the mission to provide an understanding of the structural health of the habitat.

Initial change during the first couple of strains can be compensated with similar calibration exercises on the ground before launch. The habitat will be testing in the space environment before it's launched and strain changes will be measured. Those strain values are expected to be representative of what would be seen during the initial change in strain once the gages and the habitat are in space. By conducting a series of ground

tests, we can fully understand and predict the behavior of the habitat and the strain

measurement system and use that prediction to compensate the readings in space.

## 2.4 Conclusions

In summary, a capacitive based strain gauge was fabricated via aerosol jet

printing where silver served as the capacitive material and PMMA the dielectric. Printed

CSGs exhibited starting capacitance values ranging from 42 pF to 15 nF. A flexible

substrate, Kapton, was employed to provide the required flexibility for these devices to

withstand high load/strain, and All-purpose Barge Cement served as the adhesive

between the Kapton and the Kevlar strap. Dynamic and static testing was performed for

arrangements where the electrodes were oriented either perpendicular or parallel to the

direction of strain, and the perpendicular arrangement was used for cyclic testing.

Furthermore, HE-RSGs were tested utilizing the same attachment strategy, under the

same conditions, to compare their response to printed CSGs, and to evaluate their

suitability for SHM of soft structural materials. Devices having a starting capacitance in

the nF range demonstrated the highest sensitivity, and a gauge factor of 5.2 was obtained

for those devices having their electrodes arranged perpendicular to the direction of strain.

Finally, printed CSGs were determined to be the better candidates for high elongation

application as they performed better in static situations, dynamic and cyclic events when

compared to commercially available HE-RSGs.

## 2.5 Methods

### 2.5.1 Device Fabrication

The layout of the interdigitated CSG device is shown in **Figure 2.1a**. Device

fabrication began by depositing Sicrys$^{TM}$ 160PM-116 (PV Nanocell) onto a 125 μm thick

DuPont$^{TM}$ Kapton (FPC).  Printing was achieved with the pneumatic atomizer (PA) of an Optomec Aerosol Jet 200 equipped with a 200 µm nozzle. While printing, the ink was held at 23°C to stabilize the ink, and the printed films were heated at 300 °C for 30 min. to remove any residual solvent. The tool platen temperature, nozzle diameter, and pneumatic atomizer, pneumatic exhaust and sheath gas flows were optimized to ensure the line widths and material deposition of functional materials were adequate to obtain conductive traces. Silver epoxy (Epotek, H20E) was used to adhere 30-gauge copper wire to the printed contact pads, and a layer of 950 PMMA A11 (Kayaku Advanced Materials, Inc.) was drop-coated onto the surface of the device to serve as the dielectric. Both the printed CSG and commercially acquired RSG (HBM, Inc., 1-LD20-6/350) devices were attached to Kevlar straps having a maximum loading capacity of approximately 27 kN (6 klbf) with All-Purpose Barge Cement.

## 2.5.2 Characterization

Device imaging and dimensions were obtained by digital microscopy (Keyence VHX-5000), scanning electron microscopy (FEI Teneo Field Emission Scanning Electron Microscopy) and laser microscopy (Keyence VK-Z260K 3D Laser Scanning Confocol Microscope). Additional height profiles were obtained with a Bruker Dektak XT-A Stylus Profilometer fitted with a 2 µm stylus. A Leaic EM UC6 microtome equipped with glass blades was used to produce CSG cross-sections.  Furthermore, cross-sectioning required devices to first be encapsulated in Quickstick 135 mounting wax (Scanning Microscopy Services) prior to slicing.  CSG cross-sections were carbon-coated to prevent charging of the specimen.

2.5.3 Device Attachment

Strain gauges were attached to Kevlar webbing (1991-25.4 mm, Type VI, Class 9) nominally rated at 26.7 kN (6 klbf), and manufactured to Mil-T 87130 manufacturing specifications.  Attaching the gauges to the Kevlar webbing was accomplished with a contact cement known as APBC (All-Purpose Barge Cement; Barge Cements, Inc.). This cement is a polychloroprene based adhesive that is well known for its high strength and flexibility and is typically used in the leather, shoe and prosthetic industries. While the tensile modulus for APBC is not reported or available, polychloroprene is reported to have a tensile modulus of 21 MPa.[41] This is well below the tensile modulus for kapton and kevlar, which indicates that it is well-suited for the intended application. For testing purposes, multiple adhesives were considered including Double/Bubble epoxy, Pliobond 25, DAP Cove Base Zocalo construction adhesive, and GE silicone II caulk.  However, APBC was the only adhesive capable of maintaining the integrity of the bond while under high strain such as that produced while testing Kevlar straps.  Adhering the printed CSGs and RSGs to the Kevlar strap began by applying a thin layer of APBC to both the testing strap and the backside of the printed CSG or RSG. The two items were immediately bonded together with the adhesive sandwiched between the CSG or RSG backing and the strap.  The bond was allowed to cure for 24 hours.

2.5.4 Testing

After the bond was fully cured the Kevlar straps were attached to the webbing grips on the MTS test system by wrapping each end of the strap at least three times around the grip to ensure the strap would not come loose during testing. The grips were positioned such that there was approximately 24" between the base of each grip with the

strain gauge positioned in the center. Samples tested included gauges mounted with electrodes both perpendicular and parallel to the direction of strain resulting in positive and negative changes in capacitance respectively. The leads to the LCR meter were attached and supported to ensure the leads would not come into contact with each other, would not place undue tension on the copper wire attachments, and would remain relatively stable during testing. CSG devices were attached both perpendicular and parallel to the direction of strain while RSG devices were only tested having electrodes parallel to the direction of strain, and both types of devices were attached to Kevlar straps with All-Purpose Barge Cement. Strain testing was performed with an MTS 810 Material Test System equipped with a 100 kN load head, ADMET GRW-50T (Part No. 3218-00225) webbing grips, and FlexTest SE Station Manager software. Capacitance measurements were obtained with an Agilent HP 4284A Precision LCR Meter (10 kHz at 5V), and resistance measurements were obtained with a Keithley 2182A/6220 (-1 to 1 mA), Printed CSG and commercial RSG devices were studied under dynamic, cyclic, and static loads while Kevlar straps were subjected to a maximum load of 18.7 kN (4.2 klbf) during static and dynamic loads at a ramp rate of 45 N/sec (10 lbf/sec). During dynamic testing capacitance measurements were obtained every 4.5 kN (1 klbf) up to the maximum load of 18.7 kN (4.2 klbf), and static loads were held for a total of one hour ten minutes with capacitance measurements taken every five minutes. Additionally, printed CSGs and commercial RSGs were characterized under cyclic loading of 5.3 kN (1.2 klbf) and 10.7 kN (2.4 klbf) for ten total cycles with a ramp rate of 89 N/sec (20 lbf/sec) with capacitance measurements taken at 90 second intervals between each cycle. Macro images of the CSGs were taken in tandem with capacitance measurements in order to

determine the gauge factor for the CSGs. Images were recorded with a Canon EOS 70D digital SLR camera outfitted with a Tamron AF 90mm f/2.8 1:1 macro lens. The camera was held stationary on a tripod and a remote trigger was used to eliminate vibration during image exposure. The ruler imaged next to the CSG during testing was kept in-plane with the device for use in measuring the dimensional change experienced by the CSG at strain. Gauge factor calculations were completed using values for the dimensional changes obtained in conjunction with digital imaging processing software.

## 2.6 Acknowledgements

## 2.7 References

1. Program, N. scientific and technical information. *Technical Report - NASA/CR–2010-216682: Intelligent Flexible Materials for Space Structures.* (2010). at <https://ntrs.nasa.gov/search.jsp?R=20100017479 2019-07-29T22:11:59+00:00Z>

2. Li, J., Longtin, J. P., Tankiewicz, S., Gouldstone, A. & Sampath, S. Interdigital capacitive strain gauges fabricated by direct-write thermal spray and ultrafast laser micromachining. *Sensors Actuators, A Phys.* **133,** 1–8 (2007).

3. Litteken, D. Evaluation of Strain Measurement Devices for Inflatable Structures. in *8th AIAA/ASCE/AHS/ASC Struct. Struct. Dyn. Mater. Conf.* (2017). doi:10.2514/6.2017-0426

4. Kim, S. R., Kim, J. H. & Park, J. W. Wearable and Transparent Capacitive Strain Sensor with High Sensitivity Based on Patterned Ag Nanowire Networks. *ACS Appl. Mater. Interfaces* **9,** 26407–26416 (2017).

5. Cohen, D. J., Mitra, D., Peterson, K. & Maharbiz, M. M. A highly elastic, capacitive strain gauge based on percolating nanotube networks. *Nano Lett.* **12,** 1821–1825 (2012).

6. Amjadi, M., Pichitpajongkit, A., Lee, S., Ryu, S. & Park, I. Highly stretchable and sensitive strain sensor based on silver nanowire-elastomer nanocomposite. *ACS Nano* **8,** 5154–5163 (2014).

7. Andeen, C., Fontanella, J. & Schuele, D. A capacitive gauge for the accurate measurement of high pressures. *Rev. Sci. Instrum.* **42,** 495–496 (1971).

8. Amjadi, M., Kyung, K. U., Park, I. & Sitti, M. Stretchable, Skin-Mountable, and Wearable Strain Sensors and Their Potential Applications: A Review. *Adv. Funct. Mater.* **26,** 1678–1698 (2016).

9. Lipomi, D. J., Vosgueritchian, M., Tee, B. C. K., Hellstrom, S. L., Lee, J. A., Fox, C. H. & Bao, Z. Skin-like pressure and strain sensors based on transparent elastic films of carbon nanotubes. *Nat. Nanotechnol.* **6,** 788–792 (2011).

10. Tsouti, V., Mitrakos, V., Broutas, P. & Chatzandroulis, S. Modeling and Development of a Flexible Carbon Black-Based Capacitive Strain Sensor. *IEEE Sens. J.* **16,** 3059–3067 (2016).

11. Matsuzaki, R. & Todoroki, A. Wireless flexible capacitive sensor based on ultra-flexible epoxy resin for strain measurement of automobile tires. *Sensors Actuators, A Phys.* **140,** 32–42 (2007).

12. Glass, S. W., Fifield, L. S., Sriraman, A. & Bowler, N. Inter-digital capacitive sensor for evaluating cable insulation through jacket. *19th Int. Conf. Environ. Degrad. Mater. Nucl. Power Syst. - Water React. EnvDeg 2019* **020024,** 852–858 (2019).

13. Zeiser, R., Fellner, T. & Wilde, J. Capacitive strain gauges on flexible polymer substrates for wireless, intelligent systems. *J. Sensors Sens. Syst.* **3,** 77–86 (2014).

14. Lynch, J. P. A Summary Review of Wireless Sensors and Sensor Networks for Structural Health Monitoring. *Struct. Heal. Monit.* **38,** 91–128 (2006).

15. Cao, C., Andrews, J. B. & Franklin, A. D. Completely Printed, Flexible, Stable, and Hysteresis-Free Carbon Nanotube Thin-Film Transistors via Aerosol Jet Printing. *Adv. Electron. Mater.* **3,** 1700057 (2017).

16. Cheng, M. Y., Lin, C. L., Lai, Y. T. & Yang, Y. J. A polymer-based capacitive sensing array for normal and shear force measurement. *Sensors (Switzerland)* **10,** 10211–10225 (2010).

17. Wang, F. X., Lin, J., Gu, W. B., Liu, Y. Q., Wu, H. Di & Pan, G. B. Aerosol-jet printing of nanowire networks of zinc octaethylporphyrin and its application in flexible photodetectors. *Chem. Commun.* **49,** 2433–2435 (2013).

18. Obata, K., Schonewille, A., Slobin, S., Hohnholz, A., Unger, C., Koch, J., Suttmann, O. & Overmeyer, L. Hybrid 2D patterning using UV laser direct writing and aerosol jet printing of UV curable polydimethylsiloxane. *Appl. Phys. Lett.* **111,** 121903 (2017).

19. Feng, J. Q. & Renn, M. J. Aerosol Jet ® Direct-Write for Microscale Additive Manufacturing . *J. Micro Nano-Manufacturing* **7,** 011004 (2019).

20. Wilkinson, N. J., Smith, M. A. A., Kay, R. W. & Harris, R. A. A review of aerosol jet printing—a non-traditional hybrid process for micro-manufacturing. *Int. J. Adv. Manuf. Technol.* (2019). doi:10.1007/s00170-019-03438-2

21. Secor, E. B. Principles of aerosol jet printing. *Flex. Print. Electron.* **3,** (2018).

22. Folgar, C. E., Suchicital, C. & Priya, S. Solution-based aerosol deposition process for synthesis of multilayer structures. *Mater. Lett.* **65,** 1302–1307 (2011).

23. Mahajan, A., Frisbie, C. D. & Francis, L. F. Optimization of aerosol jet printing for high-resolution, high-aspect ratio silver lines. *ACS Appl. Mater. Interfaces* **5,** 4856–4864 (2013).

24. Paulsen, J. A., Renn, M., Christenson, K. & Plourde, R. Printing conformal electronics on 3D structures with aerosol jet technology. *FIIW 2012 - 2012 Futur. Instrum. Int. Work. Proc.* 47–50 (2012). doi:10.1109/FIIW.2012.6378343

25. Hedges, M., Borras, A. & Services, M. N. 3D Aerosol Jet ® Printing-Adding Electronics Functionality to RP/RM. in *DDMC 2012 Conf.* 1–5 (2012).

26. Pandhi, T., Kreit, E., Aga, R., Fujimoto, K., Sharbati, M. T., Khademi, S., Chang, A. N., Xiong, F., Koehne, J., Heckman, E. M. & Estrada, D. Electrical Transport and Power Dissipation in Aerosol-Jet-Printed Graphene Interconnects. *Sci. Rep.* **8,** 1–10 (2018).

27. Deiner, L. J. & Reitz, T. L. Inkjet and Aerosol Jet Printing of Electrochemical Devices for Energy Conversion and Storage. *Adv. Eng. Mater.* **19,** 1600878 (2017).

28. Madou, M. J. in *Manuf. Tech. Microfabr. Nanotechnol.* 509–567 (CRC Press, 2011).

29. Morales-Rodriguez, M. E., Joshi, P. C., Humphries, J. R., Fuhr, P. L. & McIntyre, T. J. Fabrication of low cost surface acoustic wave sensors using direct printing by aerosol inkjet. *IEEE Access* **6,** 20907–20915 (2018).

30. Sethumadhavan, V., Saraf, S. & Chaudhari, A. Development of printable electronic materials for low cost flexible sensor fabrication. in *Proc. - 2017 IEEE Int. Conf. Electr. Instrum. Commun. Eng.* (2017). doi:10.1109/ICEICE.2017.8192449

31. Hu, C. F., Wang, J. Y., Liu, Y. C., Tsai, M. H. & Fang, W. Development of 3D carbon nanotube interdigitated finger electrodes on polymer substrate for flexible capacitive sensor application. *Nanotechnology* **24,** 1–14 (2013).

32. Selig, M. M., Valle, G. D., James, G. H., Oliveras, O. M., Jones, T. C. & Doggett, W. R. Creep burst testing of a woven inflatable module. in *2nd AIAA Spacecr. Struct. Conf.* (2015). doi:10.2514/6.2015-1625

33. Rahman, M. T., Rahimi, A., Gupta, S. & Panat, R. Microscale additive manufacturing and modeling of interdigitated capacitive touch sensors. *Sensors Actuators, A Phys.* **248,** 94–103 (2016).

34. MatWeb. Overview of Materials for Acrylic, General Purpose, Molded. at <http://www.matweb.com/search/DataSheet.aspx?MatGUID=3cb08da2a0054447a3790015b7214d07&ckck=1>

35. Verheecke, W., Van Dyck, M., Vogeler, F., Voet, A. & Valkenaers, H. Optimizing aerosol jet® printing of silver interconnects on polyimide film for embedded electronics applications. in *8th Int. DAAAM Balt. Conf. "INDUSTRIAL Eng.* 373–379 (2012). at <http://www.davidlu.net/Verheecke.pdf>

36. Chen, G., Gu, Y., Tsang, H., Hines, D. R. & Das, S. The Effect of Droplet Sizes on Overspray in Aerosol-Jet Printing. *Adv. Eng. Mater.* **20,** 1701084 (2018).

37. Salary, R. (Ross), Lombardi, J. P., Samie Tootooni, M., Donovan, R., Rao, P. K., Borgesen, P. & Poliks, M. D. Computational Fluid Dynamics Modeling and Online Monitoring of Aerosol Jet Printing Process. *J. Manuf. Sci. Eng.* **139,** 021015 (2016).

38. Gu, Y., Gutierrez, D., Das, S. & Hines, D. R. Inkwells for on-demand deposition rate measurement in aerosol-jet based 3D printing. *J. Micromechanics Microengineering* **27,** 097001 (2017).

39.     VPG. *High-Elongation Strain Measurements Tech Tip TT-605. Strain Gages and Instruments* (2015).

40.     Tony R. Kuphaldt. *Strain gauges. HBM Strain Gauges* (2008).

41.     Ames. *Polychlorprene Rubber - neoprene datasheet. Polychloroprene Rubber - neoprene datasheet* (2020). at <http://www.amesrubberonline.com/pdf/polychloroprene-neoprene.pdf>

CHAPTER THREE: ADDITIVE MANUFACTURING OF MINIATURIZED PEAK

TEMPERATURE MONITORS FOR IN-PILE APPLICATIONS

This chapter has been published in MDPI-Sensors

Reference:

Fujimoto, K. T., Hone, L. A., Manning, K. D., Seifert, R. D., Davis, K. L.,

Milloway, J. N., ... & Estrada, D. (2021). Additive Manufacturing of Miniaturized

Peak Temperature Monitors for In-Pile Applications. *Sensors*, *21*(22), 7688.

https://doi.org/ 10.3390/s21227688

ADDITIVE MANUFACTURING OF MINIATURIZED PEAK TEMPERATURE

MONITORS FOR IN-PILE APPLICATIONS

### 3.1 Abstract

Passive monitoring techniques have been used for peak temperature measurements during irradiation tests by exploiting the melting point of well-characterized materials. Recent efforts to expand the capabilities of such peak temperature detection instrumentation include the development and testing of additively manufactured (AM) melt wires. In an effort to demonstrate and benchmark the performance and reliability of AM melt wires, we conducted a study to compare prototypical standard melt wires to an AM melt wire capsule, composed of printed aluminum, zinc, and tin melt wires. The lowest melting-point material used was Sn, with a melting point of approximately 230 °C, Zn melts at approximately 420 °C, and the high melting-point material was aluminum, with an approximate melting point of 660 °C. Through differential scanning calorimetry and furnace testing we show that the performance of our AM melt wire capsule was consistent with that of the standard melt-wire capsule, highlighting a path towards miniaturized peak-temperature sensors for in-pile sensor applications.

### 3.2 Introduction

For over a century burning fossil fuels has provided most of the energy required to heat our homes, power industry, drive our cars, and light up our cities. Within the United States alone, 85% of total energy comes from oil, coal, and natural gas.[1] While fossil fuel based energy consumption continues to increase alongside the world's population, growing concern over limited fossil fuel supplies and the accumulating

greenhouse gases in the Earth's atmosphere have triggered a transition from using fossil fuels as our main energy source to those that are more sustainable and environmentally responsible.[2] Of the clean energy sources available there is only one zero-carbon technology capable of meeting most, if not all, of the energy demands of a modern society, and that is nuclear power. Severe reactor accidents such as Fukushima Daiichi Nuclear Power Plant (2011) have emphasized the need to enhance accident tolerance in nuclear plants and prompted developments in advanced fuels and more robust structural materials capable of enhancing safety and efficiency in operations.[3] Nuclear energy has had a declining share in global electricity markets., and if nuclear energy is to realize a global impact in clean energy production and reduced carbon emissions, innovations in nuclear technology are needed to extend the life of current light-water reactors and expedite the development of generation IV nuclear reactors.[4–6]

On a fundamental level, safety in nuclear reactor operations requires an in-depth understanding of how advanced nuclear fuels and structural materials behave within a reactor environment.[7] The development, demonstration and qualification of advanced reactor materials is expected to facilitate an accelerated deployment of advanced reactor technologies, and this requires a greater understanding of the irradiation effects on fuels and material behaviors.[8] Furthermore, this understanding is critical for the assessment of potential materials for any nuclear reactor concept to ensure safety, reliability and efficiency in operations. This understanding is typically acquired with the use in-pile (i.e., in-core or in-reactor) sensors deployed as part of experiments in Materials Test Reactors (MTRs). MTRs such as the Advanced Test Reactor (ATR) and the Transient Reactor Test Facility at the Idaho National Laboratory use specialized irradiation capsules equipped

with in-pile instrumentation for targeted property measurements within the extreme environment of a nuclear reactor core.[9–11] Current in-pile instrumentation efforts look to assess, verify, and increase the precision of measurements under irradiation with the development of advanced sensors capable of monitoring temperature, physiochemical conditions, neutron flux/dose, pressure, and multi-physics field properties. To maximize time, resources, and data collection, advanced and miniaturized instrumentation is needed to accurately measure such properties in the extreme and complex environment of nuclear test reactors.

A key parameter during irradiation tests is temperature. Temperature monitoring is currently achieved with both passive- and active-monitoring techniques.[12] Active-monitoring techniques, such as thermocouples, provide real-time data and are typically expensive because they require the implementation of instrumentation leads. On the other hand, passive-monitoring techniques are typically used in static irradiation capsules, and can provide an insight toward peak temperatures.[13] For those instances where irradiation tests are seeking a less-expensive measurement method and/or the experiment requires instrumentation without leads such as static capsule experiments, passive techniques are the preferred method for temperature monitoring.[10]

Melt wires are a passive monitoring technique that enables identification of the peak temperature achieved during an irradiation test.[14] This method involves placing wires of a known composition and well-characterized melting temperature within an experimental test capsule designed for materials testing. The peak test temperature is then inferred during post-test examination or post-irradiation examination (PIE) where the melt wires are inspected for visual signs of melting. If the material shows signs of

melting it can then be reasoned that the peak temperature during testing exceeded the melting point of melt wire material. On the other hand, it is determined that the peak test temperature remained below the melting point of the wire material if the wire does not show signs of melting. Preferably, materials chosen for melt wires have a low neutron-absorption cross-section while exhibiting distinct and reproducible melting behavior when they have been exposed to temperatures beyond their respective melting point.

Current state-of-the art passive peak temperature sensors used within MTRs are melt wires, and within this work will be referred to as classical melt wires. These melt wires have been matured through a meticulous material selection process and the development of validation procedures to confirm their temperature dependent properties. The process for classical melt-wire fabrication includes the ability to encapsulate multiple wire materials into one small-diameter unit which contains the samples under inert atmosphere.[15] The library of qualified materials for melt-wire selection contains more than 40 useful materials with a detection range between 29.73 °C and 1535 °C.[15] Wire materials are chosen based on expected irradiation test temperatures and required temperature measurement resolution.[14] While classical melt wires are commonly used in test-reactor experiments, such as those conducted in the ATR, some test designs have limited space due to predesigned capsules that may only be a couple of millimeters in diameter. As multiple specimens are contained within the capsules at once, this can leave little or no space for passive and/or active instrumentation.

The production of miniature, robust peak temperature sensors is made possible through additive manufacturing (AM) techniques such as aerosol-jet printing (AJP), ink-jet printing (IJP), and micro-dispense printing (MDP). The incorporation of these AM

techniques in the design of in-pile instrumentation enables the development of advanced sensors for MTRs with features as small as 10 μm, which is advantageous for device miniaturization, especially when considering that traditional melt-wire capsules typically require a wire length of approximately 2 mm.[16,17] Currently, novel technologies such as AJP are being explored for the development of unique sensors that are otherwise unobtainable with conventional fabrication processes.[13,18–21]

The ability to directly deposit functional materials onto a wide range of substrates using AM techniques makes it possible to expand the encapsulation design and methods used for melt wire fabrication. AM facilitates the miniaturization of the entire melt wire package to accommodate more irradiation experiments. While the actual melt wires may be further miniaturized with currently available microfabrication techniques, the need to miniaturize the entire melt wire package is severely limited with the use of classical fabrication methods and materials. This is because classical melt wires are sealed within a quartz capsule to suspend and separate melt wires under inert atmosphere. The use of quartz as the encapsulation material is the limiting factor in further miniaturizing the melt wire package, as glass-blowing techniques can only allow for a certain degree of miniaturization before the integrity of the melt wire package is compromised. A solution to this is to transition the encapsulation material away from quartz to metals, which can be easily machined and welded.

Classical machining techniques, such as milling, can produce small components such as a very small container with a corresponding lid to contain printed melt wires sealed under inert atmosphere via laser welding or other metal joining techniques. Using AM techniques wires could be easily printed on the base of the container, and through

thoughtful design of the container and lid this would provide a way seal to the melt wires within an inert atmosphere, which is critical for melt wire performance. Fabricating a melt wire packages in this way is only afforded by utilizing AM methods.

Previous work has successfully demonstrated the ability to fabricate low-cost and compact melt wire chips by printing silver melt wires within a 2 mm 316 L chip with a first iteration of an encapsulation design for AM melt wires.[22] To expand on that work, the study reported here aims to demonstrate and benchmark the performance and reliability of AM melt-wire materials when compared to their classical counterparts. This work demonstrates the feasibility of AM techniques for the fabrication of advanced nuclear in-pile passive temperature sensors. The performance of prototypical classical melt wires serves as a benchmark to compare the performance of AM melt wire capsules containing aluminum (Al), zinc (Zn), and tin (Sn) AJP deposited melt wires. To minimize the number of variables introduced during benchmark testing, the encapsulation method for both the traditional and AM melt wires was based on classical fabrication techniques that do not allow for overall device miniaturization. Second, significant design improvements to the encapsulation design for AM melt wires from the first iteration were introduced with a second iteration to allow for an inert atmosphere within the capsule, which is critical for melt wire performance, especially when melt wire oxidation is of concern. The melting point of each of these materials encompasses the operating temperatures of a wide range of different reactor systems.[23,24] For these studies, the low melting-point material used was Sn, with a melting point of approximately 230 °C, Zn melts at approximately 420 °C, and the high melting-point material was Al, with an approximate melting point of 660 °C.

## 3.3 Materials and Methods

3.3.1. Materials

The incorporation of advanced fabrication methods of sensors for melt wires requires the development of ink materials containing melt-wire materials of interest while demonstrating compatibility with additive-printing technologies. For this study, AJP-compatible inks were synthesized that contained the melt wire materials of interest. Melt wire ink feedstock materials were purchased as nanopowders. Aluminum nanopowder (99.9%, 800 nm, 1–2% PVP-coated), zinc nanopowder (99.9%, 95–105 nm, 1–2% PVP-coated) and Sn nanopowder (99.9%, 60–80 nm, 1–2% PVP-coated) were all acquired commercially from US Research Nanomaterials (Houston, TX, USA). Nanopowder dispersion was achieved with the use of USP grade 200-proof ethanol (Fisher Scientific, Waltham, MA, USA), high purity ethylene glycol (VWR Life Science, Radnor, PA, USA), and BYK-156 (BYK USA Inc., Wallingford, CT, USA). All chemicals and reagents were used as received, without further purification or modification.

3.3.2. Methods

3.3.2.1. Ink Synthesis

First, a stock solution was created to act as the dispersion medium for nanopowders; it was composed of 0.1 g of BYK-156 added to a 1:3 solution of ethanol to ethylene glycol, which was allowed to stir for 1 hour. Three different AJP inks were created from each individual nanopowder. For the optimization process, inks, having a nanopowder loading of 60 wt%, were initially produced using a high shear mixer (5000 RPM for 15 min; L5M-A equipped with a 5/8 in. microtubular mixing unit, Silverson). To benchmark the performance of the initial ink composition, AJP was used and,

depending on the consistency of the output, additional solvent was added. If necessary, the dispersion medium was added in 5 mL increments and then subjected to high-shear mixing. This process continued until the desired output and ink performance were achieved. Final concentrations for each of the inks were as follows: 45 wt%, 60 wt%, and 40 wt% for tin, aluminum, and zinc, respectively.

### 3.3.2.2. Powder Feedstock Particle Size and Composition Analysis

Powders were characterized with transmission electron microscopy (TEM) for particle size analysis, X-ray diffraction (XRD) analysis for identifying powder composition and differential scanning calorimetry (DSC) to identify the melting point of the powder feedstock. Particle size analysis was performed with images obtained with a FEI Tecnai F3-FEG STwin TEM with EDS using a single tilt holder and a Formvar/Carbon 200 mesh copper grid (Ted Pella, Inc., Redding, CA, USA). ImageJ software was used to evaluate the average particle size for each powder feedstock. Confirmation of the feedstock powder composition was accomplished with XRD analysis using a Rigaku Smart Lab operating with a parallel beam geometry in combination with PDXL software.

### 3.3.2.3. Differential Scanning Calorimetry (DSC)

Stock materials and AJP inks used to fabricate the standard and AM melt wires, respectively, were subjected to DSC (Netzsch DSC 404 C Pegasus) to evaluate the melting temperature of each material to validate the melting point of the actual stock material used, rather than relying on standard data. Alumina crucibles were used for determining the melting phase transitions of experimental samples. A four-step temperature program consisting of: (1) a ramp of 5 °C/min until a targeted temperature of

50 °C below the expected melting point of the material was reached; (2) a reduction of the ramp rate to 1 °C/min until a target temperature of 50 °C above the expected melting point was reached; (3) cooling the sample to the targeted temperature of 50 °C below the expected melting point of the material and holding for one-hour dwell to ensure that the DSC had truly come down to the targeted temperature; (4) repeating this process three more times This temperature profile was repeated for a total of four times, and the onset temperature was used as expected melting point for the printed melt wires. This analysis was completed using the last three runs with Proteus® software (Netzsch).

### 3.3.2.4. Additively Manufactured (AM) Melt Wire Fabrication

Fabrication of the AM melt wires was achieved with the pneumatic atomizer (PA) of an Optomec Aerosol Jet 200, equipped with a 200 μm nozzle. The bubbler solvent add-back system, employing a 1:1 ratio of ethylene glycol to ethanol, was used to minimize the effects of solvent loss during atomization. During printing, the ink was held at 35 °C to optimize ink atomization. The tool platen temperature (65 °C), pneumatic atomizer (600 CCM), virtual impactor (500 CCM), and sheath gas (50 CCM) flow rates were optimized to ensure that the line widths and material deposition of functional materials were adequate to obtain the desired device dimensions. $SiO_2$ on Si was utilized as the substrate for the printed melt wires. Prior to printing, the substrates were triple rinsed (acetone, methanol and nanopure water) within an ultrasonic bath to clean the substrate surface. After each subsequent cleaning, nitrogen gas was used to dry the substrate.

The printed melt wires were sintered within a tube furnace (MTI GSL-11X-NT) at a temperature of 200 °C for 1 h in a reducing atmosphere (2% $H_2$ with nitrogen balance,

50 mL/min) to minimize oxidation while sintering and to remove any residual solvent. The aerosol jet printed melt wires of tin, zinc and aluminum, shown in **Figure 3.1a.**, were fabricated to have a geometry of 0.25 mm (W) × 20 mm (L) in order to compare their performance to that of a standard melt wire. The wires were sealed within a quartz tube with a helium atmosphere. The capsule was verified as a sealed instrument prior to furnace testing. For the second part of this study, improvements to the AM melt wire encapsulation design from the first iteration were made. First attempts at miniaturizing melt wire packaging included a 2 mm diameter and 0.5 mm thick Stainless Steel 316 (SS316) disc. It was milled to create a dimple or a pocket and melt wire materials that were printed within the dimple. Next, a blank SS316 disc was placed on the printed melt wire chip, and laser micro-welded to seal and encapsulate the printed materials within SS316.[22,25]

This work improves on the encapsulation design by addressing two critical features, material thickness and the environment within the capsule as shown in **Figure 3.2.** First, the thickness of the encapsulation material was significantly reduced to a side wall thickness of 0.6 mm and a floor thickness of 0.2 mm. Starting with a 5 mm SS316 rod (McMaster-Carr), an initial cut was made using a 3.57 mm end mill to a depth of 0.76 mm followed by a second cut to create a shoulder for the lid to sit recessed within the encapsulation. The second cut, which overlaid the first cut, made with a 4.35 mm end mill to a depth of 0.25 mm. Then, a cap (4.4 mm × 0.254 mm) was milled to fit within the second cut. Dimensions and a schematic of this design can be found in **Figure 3.2**.
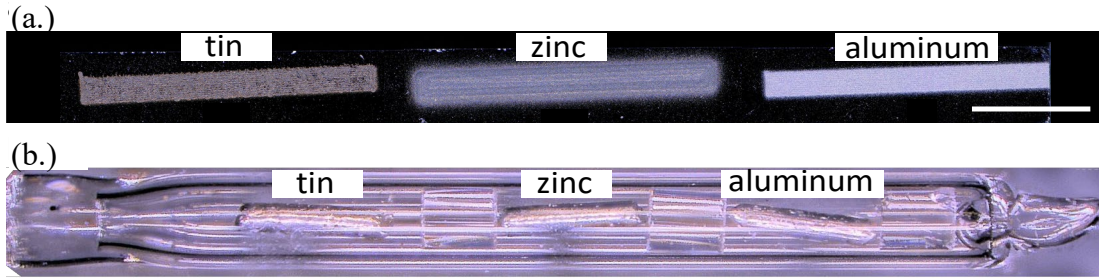
**Figure 3.1.    Additively manufactured (AM) and classical melt wire capsules.**
**Prototypes of (a) AM melt wires of aluminum, zinc and tin fabricated by aerosol jet**
**printing on an SiO₂/Si substrate, and (b) a classical melt wire capsule containing**
**aluminum, zinc and tin. For testing, both AM and classical melt wires were**
**contained within quartz capsules with a helium atmosphere at ambient pressure.**
**Scale bars represent 1 mm.**



| Variable | Dimensions (mm) |
|---|---|
| a | 0.25 |
| b | 0.76 |
| c | 0.32 |
| d | 0.39 |
| e | 5.00 |
| f | 4.37 |
| g | 3.57 |
| h | 4.34 |
| i | 0.25 |
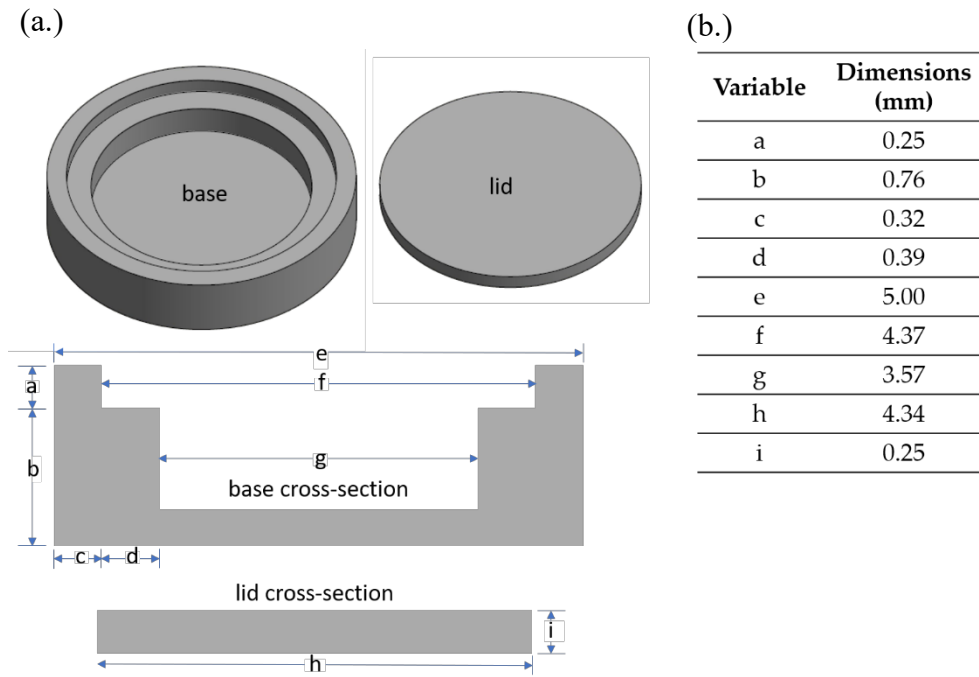
**Figure 3.2.    New AM melt wire encapsulation. (a) A schematic of the new**
**encapsulation design with base and lid cross-section shown, and (b) dimensions of**
**the base and lid.**

For this sealing process, changes included the design of a top lid to be attached using a precision laser welder. To aid in the laser welding process, a shoulder was built into the wall of the base to allow the lid to sit recessed in the container such that the lid and base provided a flush surface to weld on (**Figure 3.3a**). Laser welding was

accomplished with a LaserStar Fiberstar Workstation 7600, and seal welds were

completed using 180 W with specific settings at 2.6 J, a pulse width of 16 ms, and a beam

diameter step of 5.
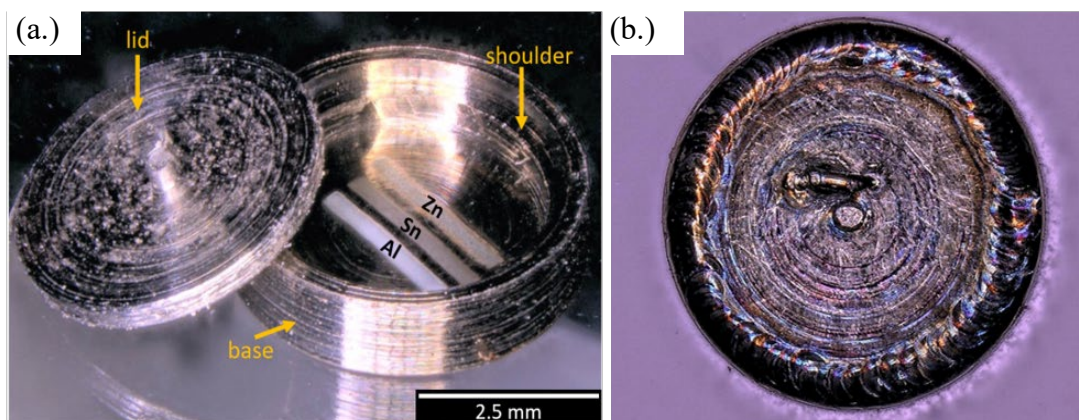


**Figure 3.3.** **Inert atmosphere encapsulation design for AM melt wires. (a) Melt wire container ready to be sealed with AM melt wires on the base of the encapsulation package, and (b) a top-view of the sealed capsule.**

On the center of the lid, a small extrusion was added as a feature to assist with

handling. To create an inert atmosphere within the encapsulation, a small weep hole was

created in the lid (approximately 250 µm) prior to attaching the lid to the base, and a

weld was created around the entire lid in air. While laser welding the lid, applying too

much energy during the sealing process initially melted the printed melt wires with lower

melting points. To prevent premature melting, it was necessary to use a copper cradle fit

to press against the melt wire container base to serve as a heat sink during the laser

welding process. To ensure the melting point of the melt wires was not exceeded during

welding, temperature was monitored on the prototypes with a thermoelement (type K)

directly attached to the substrate where the printed melt wires were located. Laser welds

were then performed using the energy necessary to close the lid. After a few

modifications to ensure a tight fit from the copper to the container, temperatures could be

limited to a maximum of 135 °C, ensuring no premature melting of the melt wire materials.

Next, an inert atmosphere was introduced into the sealed container by suspending it within a vacuum system to purge all air and was backfilled with high-purity helium. The final seal was completed by shooting the laser through a quartz window while the melt wire container was in view within the vacuum system. To ensure that an inert atmosphere was maintained within the container, the sealed piece (**Figure 3.3b**) was subjected to a helium leak check to confirm that a true seal exists.

3.3.2.5. Classical Melt Wire Fabrication

Classical melt-wire fabrication involves a series of activities that can be completed repeatedly to ensure reliable and consistent results. For this study, wires of aluminum (99.999% metals basis, with 0.5 mm dia., Puratronic), zinc (99.994% metals basis, with 0.5 mm dia., Puratronic) and tin (99.9% metals basis, with 0.5 mm dia., Leico Industries, Inc., Lyndhurst, NJ, USA) were used to fabricate wires 2 mm in length (Figure 1b.). Particular attention was given to cleaning each piece to minimize the possibility of impurities within the final product. The wires were then sealed within a quartz tube with quartz spacers placed between separate materials under vacuum in a helium atmosphere. Quartz spacers were placed between them to separate the materials during the experiment. The capsule was verified as a sealed instrument and furnace tests were conducted to examine performance, observe material interactions between melt wires or the quartz containment tube, and to provide the insight required to visually discern melting after heating in the quartz encapsulated tubes.

3.3.2.6. Furnace Testing

For both melt-wire types and for both studies the tube furnace (Lindberg clam shell tube furnace max 1200 °C) was brought up to the target temperature, and the melt wires were inserted so that they were positioned vertically during testing. To evaluate performance, each melt capsule was tested at a temperature slightly below and above the materials melting point, as determined by DSC. Tin was evaluated at 215 and 245 °C, zinc at 405 and 435 °C, and aluminum at 640 and 675 °C.

3.3.2.7. X-ray Computed Tomography

A General Electric (GE) Phoenix v|tome|x nXCT system was used to collect X-ray radiographs and perform micro-computed tomography (XCT). The X-ray generator used was a GE 180 kV nano-focus X-ray tube (Model # XS180NF) with a 5-micron spot size. A GE Dynamic 41–100, flat-panel X-ray detector was used. The detector has a 100 µm pixel pitch and an active area of 410 mm × 410 mm. CT was possible through a precision rotation stage located between the source and detector.

The settings for the X-ray generator were 75 kV and 225 µA, with an aluminum filter that was 0.5 mm thick. The magnification was 24.99× which resulted in a 4.000176 µm Voxel size. A total of 2200 projections were collected resulting in a 0.18° rotation per projection. Eight exposures were averaged for each projection with a 500.031 ms timing. GE's proprietary reconstruction software, Phoenix Datos, was used for tomographic reconstruction.

Evaluation of melt wires is accomplished by obtaining initial XCT images of a sealed melt wire assembly before the experiment to serve as a reference point. Then, after the experiment a new XCT image is obtained and compared against the reference image

to determine if any changes had occurred. Part of the fabrication process is to test prototypes of each material using the same imaging techniques used for PIE to identify any characteristics that indicate melting has occurred.

### 3.3. Results

3.3.1. Powder Feedstock Characterization

Once melt wire materials are selected, they are ordered from reliable vendors that provide a certification of purity that remains traceable throughout the fabrication process. For AM melt wires, characterization of the powder feedstock is critical for assessing compatibility with the selected additive technology and identifying material composition. The average particle size was evaluated with TEM imaging (**Figure 3.4a,d,g**) for tin, zinc and aluminum powder feedstocks was determined to be $92 \pm 50$ nm, $230 \pm 100$ nm and $76 \pm 27$ nm, respectively. Powder composition was confirmed with XRD (**Figure 3.4b,e,h**), and it was anticipated that the melting point for each powder feedstock would be in good agreement with standard values. Although the powder feedstock is purchased from a reliable vendor and composition is confirmed with XRD, when the physical material is received,  it is verified by empirically evaluating its melting point using DSC (**Figure 3.4c,f,i**) to detect heat absorption of the sample as it undergoes the endothermic phase transition from solid to liquid. The expected melting point derived from DSC analysis for each melt wire fabricated with AJP inks of tin, zinc or aluminum nanopowders are $228.3 \pm 0.7$ °C, $415 \pm 1$ °C, and $656.5 \pm 0.3$ °C, respectively.
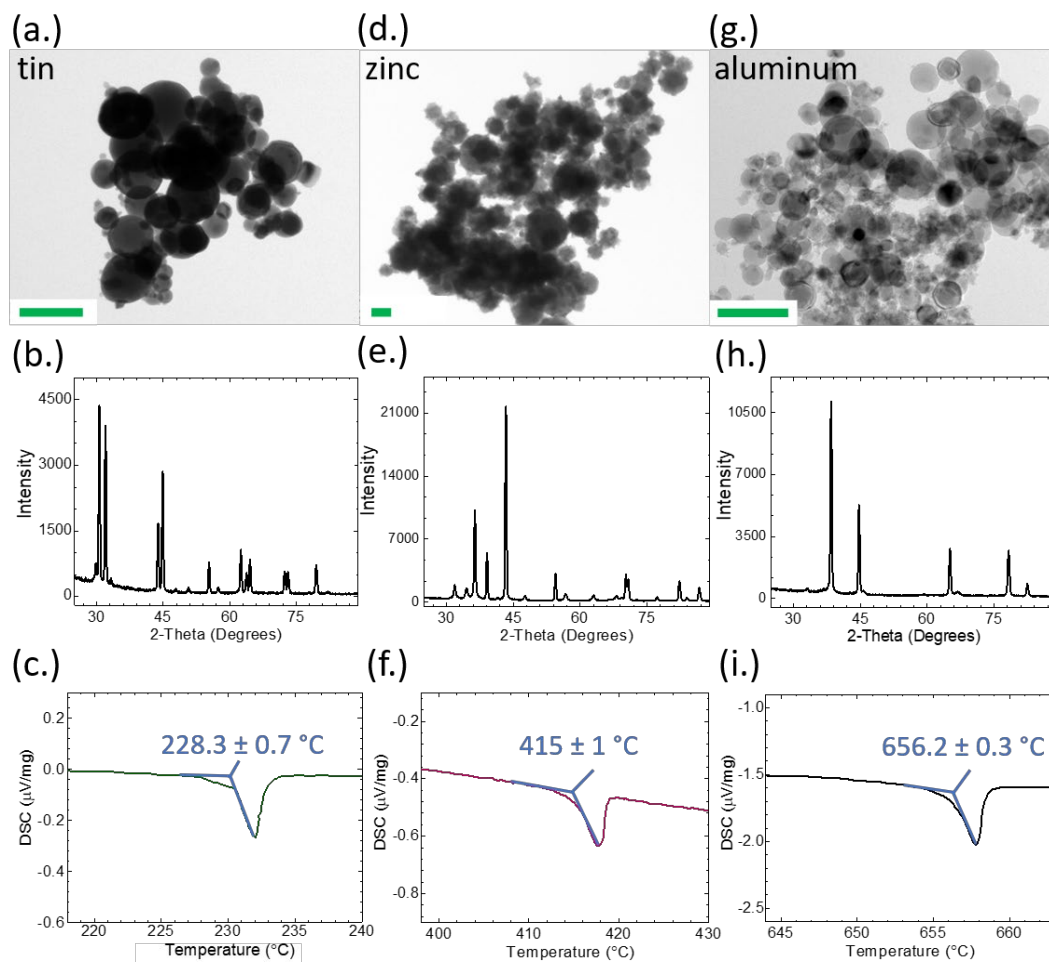
**Figure 3.4.** **Characterization of melt wire feedstock. Melt wire feedstock powders of (a-c) tin, (d-f) zinc and (g-i) aluminum were characterized for particle size with transmission electron microscopy (TEM) (a,d,g), composition with X-ray diffraction (XRD) (b,e,h), and melting point with differential scanning calorimetry (DSC) (c,f,i). Scale bars are 200 nm.**

3.3.2. AM and Standard Melt Wire Performance Evaluation

Classical and AM melt wires, encapsulated within quartz tubing (**Figure 3.1a,b**), were then subjected to furnace testing within a helium atmosphere to examine the performance, observe material interactions, and explore any interactions with the quartz encapsulation tube or $SiO_2$/Si substrate of the melt wires. Additionally, this evaluation method provides an understanding for any morphology changes that would indicate that melting has occurred.

For both melt-wire types, the furnace was brought up to the target temperature, and the melt wires were inserted so that they were positioned vertically during testing. To evaluate performance, each melt capsule was tested at a temperature slightly below and above the materials melting point, as determined by DSC. With that, tin was evaluated at 215 and 235 °C, zinc at 405 and 435 °C, and aluminum at 640 and 675 °C. Micrographs of the wires at room temperature (RT) and after melting are provided for both the standard and AM melt-wire capsules in **Figures 3.5 and 3.6**, respectively. For the standard melt wire capsule, the aluminum wire (**Figure 3.5a**) had clearly melted prior to the expected melting point of 660 °C and testing at 675 °C was not performed.

During furnace testing of the AM melt wires, however, the melting behavior for each of the three different materials appeared to be consistent: bubbles or beads were observed to form after the metals were exposed to temperatures that were near or beyond their expected melting point (**Figure 3.6**). Interestingly, both the standard and AM aluminum melt wires displayed visual melting characteristics after having been exposed to a testing temperature of 640 °C, which is about 20 °C below the expected melting point determined through DSC.

Using the new encapsulation design, AM melt wire performance tests were completed with assemblies containing air and helium gas to evaluate the impact of the environment. Initial considerations towards melt wire containment did not entrap an inert atmosphere to ensure good melt wire performance because of the use of silver in initial evaluations, and oxidation was not of a significant concern.[23] However, most materials used to fabricate melt wires are prone to oxidation, and to support the use of these materials in an inert atmosphere is critical.

Using SS316 as the encapsulation material eliminated the ability to use the traditional visual observation methods for evaluating the melt behavior of AM melt wires. To overcome this, XCT was used to produce detailed images of the melt wires before and after furnace tests. To demonstrate the need for an inert atmosphere, a melt wire assembly was assessed having an air encapsulation. A reference XCT image was collected before the melt wires were exposed to a temperature above their expected melting point. Those samples with an air encapsulation did not show distinguishable signs of melting even after exceeding expected melting temperatures more than 50 °C. However, the aluminum melt wire did exhibit some unexpected behavior when exposed to temperatures beyond its expected melting temperature as the line detached from the SS316 substrate and started bending upward. This uncharacteristic phenomenon can be observed in **Figure 3.7**, but this was only after reaching a temperature well in excess (greater than 50 °C) of its expected melting point of 660 °C.

An AM melt wire assembly having an inert encapsulation was then evaluated using the same method. A reference XCT image was collected before the melt wires were exposed to a temperature above all their expected melting points (680 °C). XCT images were then taken to evaluate the changes that should have occurred from melting. Contrast levels were adjusted for each melted material to provide the greatest detail for each image.

a.)



b.)
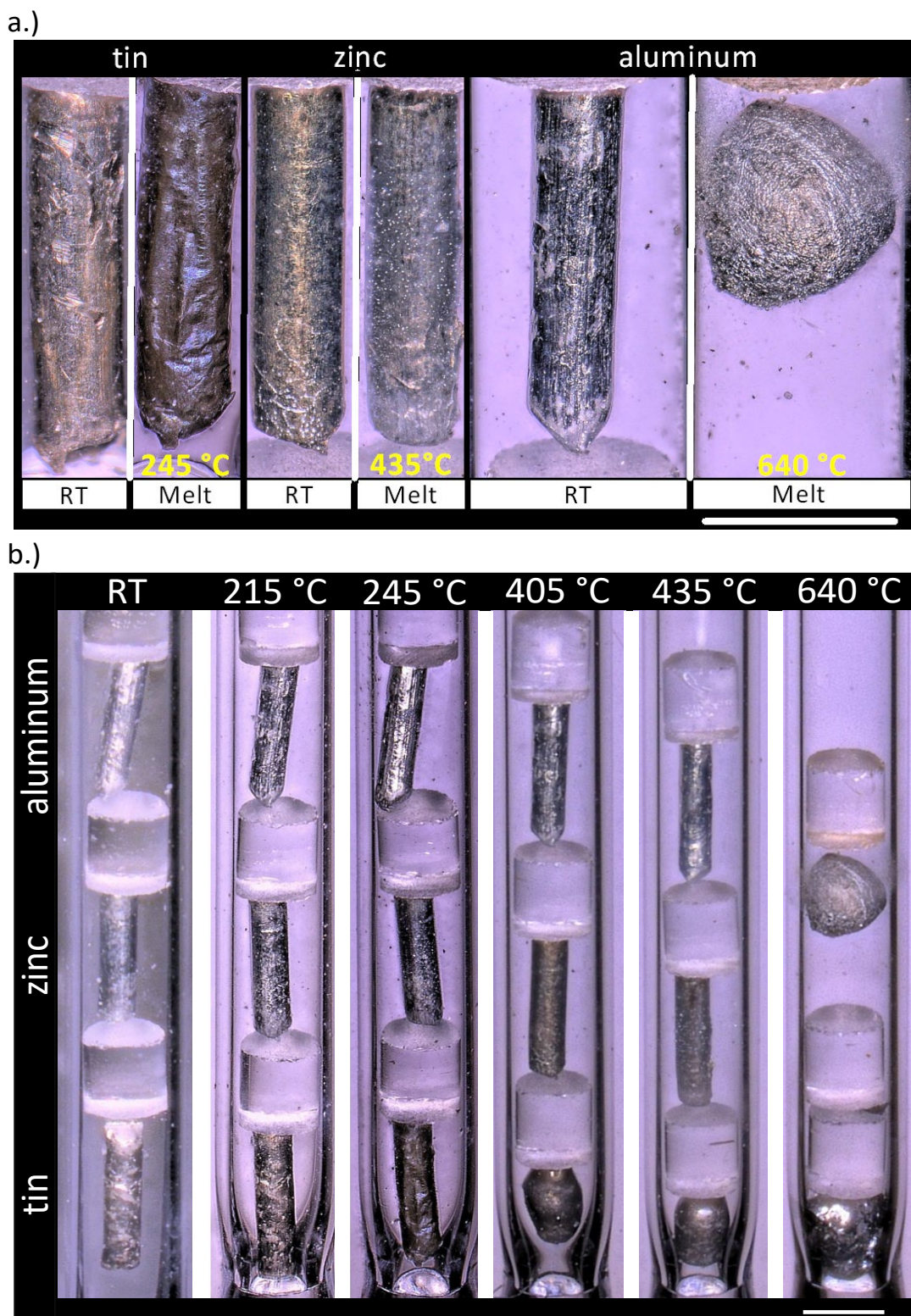


**Figure 3.5.** **Standard melt wire capsule furnace testing: magnified view of the visual temperature response indicating melting of (a) individual melt wires of Sn, Zn and Al, and (b) of the full capsule. Scale bars represent 1 mm.**
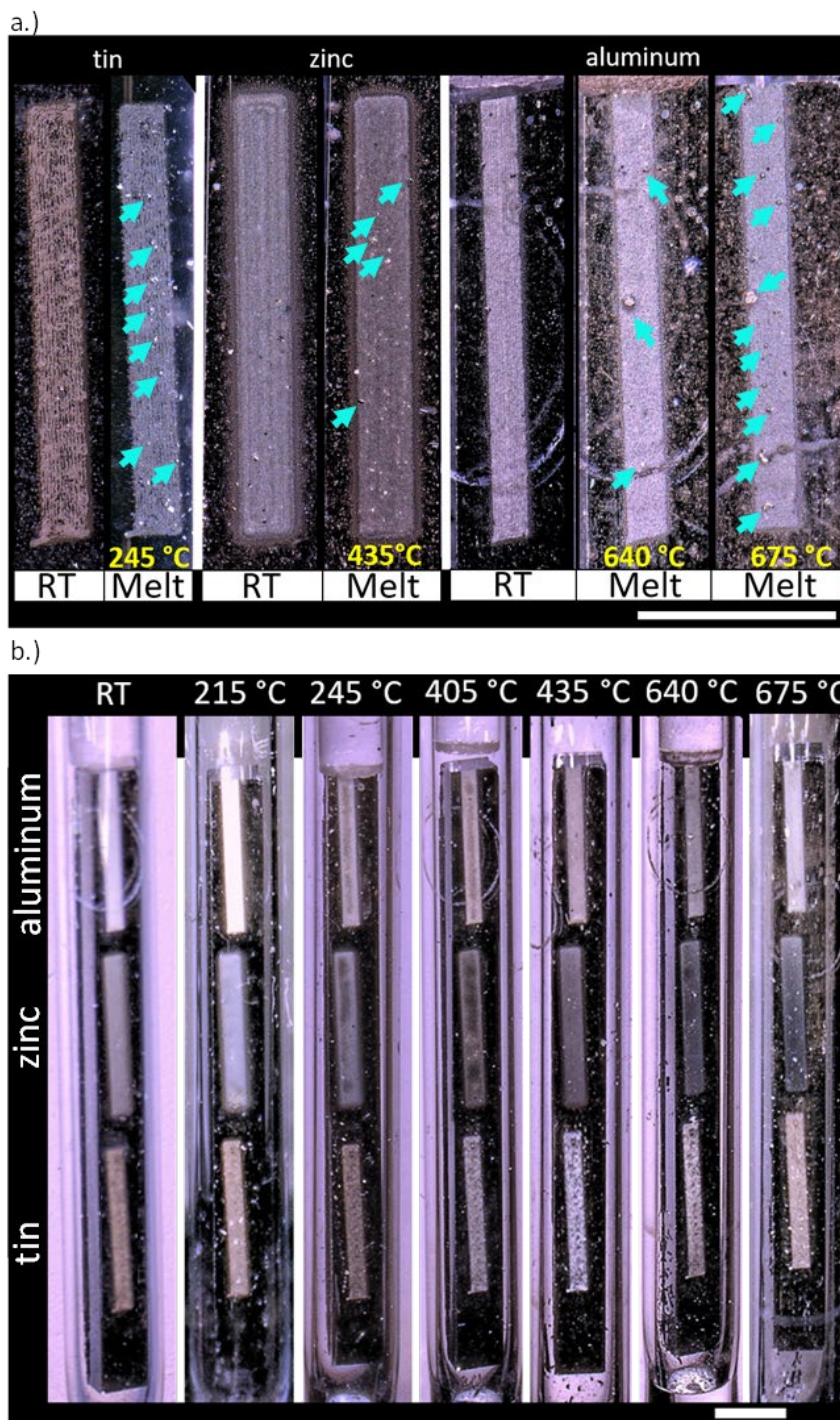
**Figure 3.6.** Micrographs of AM melt-wires in quartz capsule for furnace testing. (a) A magnified view of the temperature response indicating melting of individual melt wires of Sn, Zn, and Al, where the blue arrows indicate beading of the melt wire material due to melting. (b) Full view of quartz capsule with AM melt wires. Scale bars represent 1 mm.
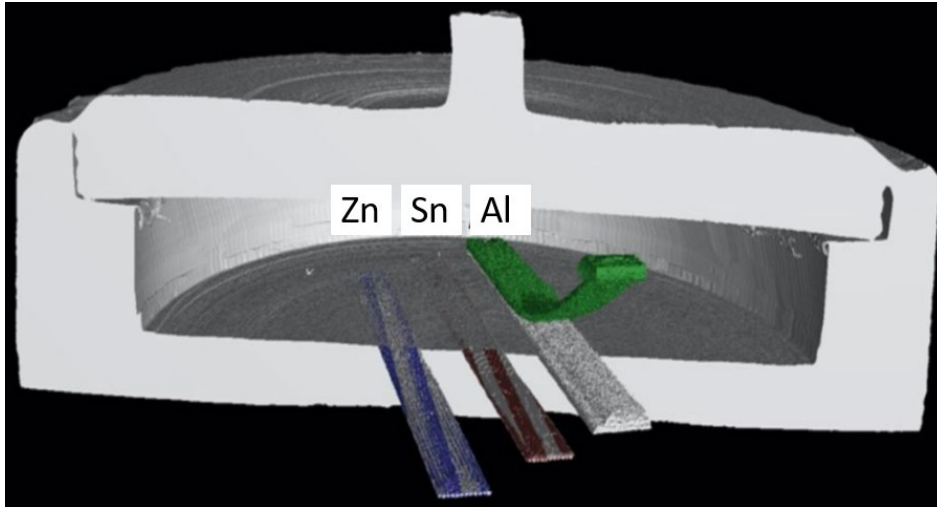
**Figure 3.7.**   **Cross section of a post furnace X-ray micro-computed tomography (XCT) image with zinc (blue), tin (maroon), superimposed over pre-furnaced image of a container sealed in air. Melt wires without color were taken before the furnace test. Melt wires with color were taken after exceeding the melting point of all three materials indicating no visible changes on two out of three wires when encapsulated in air.**

The lowest melting point material was tin which had the most obvious changes compared to the other printed materials. From Figure 8 the tin collected in a pool near the center of the container. Zinc exhibited some subtle changes that could be identified to imply melting had occurred, which can be seen in **Figure 3.9**.
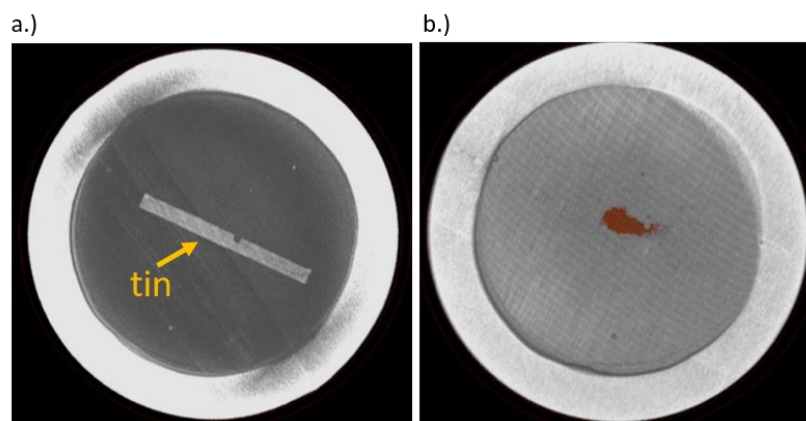


**Figure 3.8.**   **XCT images of AM tin melt wire. (a) Original XCT image of tin encapsulated in helium, and (b) post-furnace image of melted tin enhanced with color.**
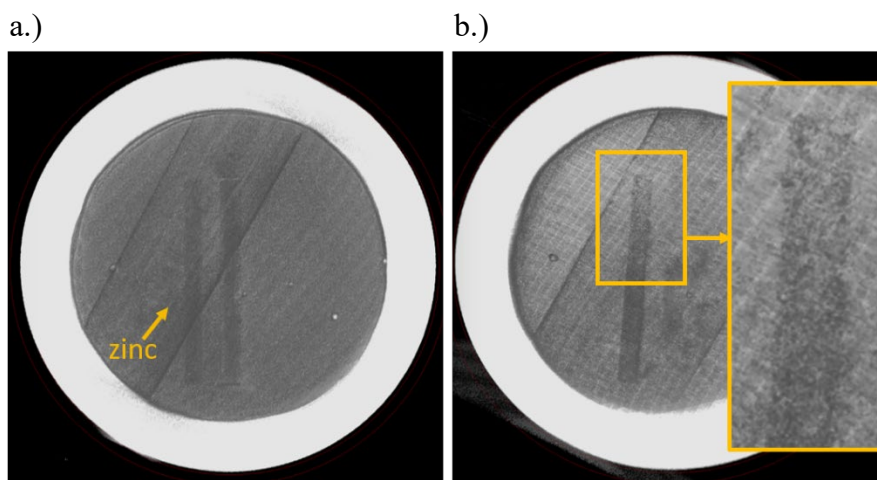
**Figure 3.9.     XCT images of AM zinc melt wire. (a) Original XCT image of zinc encapsulated in helium, (b) post-furnace image of zinc with enhanced image highlighting material separation.**

When compared to the original XCT image it was observed that a section along the zinc wire showed separation. Finally, for the evaluation of aluminum (**Figure 3.10**), the printed line on the original XCT image was unclear, and in the post-furnace image the aluminum wire was even harder to identify. From these tests it was inconclusive as to whether aluminum had melted or was just unidentifiable against the encapsulation material.
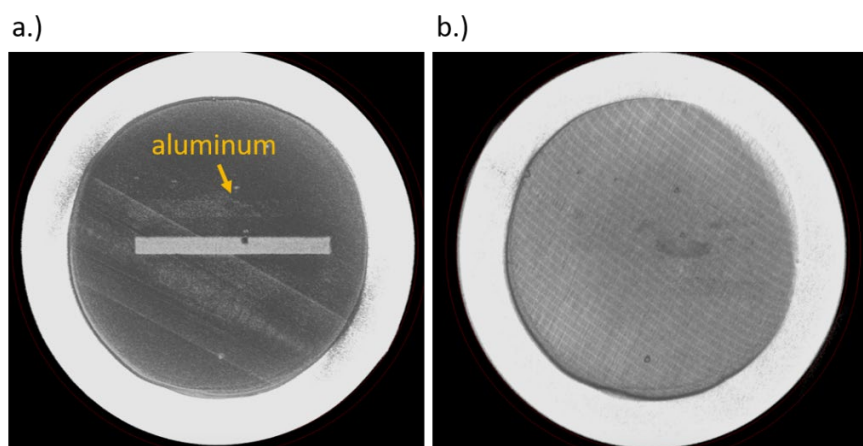


**Figure 3.10.   XCT images of AM aluminum melt wire. (a) Original XCT image of aluminum encapsulated in helium, (b) post-furnace image of melt wire capsule with the aluminum wire not discernable against the SS316 substrate.**

## 3.4. Discussion

<u>3.4.1. Powder Feedstock Characterization</u>

The expected melting point derived from DSC analysis for each melt wire
fabricated with AJP inks of tin, zinc or aluminum nanopowders are expected to be 228.3
± 0.7 °C, 415 ± 1 °C, and 656.5 ± 0.3 °C, respectively. The melting points derived from
DSC evaluation vary slightly from that of the standard values of 231.9 °C, 419.5 °C, and
660.3 °C for tin, zinc and aluminum, respectively (Table 3.1.). These deviations are
attributed to impurities within the feedstock materials, which results in the broadening of
the melting point. For melt wire performance, consistent melt behavior of a material is far
more important than obtaining a melting point that is close to the theoretical values.
Understanding this, DSC measurements for each material are performed in triplicate to
ensure that the melt behavior of the material is consistent.

**Table 3.1.      DSC melting point results.**

| Material | Theoretical melting point | Melting point derived from DSC Powder Feedstock | Meling point derived from DSC bulk wire |
|---|---|---|---|
| Tin | 231.9˚C | 228.3±0.7˚C | 231.8˚C |
| Zinc | 419.5˚C | 415±1˚C | 419.3 ˚C |
| Aluminum | 660.3˚C | 656.5±0.3˚C | 660.5˚C |

<u>3.4.2. AM and Standard Melt Wire Performance Evaluation</u>

Normally, melt-wire materials within a capsule are chosen to provide information
for a target location within a MTR that is not expected to exceed a certain temperature.
For example, having a projected temperature of an experiment, material selection would
begin with identifying a material having a melting point around 30 to 50 °C below the

expected peak temperature. The next material selection would require the identification of a material having a melting point identical to or within 5 to 10 °C of the anticipated maximum temperature of the experiment, and the last material would include one having a melting point that exceeds projected experiment temperature by approximately 50 °C. Under normal experimental circumstances, this last material would not be expected to melt; however, this can provide information about unforeseen events during an experiment that may otherwise not be caught. Unlike a typical peak-temperature test, this material performance test was done to provide comparison information over a large range of melting temperatures to examine whether the melt-wire performance varied between standard and AM melt wires with materials having a wide range of melting temperatures. Melting evaluation for a material after an experiment can be challenging because not all melted materials have the same visual characteristics, as shown above. **Figure 3.5a** highlights the challenge of identifying optically whether melt wires have exceeded their melting temperature. It is very common to see that a melt wire has flowed to the bottom of the capsule when the capsules are in a vertical orientation, which is observed with zinc at temperatures well beyond its melting point (**Figure 3.5b**). On the other hand, some materials only exhibit softening and require identifying rounded edges where sharp features had existed in the non-melted wire, as seen with tin (**Figure 3.5b**). Other materials will draw together to form a sphere, or bubbles or beads sometimes form along abrupt edges or cracks while the bulk of the material appears unaffected due to surface tension, as seen with the aluminum melt wire (**Figure 3.5b**). Due to significant variations in visual melting characteristics, it is important to accurately identify what has occurred during prototype testing to recognize melting after an experiment.

A phenomenon that is not as common, but is known to exist, includes materials reacting with one another during elevated temperatures causing vapor alloying or migration that results in material deposition onto another material or directly to the quartz tubing. This often results in a melting-point depression, as is observed with both forms of the aluminum wire. It is anticipated that this sort of interaction is the cause of the deviation from the expected melting point identified with DSC because this test is performed in an isolated and inert atmosphere. Furthermore, previous tests on the same stock material have resulted in an expected melting point (660.5 °C), and the melting characteristics from those tests are shown in **Figure 3.11**, with a comparison between the melt behavior of an aluminum classical (**Figure 3.11a,b**) and AM melt wire (**Figure 3.11c,d**) are highlighted
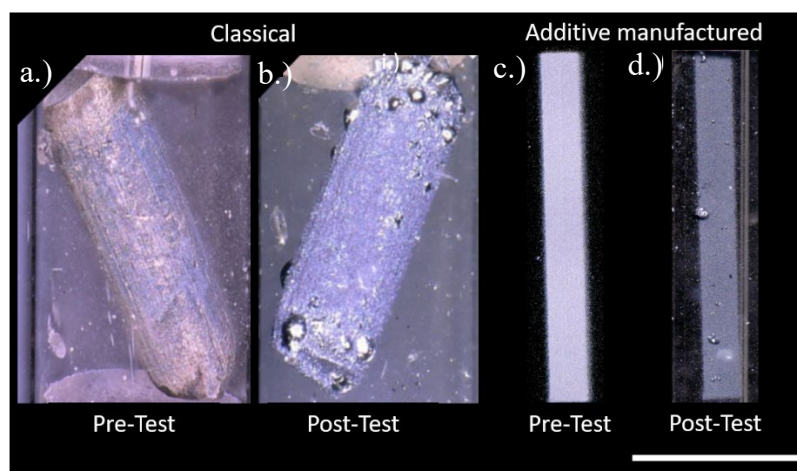


**Figure 3.11. Comparison of melt behavior of classical and AM aluminum melt wires. Micrographs of the expected melt behavior of stock aluminum wire at room temperature (a) before DSC testing and (b) after DSC testing, for which the melting point was determined to be 660.5°C. Micrographs of the observed melt behavior of AM melt wires (c) before and (d) after furnace testing. Scale bar represents 1 mm.**

Through the progression of micrographs in **Figures 3.5 and 3.6**, material deposition is observed on the quartz tube, and this is more clearly visualized with the

melt of zinc in **Figure 3.5a**, and material vaporization is further supported through

**Figure 3.6b.** The zinc wire appears to fade while material buildup on the quartz tube

demonstrates a direct relationship with test temperature. Through these observations, it is

concluded that, during the testing process, a vapor alloying-like process has occurred,

which is responsible for the melting point depression of the standard and AM aluminum

melt wires.

The ability to further miniaturize the melt wire package was introduced with the

use of AM methods as it provides a way to deposit melt wire materials directly onto a

substrate, and this allowed for an exploration into different encapsulation designs that

would not otherwise be possible. The use of different melt wire materials for peak

temperature monitoring also introduces the consideration that different materials have

different melting characteristics, and it is important to identify features before using them

within an irradiation experiment. These changes can include but are not limited to

rounded edges where sharp features had previously existed, the formation of a sphere of

the entire melted line, or the development of bubbles or beads while the bulk of the

material appears unaffected. Characterization of AM melt wires requires an assessment of

each material's melt behavior by identifying changes between XCT images before and

after exposure to melting temperatures. For this work, the evaluation method used for

classical melt wires could not be used due to the opaque encapsulation material.

Therefore, XCT was chosen because it is a capability that is available for PIE and it

enables imaging of the melt wire materials through opaque encapsulation.

With the use of the new encapsulation design, it was observed that melt

identification could be made for tin and zinc after having exposed the melt wire capsule

(with inert environment), but not for aluminum due to the low contrast between the aluminum melt wire and the SS316 substrate. Furthermore, the melt behavior of the same materials on a $SiO_2/Si$ substrate and a stainless steel substrate showed inconsistencies, which highlight the need to characterize the melt behavior of AM melt wires with each substrate they are deposited on. With these results, future work will require the exploration of additional encapsulation materials and/or melt wire materials focused towards selecting encapsulation and melt materials that have high contrast for the XCT imaging process.

AM methods provide a novel approach towards device miniaturization. While the melt wires themselves may be miniaturized, future work must focus on methods to miniaturize the entire melt wire package to include the melt wire encapsulation. To elaborate, the use of quartz as the transparent encapsulation material limits the ability to miniaturize a melt wire package, and materials that support these efforts are generally opaque and would require the development of welding and sealing methods that would provide both protection and a controlled environment to the printed melt wires. Furthermore, the use of different encapsulation methods and materials would, in turn, require higher-resolution microscopy or the incorporation of methods, such as XCT, if opaque encapsulation materials are used.

Melting evaluation for a material after an experiment can be challenging because not all melted materials have the same visual characteristics, as seen in Figures 5 and 6. Additionally, this work demonstrates that for AM melt wires, the choice of substrate will play a role in melt behavior, as different melting characteristics were observed between the $SiO_2/Si$ substrate and SS316. It is very common to see that a melt wire has flowed to

the bottom of the capsule if the capsules are in a vertical orientation, which is observed with zinc at temperatures well beyond its melting point (**Figure 3.5b**). Finally, the use of higher-resolution microscopy methods will be required to better visualize melt-wire features and melting characteristics of AM melt wires. This introduces the need to consider potential issues with X-ray contrast in material selection between substrate and melt wire material. Ultimately, the incorporation of AM melt wires would supply a complimentary peak test-temperature determination, and a better melt-evaluation technique for AM melt wires.

### 3.5. Conclusions

AM methods, such as AJP, possess significant potential for the fabrication of advanced sensors and instrumentation. This is especially true for instances where miniaturization of sensors is required due to space limitations within an experiment. To demonstrate the feasibility of incorporating AM techniques for the fabrication of advanced nuclear in-pile passive temperature sensors, a comparison between standard and AM melt wires of tin, aluminum and zinc was completed. Through DSC and furnace testing, it was determined that the performance of the AM melt-wire capsule was consistent with that of the standard melt-wire capsule.

## 3.6 References

1.    Chu, S., Cui, Y. & Liu, N. The 3ath towards sustainable energy. *Nat. Mater.* **16,** 16–22 (2016).

2.    Solomon, B. D. & Krishna, K. The coming sustainable energy transition: History, strategies, and outlook. *Energy Policy* **39,** 7422–7431 (2011).

3.    Brook, B. W., Alonso, A., Meneley, D. A., Misak, J., Blees, T. & van Erp, J. B. Why nuclear energy is sustainable and has to be part of the energy mix. *Sustain. Mater. Technol.* **1,** 8–16 (2014).

4.    Locatelli, G., Mancini, M. & Todeschini, N. Generation IV nuclear reactors: Current status and future prospects. *Energy Policy* **61,** 1503–1520 (2013).

5.    Zinkle, S. J. & Was, G. S. Materials challenges in nuclear energy. *Acta Mater.* **61,** 735–758 (2013).

6.    Was, G. S., Petti, D., Ukai, S. & Zinkle, S. Materials for future nuclear energy systems. *J. Nucl. Mater.* **527,** 151837 (2019).

7.    Bong Goo, K., Rempe, J. L., Villard, J. F. & Solstad, S. Review of instrumentation for irradiation testing of nuclear fuels and materials. *Nucl. Technol.* **176,** 155–187 (2011).

8.    Calderoni, P., Hurley, D., Daw, J., Fleming, A. & McCary, K. Innovative sensing technologies for nuclear instrumentation. *I2MTC 2019 - 2019 IEEE Int. Instrum. Meas. Technol. Conf. Proc.* **2019-May,** (2019).

9.    Pope, C. L., Jensen, C. B., Gerstner, D. M. & Parry, J. R. Transient Reactor Test (TREAT) Facility Design and Experiment Capability. *Nucl. Technol.* **205,** 1378–1386 (2019).

10.   Marshall, F. M. Advanced Test Reactor Capabilities and Future Operating Plans. *Variety* **INL/CON-05,** 1–8 (2005).

11.   Marshall, F. M., Allen, T. R., Benson, J. B. & Thelen, M. C. Advanced test reactor national scientific user facility partnerships. *Trans. Am. Nucl. Soc.* **105,** 121–122 (2011).

12. Rempe, J. L., Knudson, D. L., Daw, J. E., Condie, K. G. & Curtis Wilkins, S. New sensors for in-pile temperature measurement at the advanced test reactor national scientific user facility. *Nucl. Technol.* **175,** 681–691 (2011).

13. Fujimoto, K. T., Watkins, J. K., Phero, T., Litteken, D., Tsai, K., Bingham, T., Ranganatha, K. L., Johnson, B. C., Deng, Z., Jaques, B. & Estrada, D. Aerosol jet printed capacitive strain gauge for soft structural materials. *npj Flex. Electron.* **4,** (2020).

14. Daw, J. E., Rempe, J. L., Knudson, D. L., Unruh, T. C., Chase, B. M., Davis, K. L. & Palmer, A. J. Temperature monitoring options available at the Idaho national laboratory advanced test reactor. *AIP Conf. Proc.* **1552 8,** 970–975 (2013).

15. Davis, K. L., Knudson, D. L., Daw, J. E., Rempe, J. L. & Palmer, A. J. Melt wire sensors available to determine peak temperatures in ATR irradiation testing. *8th Int. Top. Meet. Nucl. Plant Instrumentation, Control. Human-Machine Interface Technol. 2012, NPIC HMIT 2012 Enabling Futur. Nucl. Energy* **1,** 427–434 (2012).

16. Mahajan, A., Frisbie, C. D. & Francis, L. F. Optimization of aerosol jet printing for high-resolution, high-aspect ratio silver lines. *ACS Appl. Mater. Interfaces* **5,** 4856–4864 (2013).

17. Seifert, T., Sowade, E., Roscher, F., Wiemer, M., Gessner, T. & Baumann, R. R. Additive manufacturing technologies compared: Morphology of deposits of silver ink using inkjet and aerosol jet printing. *Ind. Eng. Chem. Res.* **54,** 769–779 (2015).

18. Pandhi, T., Cornwell, C., Fujimoto, K., Barnes, P., Cox, J., Xiong, H., Davis, P. H., Subbaraman, H., Koehne, J. E. & Estrada, D. Fully inkjet-printed multilayered graphene-based flexible electrodes for repeatable electrochemical response. *RSC Adv.* **10,** 38205–38219 (2020).

19. Paulsen, J. A., Renn, M., Christenson, K. & Plourde, R. Printing conformal electronics on 3D structures with aerosol jet technology. *FIIW 2012 - 2012 Futur. Instrum. Int. Work. Proc.* 47–50 (2012). doi:10.1109/FIIW.2012.6378343

20. Rahman, M. T., Rahimi, A., Gupta, S. & Panat, R. Microscale additive

manufacturing and modeling of interdigitated capacitive touch sensors. *Sensors Actuators, A Phys.* **248,** 94–103 (2016).

21. Rahman, T., Renaud, L., Heo, D., Renn, M. & Panat, R. Aerosol based direct-write micro-additive fabrication method for sub-mm 3D metal-dielectric structures. *J. Micromechanics Microengineering* **25,** (2015).

22. Mondal, K., Fujimoto, K. & McMurtrey, M. D. Advanced Manufacturing of Printed Melt Wire Chips for Cheap, Compact Passive In-Pile Temperature Sensors. *Jom* **72,** 4196–4201 (2020).

23. Allen, T., Busby, J., Meyer, M. & Petti, D. Materials challenges for nuclear systems. *Mater. Today* **13,** 14–23 (2010).

24. Yvon, P. & Carré, F. Structural materials challenges for advanced reactor systems. *J. Nucl. Mater.* **385,** 217–222 (2009).

25. Mondal, K., Fujimoto, K. & McMurtrey, M. Non-visual analysis of miniaturized melt wire arrays for in-pile measurement of peak irradiation temperature. (2020). at <https://www.osti.gov/servlets/purl/1668675/>

CHAPTER FOUR: ADDITIVE MANUFACTURING OF NEUTRON DOSIMETERS

FOR DIRECTIONAL FLUX MEASUREMENTS

**4.1 Abstract**

To maintain the highest nuclear operation safety standards, an understanding

towards the design limits and material response of nuclear fuels and associated structural

elements during reactor operations is critical. Reactor dosimetry can determine the

energy-dependent neutron flux during reactor operations by irradiating materials of

different compositions and measuring radioisotopic products with gamma-ray

spectrometry. Monitoring neutron flux is typically performed with passive sensors known

as neutron dosimeters, and classical neutron dosimeters, due to geometry constraints,

cannot accommodate directional flux monitoring, which results in an incomplete picture

of the irradiation environment during an experiment. Using Digital Light Projection and

Micro-Dispense printing novel flux foils or Advanced Manufactured Dosimeters (AMDs)

were fabricated to enable directional flux monitoring within nuclear reactors, and four

different materials (iron, cobalt, titanium and nickel) were selected for testing to target a

range of neutron energies. The foils were arranged so they were facing in either

north/south or east/west directions and were accompanied by classical neutron flux wires

as a way to benchmark the response of the AMDs. Two different assemblies of AMDs

and classical wires were subjected to two separate transient trials within TREAT and the

number of fissions for each dosimeter material was determined via gamma-ray

spectroscopy. The results from gamma spectrometry results revealed asymmetry in the neutron flux under some test conditions.

## 4.2 Introduction

The TRansient REActor Test facility (TREAT) housed at the Idaho National Laboratory (INL) is a unique research reactor, as it is an air-cooled, thermal spectrum, pulsed and graphite moderated reactor capable of safely generating very large integrated bursts of thermal neutrons over a large sample volume.[1] With a core made up of highly enriched uranium disperse in graphite with a 10,000:1 carbon-to-uranium atom ratio that provides a highly negative temperature coefficient of reactivity for safe self-limiting power excursions.[2,3] Furthermore, the TREAT reactor consists of a square 19 × 19 lattice of positions for assemblies (mostly fuel assemblies, but also including control rod assemblies) on a 4-inch pitch creating a 6-ft 4-in–square maximum core size with 361 available assembly positions. Experiment vehicles are accommodated in the reactor by removing fuel assemblies and replacing them with an experiment vehicle, typically in the center of the reactor.[2] TREAT was designed to provide a facility for irradiation experiments capable of depositing a large amount of energy into an experimental sample over a short period of time. With these power pulses, it is possible to induce intense fission heating in the nuclear fuel that is being tested to evaluate failure mechanisms and nuclear reactor fuel performance under severe reactor accident conditions.[4]

According to the United States Nuclear Regulatory Commission, a transient event is one where a change in the reactor coolant system temperature, pressure, or both, is attributed to a change in the reactors power output. Furthermore, transients can be caused by adding or removing neutron poisons, by increasing or decreasing electrical load on the

turbine generator, or with accident conditions. Following the events at the Fukushima

Daiichi Nuclear Power Plant the United States Department of energy developed the

Accident Tolerant Fuels program to improve reactor sustainability, safety and

performance by developing fuels with greater accident tolerance for the current and

future generation of nuclear reactors while reducing the potential of proliferation of

nuclear materials.[5,6] To maintain the highest nuclear operation safety standards, it is

critical that an understanding towards the design limits and material response of nuclear

fuels and associated structural elements during transient events be established, and one

use identified for TREAT is to test various types of sensors and instrumentation to

elucidate the reactor environment during irradiation experiments. Experiments at this

facility are used to guide the development and improvement of advanced nuclear fuel

designs, and to validate computer models of fuel and core behavior as required for U.S.

Regulatory Commission evaluation of nuclear reactor power design and safety

evaluations.

To support these efforts, computational modeling campaigns are currently

underway to establish methods that provide 3-D modeling capabilities and the ability to

predict the amount of energy deposited in an irradiation experiment during a power

excursion, along with its axial distribution. As these factors are dependent on a large

number of variables including (but not limited to): core configuration, the experiment

vehicle design, instrumentation and containment, the nature of the fuels sample or

samples themselves, coolant/moderator, control rod positions and motion history, and

temperature changes during the transient.[7] With the lack of 3-D modeling capabilities

prior to being placed in standby mode, it was impossible to predict energy deposition in a

test sample before an experiment. To validate 3-D simulations, experiments targeted towards physics measurements to provide 3-D temperature, 3-D flux, fission wire and spectral measurements must be performed, and current efforts within advanced/additive manufactured (AM) in-pile sensors have significant potential to support these activities.

Having a unique configuration among typical research reactors, TREAT possesses an asymmetrical flux in the core, where in a typical water-cooled research reactor with a cylindrical core design, omitting any filters or significant structures, the thermal and fast neutron flux is radially symmetric. The asymmetry of flux has been simulated previously, but the creation of advanced manufactured dosimeters (AMDs) allows for the measurement of this phenomena inside the core during a transient.[7] Classical neutron dosimeter wires, due to geometry constraints, do not allow for directional flux monitoring within a nuclear reactor and results in an incomplete picture of the irradiation environment for an experiment. As the focus of TREAT is materials characterization during transient events, it is critical to develop sensors and instrumentation capable of providing quantitative and orientation specific neutron flux data so a more holistic view of the irradiation environment can be elucidated during these tests. Access to high quality quantitative data for the validation of modeling and simulation efforts requires the qualification of sensors and instrumentation to evaluate both their performance within an irradiation environment, and their integration within the TREAT reactor. So, current efforts are under way to qualify sensors and instrumentation for experiment deployments. With that, the primary purpose of isolated sensor testing in the TREAT facility is to evaluate the impacts of the irradiation environment to in-pile sensors and to demonstrate sensor integration within the TREAT facility. A secondary purpose is to support ongoing

physics testing and characterizing reactor performance that serves as a supplement to both objectives is the use and development of passive dosimeters (also known as flux/fission wires), which is the focus of this work.

Current dosimetry methods typically consist of the irradiation of low-impurity metals in the forms of foils or wires, and then subsequent measurement of the foils or wires with gamma or mass spectrometry. The metals are typically purchased with a certificate of impurity levels. Impurities in dosimetry materials can produce unintended interferences during gamma spectrometry and increase detector dead time and personnel dose. Additive manufacturing methods provide a unique opportunity to produce dosimetry materials with material and dimensional flexibility that may not be attainable with a traditional method. Additionally, additively manufactured dosimeters (AMDs) can be used to discern directional flux information in the reactor, which is especially important in the Transient Reactor Test (TREAT) facility.

Additive manufacturing is a rapid prototyping process that builds components layer-by-layer from computer aided design software, or three-dimensional object scanners (3D) enabling a strong linkage between digital and physical manufacturing.[8] These advanced methods stand to enlarge the design envelope by relaxing design constraints to allow for manufacturing of unique functional geometries, and additional versatility is introduced with the wide selection of materials made available with AM technologies through feedstock development activities. For sensor fabrication, the ability to deposit functional materials on virtually any surface supports innovative sensor and instrumentation development, which could stand to revolution the way in-pile sensors and instrumentation are fabricated while also supporting the development of advanced

sensors and instrumentation having better performance than their classically fabricated counterparts.

The range of AM technologies can be classified into several categories: binder jetting, material jetting, direct energy deposition, sheet laminations, material extrusion, powder bed fusion, and vat photo-polymerization.[9] In this work, the printing modalities that are highlighted include vat photo-polymerization with the use of a Dynamic Light Projector (DLP) to print the alumina encapsulation, and material extrusion accomplished with Micro-Dispense Printing (MDP) to print the flux foils.

Vat polymerization includes several different processes including stereolithography, DLP, continuous liquid interface production, and daylight polymer printing, and introduces the ability to produce ceramic components having sub 100 micro-meter complex features.[10,11] With this technique, selective curing is made possible with the implementation of photocurable polymers within the printer feedstock, and the desired pattern is projected using an ultraviolet source into the feedstock converting it into a layer of solid material.[12] This process is repeated until the part is completed.

Material extrusion methods can include direct printing processes, such as micro-dispense printing (MDP), which are high-throughput and maskless methods that the enables the printing of various complex structures with fine feature sizes, and is capable of printing standard thick film, screen-printable materials, which makes it compatible with a wide range of materials.[13,14] Briefly, this process uses a paste containing the functional material of interest, and it is extruded through a nozzle attached to the printer cartridge. Both the DLP and MDP processes use CAD software to create a 3D representation of the printed piece, which is then translated to the printer. Finally, both

methods require post-processing to remove any remaining solvent, binders, etc to achieve a sintered component.

For this work, two different additive manufacturing processes were explored to fabricate novel flux foils or AMDs to enable directional flux monitoring within a nuclear reactors, and four different parent materials (iron, cobalt, titanium and nickel) were selected for testing to target a range of neutron energies. Several AMDs were produced with various metals chosen for their traditional use in reactor dosimeter: titanium (Ti), iron (Fe), cobalt (Co) and nickel (Ni). The AMDs were arranged so that foils were either oriented in the North/South or East/West directions and were accompanied by classical flux wires to benchmark the response of the AMDs. Two different assemblies consisting of 9 AMDs for a total of 18 AMDs were subjected to two separate transient trials within TREAT and the number of fissions for each dosimeter material was evaluated with gamma-ray spectroscopy, which quantifies the number of atoms of specific fission products from characteristic gamma-ray peaks in the measured spectrum.[15] From these experiments, we demonstrate, for the first time, the ability to perform directional flux monitoring within a nuclear reactor core with the introduction of AM fabrication methods.

### 4.3 Materials and Methods

4.3.1 Materials

4.3.1.1 Advanced Manufactured Dosimeters

Alumina slurry (Admaprint A130), 1,2-Ethanediol (Sigma Aldrich; Anhydrous 99.8% purity), ethanol (Sigma-Aldrich; 200 proof anhydrous and $\geq 99.5\%$ purity,) Cobalt Oxide nanopowder (U.S. Research Nanomaterials; 1-2 wt% PVP coated with

99.9% purity and 15 nm average particle size), iron nanopower (U.S. Research Nanomaterials; 1-2 wt% PVP coated with 99.5+% and 35-45 nm average particle size), nickel nanopowder (U.S. Research Nanomaterials, 1-2 wt% PVP coated with 99.9% and 40 nm average particle size), and titanium nanopowder (U.S. Research Nanomaterials, 1-2 wt% PVP coated with 99.9+% purity and 30-50 nm average particle size). All materials and solvents were used as received with no further modification or purification.

### 4.3.1.2 Classical Flux Wires

Flux wires of iron (Good Fellow Corporation; Product No. FE005180), aluminum (99.0%)/cobalt (0.01%) (Good Fellow Corporation; Product No. AD205160) and titanium (Good Fellow Corporation; Product Number TI005135) were selected to have a 1 mm diameter and were cut to 5 mm lengths. All materials were used as received with no further modification or purification.

### 4.3.1.3 Dosimeter Assembly

A titanium tube (SHAANXI Lasting Titanium Industry Co., LTD.; ASTM B338-12, ASME SB338-13; Grade 2) was used as the dosimeter assembly housing, and a titanium spacer wire (Goodfellow; Product number TI007915; Grade 1; >99.6% purity; 3.0 mm OD) was included to stabilize the internal components of the dosimeter stack. An aluminum tube (Goodfellow; Product Number AL007200; 99.5% purity; 3.00 mm OD and 0.69 mm wall) was used to hold the classical neutron flux wire assembly. The dosimeter stack was arranged using a stainless steel 304 square wire (McMaster-Carr; Product number 4253K19. All materials were used as received with further modification or purification.

4.3.2 Methods

4.3.2.1 Advanced Manufactured Dosimeter Encapsulation

The ceramic encapsulation was designed in SOLIDWORKS, and the printed foils were created using Digital Light Projection on an Admatech A130 with alumina slurry (Admaprint A130). A 15 mm long two-part capsule was fabricated having a maximum diameter of 4.57 mm (**Figure 4.1a**). A recessed area (1 mm (L) x 0.5 mm (To allow for specific directional orientation, a square hole was included in the design of the piece, to accommodate a 1.02 x 1.02 mm square wire that would be used during the assembly process. Each component was labeled during the printing process to identify the material and the intended monitoring direction.
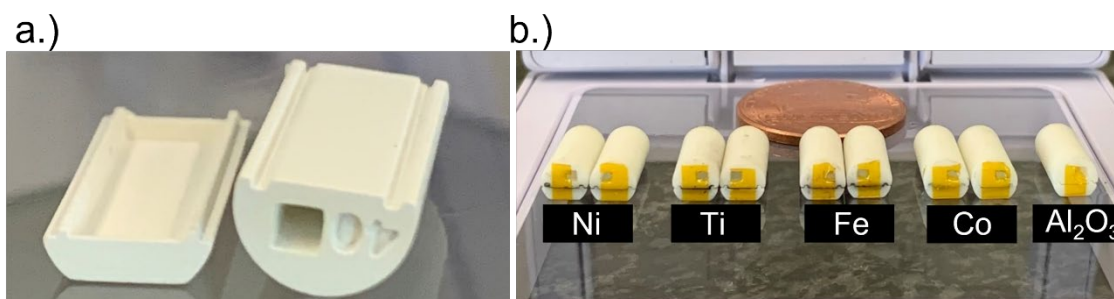


**Figure 4.1.** **Advanced manufactured dosimeters. a.) Two part capsule fabricated via DLP with alumina with a square hole to orient the AMD flux foils in either N/S or E/W directions, and b.) a representative AMD array used for MNFW-1 and MNFW-2 irradiation experiments.**

The green AMD forms were then subjected to the debinding and sintering to remove the organic binders and to remove the starting porosity to establish the defining microstructure and material properties. This process begins by submerging the prints in water (24 hours at 30 °C), to remove as much of the water-soluble components in present in the resin as possible. After soaking the forms were wiped with a soft brush to wipe off any non-cured resin on the surface of the print. Next, the forms were dried, in air, for 24

hours. During the debinding step organic components (binders) are removed with high temperature, and for the alumina the following debinding heating profile was used: (1) Starting at room temperature, ramp the furnace to 150 °C at a rate of 60 °C/hour, (2) dwell at 150 °C for 30 min, (3) ramp the furnace to 450 °C at a rate of 12 °C/hour, (4) ramp the furnace to 1000 °C at a rate of 60 °C/hour, (5) dwell at 1000 °C for 120 min, (6) bring the furnace back down to room temperature at a rate of 100 °C/hour.

After the debinding step is completed, the pieces are sintered to allow the alumina particles within the print to come in close contact with one another to increase the density of the print, which results in shrinking of the overall dimension. The sintering step was completed with the following heating profile: (1) Starting at room temperature ramp the furnace to 1000 °C at a rate of 200 °C/hour, (2) dwell at 100 °C for 30 min, (3) ramp the furnace to 1575° C at 100 °C/hour, (4) perform a second ramp to 1625 at 75 °C/hour, (5) dwell at 1625 °C for 120 min, (6) bring the furnace down to room temperature at a rate of 300 °C/hour.

### 4.3.2.2 Advanced manufactured dosimeter foils

As material mass is critical for gamma spectroscopy, the encapsulation material was weighed before printing (top and bottom), and the entire AMD was weighed post-sintering to obtain the mass of the dosimeter material. The same weigh scale (Mettler Toledo, XPR Analytical Balance), and average mass was obtained by weighing each material before and after sintering in triplicate.

KiCAD, was used to design the dosimeter foils for a Voltera V-One Prototyping Circuit Board Machine (Geonoise Malaysia Sdn. Bhd.). The V-One printer was equipped with a 200 µm nozzle, and print parameters such as filling pattern, print speed, dispense

height, feedrate, trim length, trace penetration, anti-stringing distance, kick, soft start ratio, soft stop ratio and rheological setpoint were optimized for each print to deposit the appropriate amount of dosimeter material to fill the recessed area within the alumina encapsulation. The pastes used in this study were synthesized in house using the following procedure: A 80 wt% paste was created by combining the appropriate amount of nanopowder (titanium, cobalt oxide, iron or nickel) to 50 mL of ethylene glycol within a glovebox to minimize oxidation. Next, the mixtures were transferred to a planetary mixer (Thinky AR-100), and a homogenous slurry was created using an RPM of 2000 for 10 min.

After deposition, the top of the alumina dosimeter encapsulation was placed on top to finish the AMD capsule. Next, the AMD capsules were inserted into a 100 °C furnace with an argon environment and were allowed to dry overnight. After the drying step, the furnace was brought up to 500 °C using a slow ramp (1 C/min) to 500 °C followed by a dwell at 500 °C for 1 hour. The furnace was then brought down to room temperature, the AMDs were removed, and then weighed. A total of 9 dosimeters (**Figure 4.1b**) were contained in each experiment (2-titanimum, 2-iron, 2-nickel, 2-cobalt, and 1 blank)

### 4.3.2.3 Classical Neutron Flux Wire Assembly

Each wire (titanium, iron and Al(99.9%)/Co(0.1%)) were cut to 5.00 mm in length and were purchased at a diameter of 1 mm was weighed to obtain the mass prior to irradiation and loading into assembly tube. After the wires were inserted into the aluminum tube, the tube was crimped on both ends to ensure that the wires would stay within the tube during assembly and testing (**Figure 4.2**).
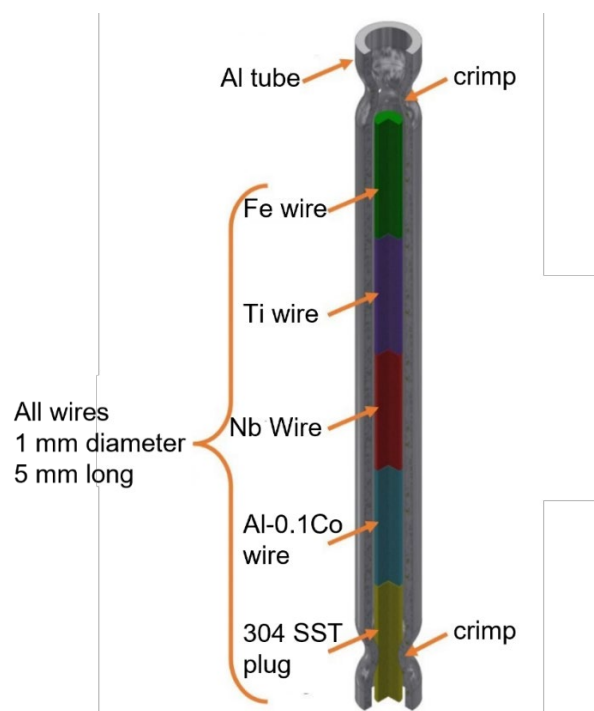
**Figure 4.2.    Classical dosimetry assembly**

One historically important method for obtaining relevant reactor data for nuclear experiments is the use of fission and flux wires. Fission and flux wires have been employed in recent years at TREAT.[5] The method for irradiating flux wires in TREAT has been to utilize a vertical titanium tube with an outer diameter of 0.25 inches which is plugged at the bottom (see Figure 1). Titanium was selected for the TREAT concurrent testing holder material due to its high heat resistance (unlike aluminum) and relatively low activation in the presence of neutron flux (unlike stainless steel), contributing to low doses for personnel working with irradiated materials. Other metals such as aluminum and stainless steel are also used in portions of flux wire assemblies where it makes sense to do so. indicated by a flat face of the alumina encapsulation. The dimensions of all components within the assembly are summarized in Table 4.1.

**Table 4.1.** **Dimensions of assembly components**

| Item | Length (mm) |
|---|---|
| Titanium spacer wire (bottom) | 443 |
| MNFW-1-C1 | 30 |
| MNFW-1-AMD1 | 10 |
| MNFW-1-AMD2 | 10 |
| Bare square wire | 10 |
| MNFW-1-AMD3 | 10 |
| MNFW-1-AMD4 | 10 |
| MNFW-1-AMD5 | 10 |
| Bare square wire | 10 |
| MNFW-1-C3 | 30 |
| MNFW-1-AMD6 | 10 |
| MNFW-1-AMD7 | 10 |
| Bare square wire | 10 |
| MNFW-1-C4 | 30 |
| MNFW-1-AMD8 | 10 |
| MNFW-1-AMD9 | 10 |
| Bare square wire | 10 |
| Empty aluminum tube (Top) | 1498 |

4.2.3.4 Irradiation Test Holder

Prior to irradiation, the AMDs were installed in the center irradiation position (K-10) very near the physical center of the reactor core in the east-west and north-south directions (**Figure 4.3a**). Both the MNFW-1 and MNFW-2 assemblies were installed in the center experiment position of the TREAT reactor, and the AMD assembly titanium tubes were placed in the "A" position (**Figure 4.3b**.).

a.)
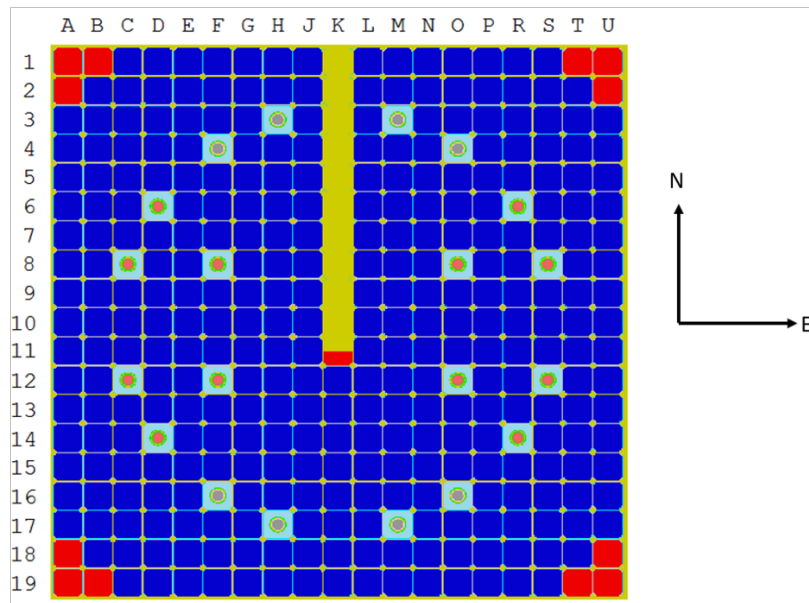
b.)
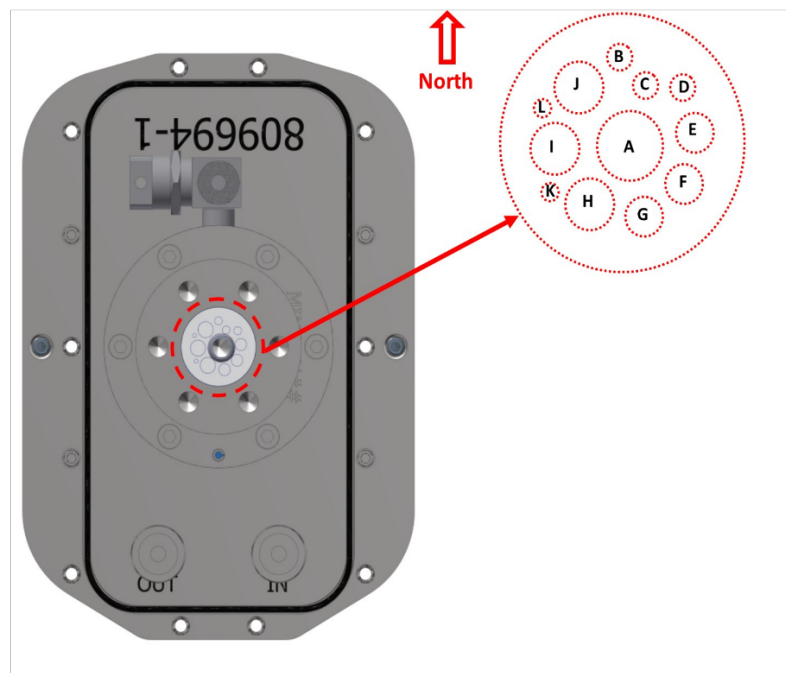


**Figure 4.3.    AMD irradiation experiment. a.) TREAT core schematic showing the K-10 position and b.) a top-down view of the MIMIC-N instrument cluster installed in the Buster experiment vehicle where the classical flux wires and AMDs were inserted in the A position.**
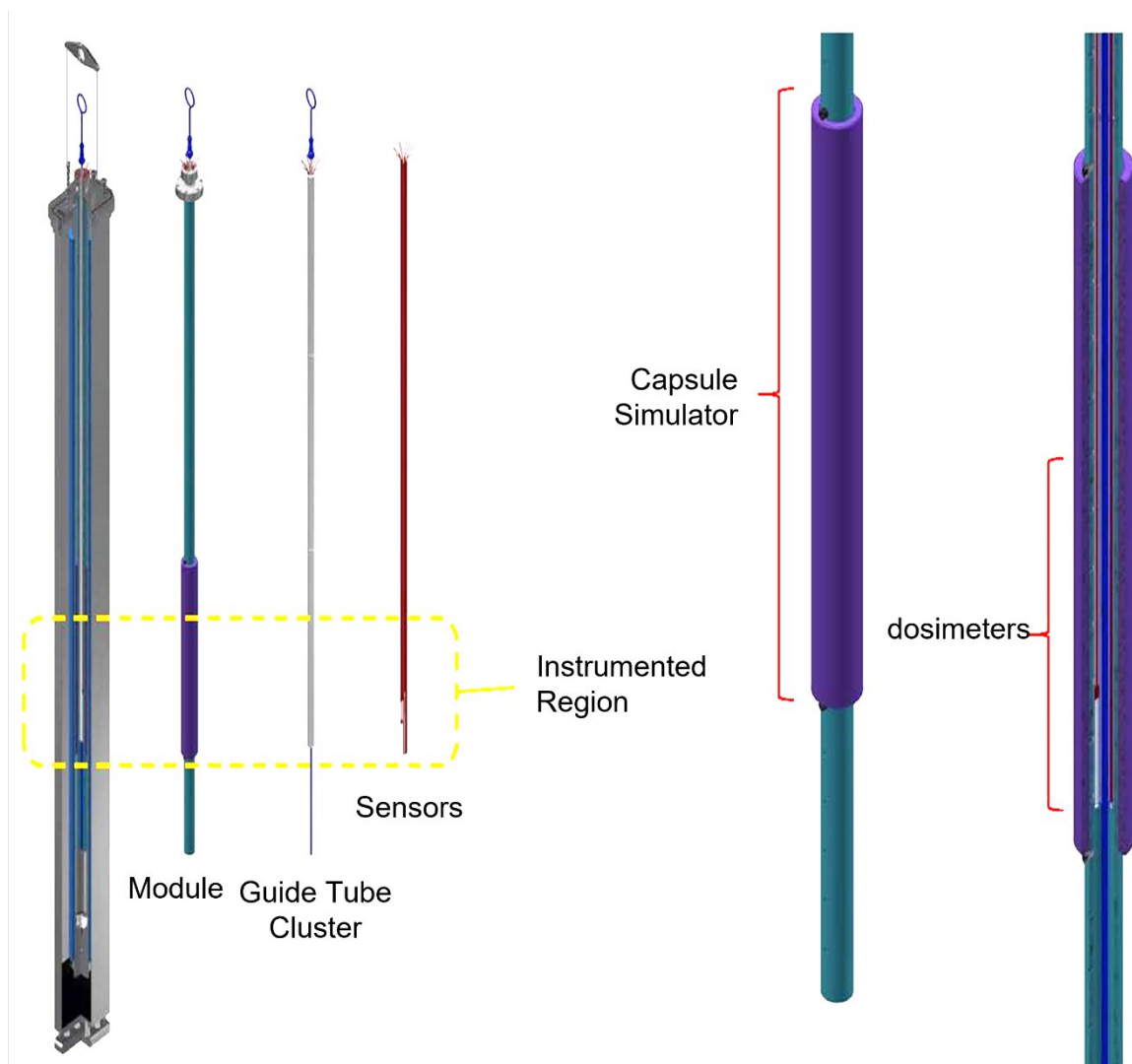
**Figure 4.4.** **The Buster assembly for MIMIC-N experiments contains a holder that is approximately 94 inches long from the top of the lifting eye to the bottom of the plug containing a titanium module, which housed the advanced manufactured dosimeters and an expanded view to highlight the designated placement of the dosimeters within the module and experiment.**

A titanium tube was used within the BUSTER assembly (**Figure 4.4**) housing which included four different sets of AMD's and classical flux foils were subjected to transient testing in TREAT. Briefly, as shown in **Figure 4.5**, the stacking sequence involved the use of a square wire facilitate orientation of the four different sets of AMDs plus the classical flux wires (**Figure 4.5a**). Furthermore, a blank alumina capsule (containing no dosimeter material) was also included with the titanium flux foils (**Figure 4.5b**). During assembly, the square wires were threaded so that each flux foil was arranged facing either N/S or E/W.
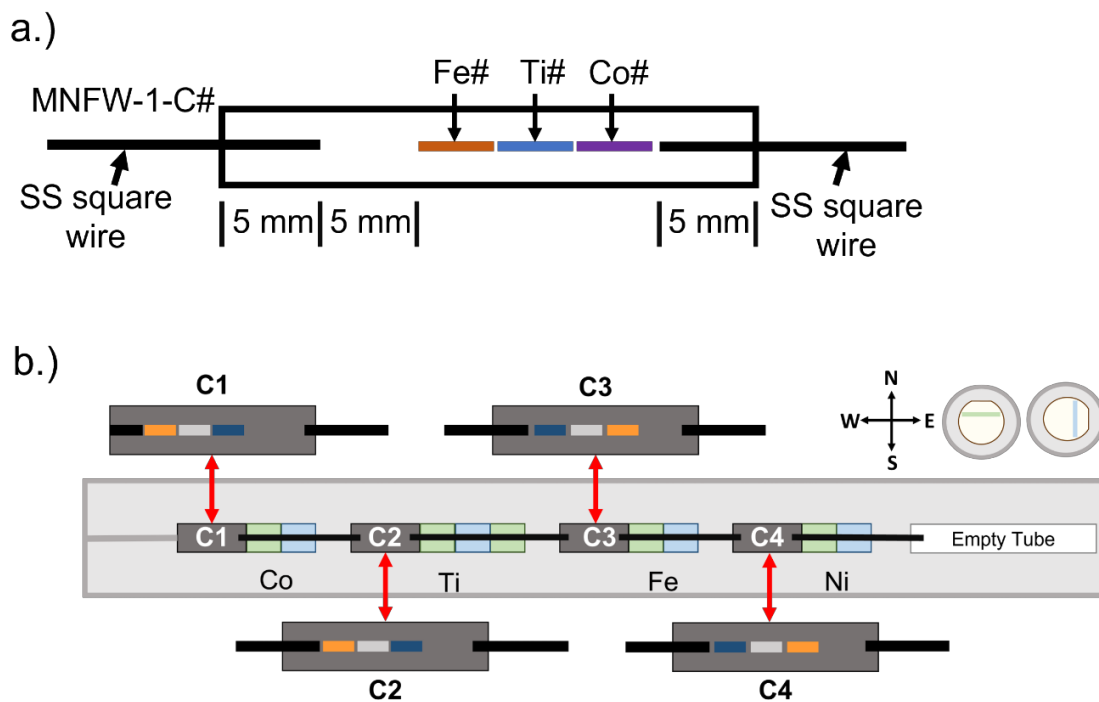


**Figure 4.5.** Schematic detailing the arrangement of dosimeters. a.) Flux wire capsules with iron, titanium and cobalt wires shown inside an aluminum tube, with the stainless steel square wire extending out both ends of the tube, and b.)schematic with flux wire capsules and AMDs assembled with the square wire within the titanium housing.

4.3.2.5 Irradiation Experiments

As part of the concurrent testing program, which is as an independent accompaniment to planned experiments at the TREAT facility, the Materials Irradiation Capability for Neutron Sensors (MIMIC-N) configuration was used for these experiments, which is configured specifically for neutron sensors and dosimeters to measure neutron flux, and the MNFW designation will be used from here on out to stand for MIMIC-N Flux Wire. Two transients (MNFW-1 and MNFW-2) were targeted and the resultant transient energy was 1029.19 MJ and 1683.76 MJ for the first and second tests, respectively. A summary of transient reactor operations for the two transients during which the AMDs were irradiated is provided in Table 4.2 where total transient energy and peak power values represent best estimates.

**Table 4.2.     Transient characteristics for MNFW-1 and MNFW-2**

|                          | Transient #1 (MNFW-1) | Transient #2 (MNFW-2) |
|--------------------------|-----------------------|-----------------------|
| **Transient Time**       | 11:04                 | 10:57                 |
| **Transient Energy (MJ)**| 1029.19               | 1683.76               |
| **Peak Power (MW)**      | 9953.65               | 10539.12              |

4.3.2.6 Gamma Spectroscopy

Following irradiation, the AMDs were measured with a High-Purity Germanium (HPGe) detector. The activation products in each AMD were quantified based on the gamma-ray spectrometry measurements. The HPGe detector is well-characterized, and the efficiency is calculated with a National Institute of Standards and Technology (NIST)-traceable calibration source as a function of distance from the detector face. Additionally, a detailed Monte-Carlo N-Particle (MCNP) model has been developed that

quantifies the impact of source geometry and photon attenuation on the detector efficiency.[16]

The AMDs were placed at various distances from the detector face. The AMD ID, material, counting time, and dead time are found in Table 4.3 and Table 4.4 for MNFW-1 and MNFW-2, respectively. It is desirable for the detector dead time to be less than 10%, as large dead times can degrade the peak resolution. In the case of the MNFW-1 and MNFW-2 AMDs, the activities were small, and the AMDs were able to be counted close to the detector face. The Co and Ni AMDs were counted at a larger distance from the detector due to higher activity. The live time is a preset in the detector configuration software and is chosen to be sufficiently long to obtain low statistics for photopeak count uncertainty.

**Table 4.3.**     **MNFW-1 AMDs Measurement Characteristics**

| AMD Number | Material | Dead Time (%) | Counting Live Time (sec) | Distance from Detector Face (mm) |
|---|---|---|---|---|
| MNFW-1-AMD1 | Cobalt | 8.90 | | 49 |
| MNFW-1-AMD2 | Cobalt | 9.80 | | 49 |
| MNFW-1-AMD3 | Titanium | 5.76 | 7200 | 9 |
| MNFW-1-AMD4 | Titanium | 6.07 | | 9 |
| MNFW-1-AMD5 | Blank | 0.44 | 76806 | 9 |
| MNFW-1-AMD6 | Iron | 2.37 | | 9 |
| MNFW-1-AMD7 | Iron | 2.61 | 7200 | 9 |
| MNFW-1-AMD8 | Nickel | 5.28 | | 29 |
| MNFW-1-AMD9 | Nickel | 6.31 | | 29 |

**Table 4.4.    MNFW-2 AMDs Measurement Characteristics**

| AMD Number | Material | Dead Time (%) | Counting Live Time (sec) | Distance from Detector Face (mm) |
|---|---|---|---|---|
| MNFW-2-AMD1 | Cobalt | 11.52 | | 89 |
| MNFW-2-AMD2 | Cobalt | 8.82 | | 89 |
| MNFW-2-AMD3 | Titanium | 0.95 | | 9 |
| MNFW-2-AMD4 | Titanium | 0.96 | | 9 |
| MNFW-2-AMD5 | Blank | 0.77 | 7200 | 9 |
| MNFW-2-AMD6 | Iron | 8.19 | | 49 |
| MNFW-2-AMD7 | Iron | 3.62 | | 49 |
| MNFW-2-AMD8 | Nickel | 7.03 | | 29 |
| MNFW-2-AMD9 | Nickel | 8.65 | | 29 |

The foils were each measured using an HPGe detector. To begin analysis, The spectra for the blank alumina dosimeter holder was collected and used as a baseline for subsequent AMD analysis.

4.3.2.7. Method of Calculation for AMDs

The calculations of isotopic activities for the AMDs are not straightforward, and accurate peak fitting and efficiency determinations are necessary to provide acceptable results. In **Figure 4.6**, the isotopic activity (red) is impacted by many different components. Nuclear data (green) is used for several variables in the calculation, and gamma-ray interferences from the "blank" AMD without an active dosimeter material and other isotopes must be taken into account. Steps that involve gamma spectrometry are contained in blue boxes, while yellow boxes indicate computational simulations are required. The largest effort involves determination of the detector efficiency for each AMD material and gamma-ray energy. The NIST-traceable calibration source ($^{152}$Eu) is measured at a distance from the detector face. However, the calibration source is not the

same material composition or geometry as the AMD. To remedy the difference, a high-fidelity MCNP simulation of the HPGe detector is used to simulate the detector efficiency with each AMD. To account for bias within the MCNP simulation, a separate simulation is created for the NIST-traceable calibration source. Then, the detector's efficiency with each AMD is determined using the experimental and simulated detector efficiencies. The gamma spectroscopy measurement of the AMDs is corrected by subtracting the contribution from blank AMDs and other interferences to obtain a final isotopic activity.

To calculate the activity for each isotope in a sample, the relevant photopeaks and nuclear data used during gamma spectroscopy are shown in Table 4.5. For all equations, Table 4.6 specifies the definition of each variable. Eq. (1) provides the equation to calculate isotope activity. The total and simplified calculation for uncertainty is shown in Eq. (2) and Eq. (3), respectively, in a manner concurrent with the root mean square method of uncertainty propagation. The definition of the partial derivative in Eq. (4) is required for the uncertainty calculation.
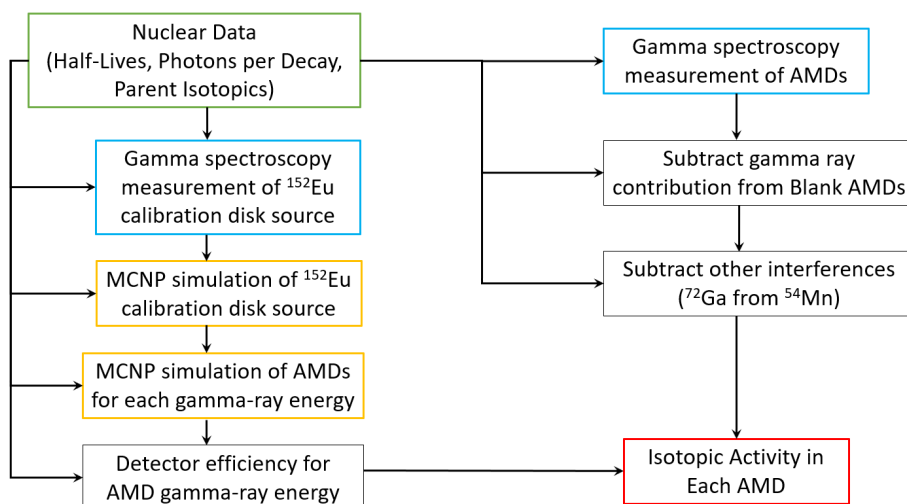


**Figure 4.6.     Flow chart for calculation of activity in AMDs**

$$A_i = \frac{\lambda_i C_i e^{\lambda_i t_d}}{\left(1 - e^{\lambda_i t_c}\right) \varepsilon_i \eta_i} \tag{1}$$

$$\sigma_{A_i} = \left(\left(\frac{\partial A_i}{\partial C_i}\sigma_{C_i}\right)^2 + \left(\frac{\partial A_i}{\partial \varepsilon_i}\sigma_{\varepsilon_i}\right)^2 + \left(\frac{\partial A_i}{\partial \lambda_i}\sigma_{\lambda_i}\right)^2 + \left(\frac{\partial A_i}{\partial \eta_i}\sigma_{\eta_i}\right)^2\right)^{1/2} \tag{2}$$

$$\sigma_{A_i} = A_i\left(\left(\frac{\sigma_{C_i}}{C_i}\right)^2 + \left(\frac{\sigma_{\varepsilon_i}}{\varepsilon_i}\right)^2 + \frac{1}{A_i^2}\left(\frac{\partial A_i}{\partial \lambda_i}\sigma_{\lambda_i}\right)^2 + \left(\frac{\sigma_{\eta_i}}{\eta_i}\right)^2\right)^{1/2} \tag{3}$$

$$\frac{\partial A_i}{\partial \lambda_i} = \frac{A_i}{\lambda_i}\left(\frac{\lambda_i t_d + 1 - e^{-\lambda_i t_c}\left(\lambda_i t_d + 1 + \lambda_i t_c\right)}{1 - e^{-\lambda_i t_c}}\right) \tag{4}$$

**Table 4.5.    Nomenclature for Equation Variables**

| Variable | Description |
|---|---|
| $C_i$ | Photopeak counts (area) of gamma-ray from isotope $i$ |
| $\lambda_i$ | Decay constant of isotope $i$ (sec$^{-1}$) |
| $\varepsilon_i$ | Absolute detector efficiency of gamma-ray emitted by isotope $i$ |
| $\eta_i$ | Quantum yield of gamma-ray per disintegration of isotope $i$ |
| $\sigma_x$ | Uncertainty of quantity $x$ |
| $A_i$ | Activity of isotope $i$ (Bq) |
| $t_c$ | Counting live time (sec) |
| $t_d$ | Decay time between T-zero and measurement (sec) |

## 4.4 Results and Discussion

4.4.1. AMD Results

For gamma spectrometry of the AMDs, each gamma ray of interest must be quantified, and multiple gamma rays from the same isotope are used to reduce the uncertainty of the production of the radioisotope. The measurements of the MNFW-1 Ti, Fe, Co, and Ni AMDs are shown in **Figure 4.7-4.10** with the blank AMD from MNFW-1

shown in blue and the AMD with active material shown in black. Note in each figure the large number of photopeaks in each gamma-ray spectrum.

The results for the ratios of the East/West facing to the North/South facing AMDs for each test are found in Table 4.6 through Table 4.8. The fast neutron reactions are found in Tables 4.6 and 4.7, while the thermal neutron reactions are found in Table 4.8. For the reactions in Table 4.6, there are observable radioisotopes in all the AMDs measured.
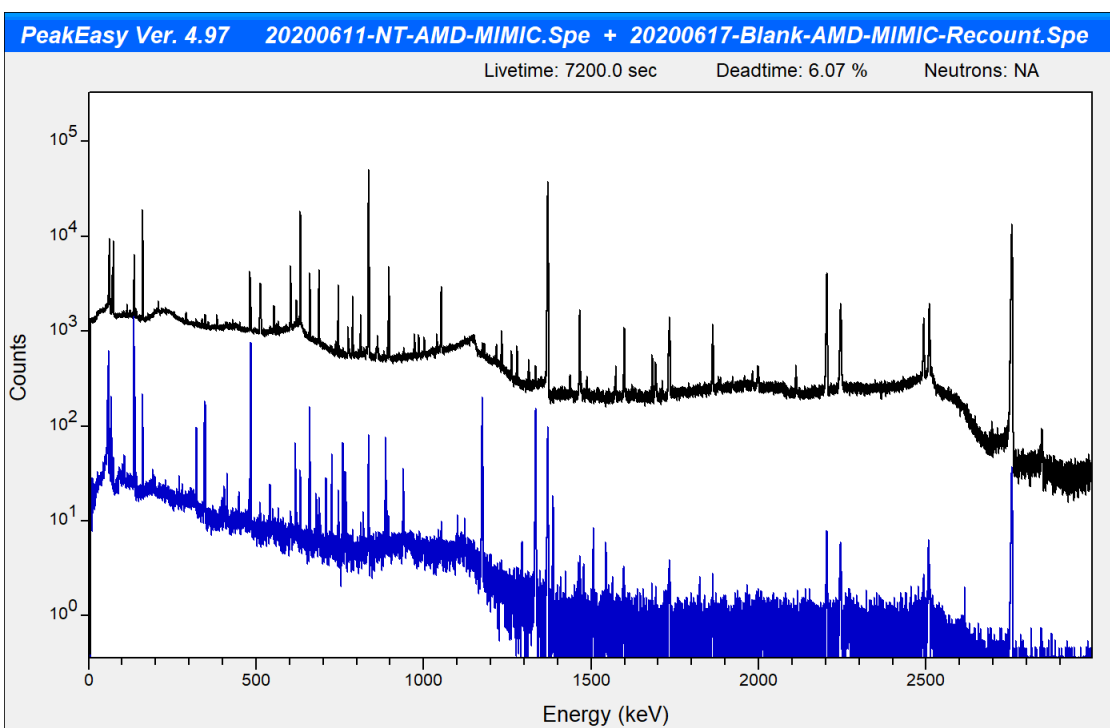


**Figure 4.7.** **Comparison plot of MNFW-1 North/South Titanium AMD (black) and MNFW-1 "Blank" AMD (blue)**
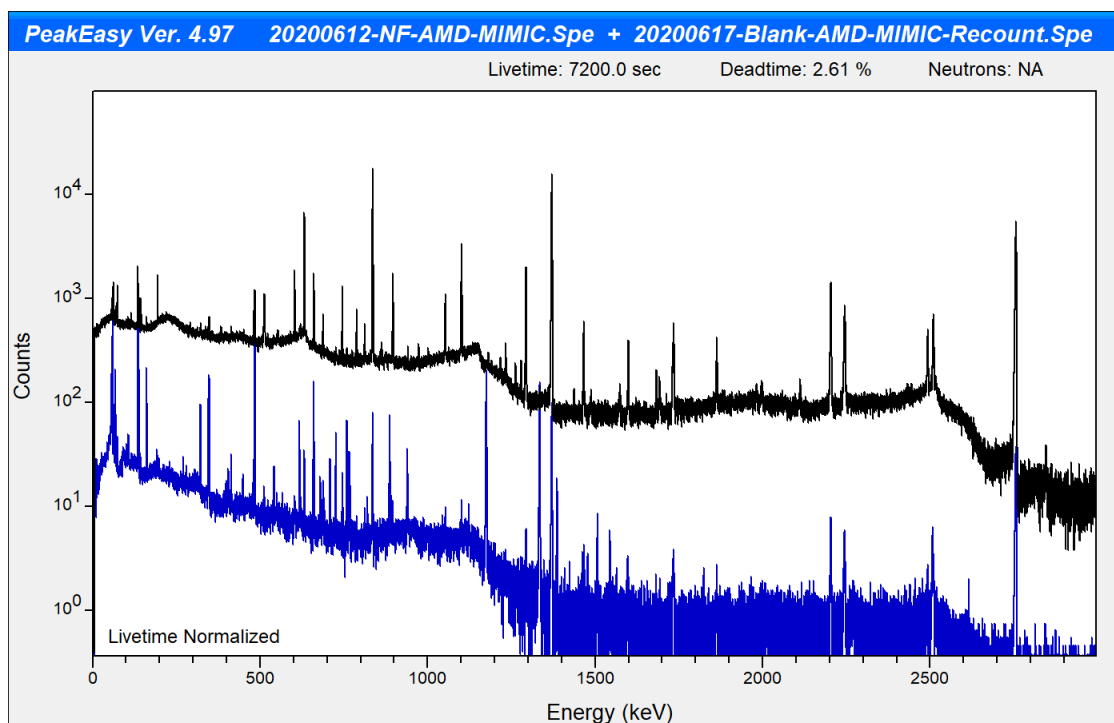
**Figure 4.8.    Comparison plot of MNFW-1 North/South Iron AMD (black) and MNFW-1 "Blank" AMD (blue)**
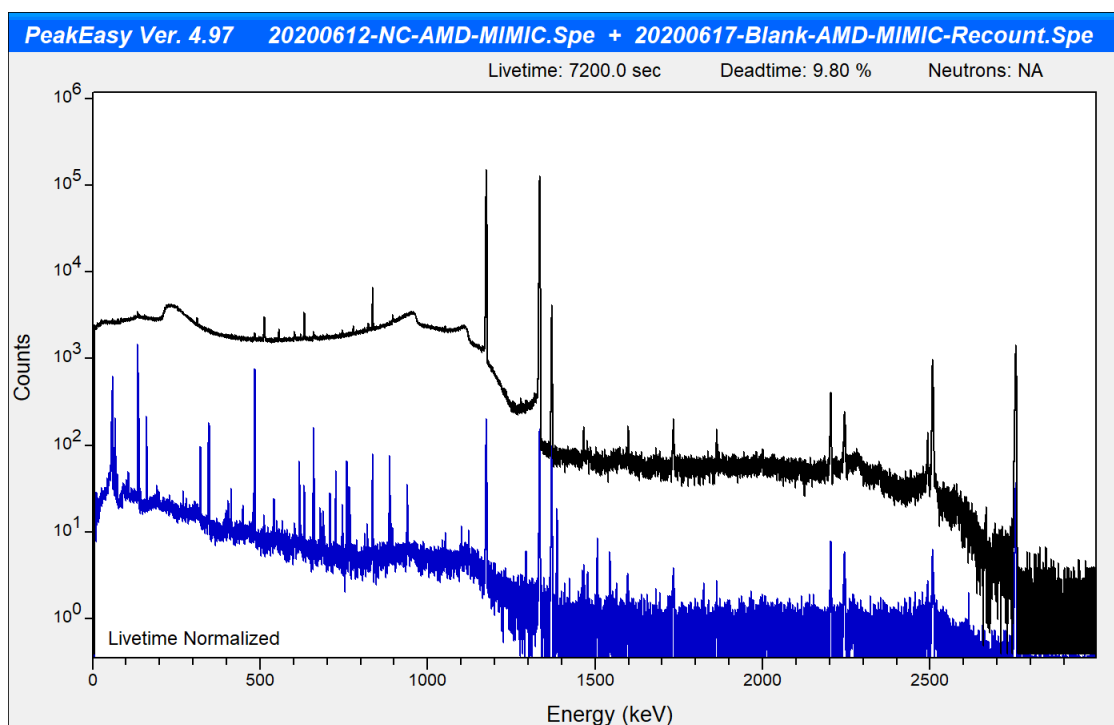


**Figure 4.9.    Comparison plot of MNFW-1 North/South Cobalt AMD (black) and MNFW-1 "Blank" AMD (blue)**
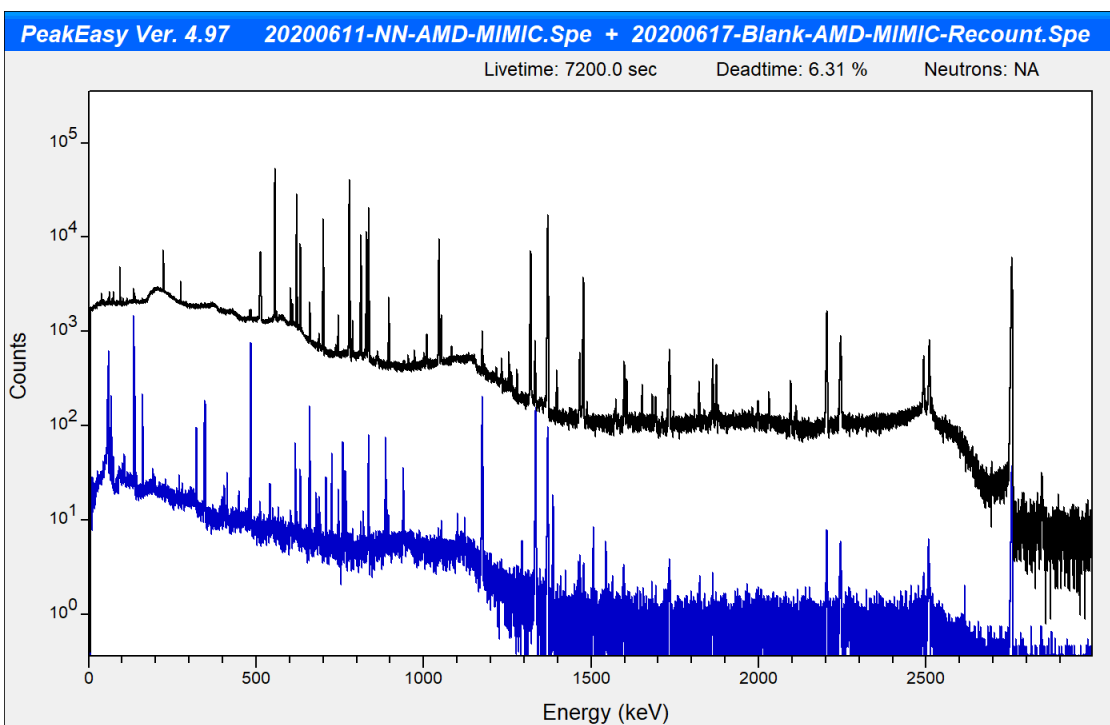
**Figure 4.10.   Comparison plot of MNFW-1 North/South Nickel AMD (black) and MNFW-1 "Blank" AMD (blue)**

observed inconsistencies in the alumina constituents can influence the ratio and associated uncertainty. For example, in Table 4.6, the reaction for $^{54}$Mn is observable in all AMD materials, but the uncertainties in some AMDs ($^{54}$Mn in the MNFW-2 Fe AMD) have exceedingly large uncertainties due to the interferences of impurities, specifically $^{72}$Ga, which emits an 834 keV photon similar to $^{54}$Mn. The intended reactions for AMDs are shown in orange in Table 4.6.

For the ratios observed with acceptable statistics, the following conclusions can be made:

- Based on $^{54}$Fe (n,p), there are no comparisons that can be made between MNFW-1 and MNFW-2 due to the statistics in the MNFW-2 AMD. Within statistical uncertainty, the East/North flux appear to be equivalent in each transient, MNFW-1 and MNFW-2.

- Based on $^{58}$Ni (n,p) in Table 4.6, the East/North flux ratio was equivalent in MNFW-1 but decreases for MNFW-2.

- Based on $^{46}$Ti (n,p), $^{47}$Ti (n,p), $^{48}$Ti (n,p), and $^{60}$Ni (n,p) in Table 4.7, the East/West flux to North/South flux was approximately 1, and equal within statistics for MNFW-1 and MNFW-2.

- Based on $^{58}$Fe (n,γ) and $^{59}$Co (n,γ) in Table 4.8, the East/North flux ratio was less in MNFW-1 than MNFW-2. In MNFW-1, the East/West thermal flux was less than or equal to the North/South thermal flux. However, in MNFW-2, the East/West thermal flux was about 20% higher than the North/South direction.

**Table 4.6.    Ratio Results for Fast Neutron Reactions**

| | | | $^{54}$Fe (n,p) $^{54}$Mn | | $^{58}$Ni (n,p) $^{58}$Co | |
|---|---|---|---|---|---|---|
| | Active Material | Test | Ratio | Uncertainty (k = 1) | Ratio | Uncertainty (k = 1) |
| East/North | Nickel | MNFW-1 | 1.328 | 0.463 | 1.041 | 0.027 |
| | Titanium | | 0.970 | 0.208 | 0.969 | 0.039 |
| | Cobalt | | 1.208 | 0.949 | 0 | 0 |
| | Iron | | 0.705 | 0.169 | 0.724 | 0.050 |
| | Nickel | MNFW-2 | 3.063 | 1.551 | 0.667 | 0.017 |
| | Titanium | | 32.85 | 348.27 | 0 | 0 |
| | Cobalt | | 0 | 0 | 0.862 | 0.183 |
| | Iron | | 2.377 | 2.691 | 2.530 | 0.096 |

**Table 4.7.    Ratio Results for Fast Neutron Reactions**

| | | $^{46}$Ti (n,p) $^{46}$Sc | | $^{47}$Ti (n,p) $^{47}$Sc | | $^{48}$Ti (n,p) $^{48}$Sc | | $^{60}$Ni (n,p) $^{60}$Co | |
|---|---|---|---|---|---|---|---|---|---|
| | | Ratio | Unc. (k = 1) | Ratio | Unc. (k = 1) | Ratio | Unc (k = 1) | Ratio | Unc (k = 1) |
| East/North | MNFW-1 | 0.903 | 1.600 | 1.154 | 0.035 | 1.032 | 0.067 | 0 | 0 |
| | MNFW-2 | 1.191 | 0.066 | 1.000 | 0.030 | 1.026 | 0.056 | 0.377 | 0.019 |

**Table 4.8.    Ratio Results for Thermal Neutron Reactions**

| | | $^{58}$Fe (n,γ) $^{59}$Fe | | $^{59}$Co (n,γ) $^{60}$Co | |
|---|---|---|---|---|---|
| | | Ratio | Uncertainty (k = 1) | Ratio | Uncertainty (k = 1) |
| East/North | MNFW-1 | 0.631 | 0.023 | 0.987 | 0.027 |
| | MNFW-2 | 1.213 | 0.060 | 1.245 | 0.034 |

For the differences in the fast neutron reactions, the approximate threshold energies are given in Table 4.9. The only fast reaction that showed a difference was 58Ni (n,p), which has a 3 MeV neutron energy threshold. The only reaction with a larger threshold energy is 54Mn (n,p), which could not be quantified with small uncertainty due to the interference with 72Ga. As a result, it could be inferred that the neutron population with an energy above 3 MeV was smaller in the East/West direction for MNFW-2. Correspondingly, the thermal neutron reactions showed a higher thermal flux in the East/West direction for MNFW-2.

**Table 4.9.** **Radioactive Daughter Products and Properties**

| Reaction | Approximate Energy Threshold (MeV) | Half-Life (days) | Unc (k = 1) | Gamma Ray Energy (keV) | Photons per Disintegration ($10^{-2}$) | Unc (k = 1) |
|---|---|---|---|---|---|---|
| $^{46}$Ti (n,p) $^{46}$Sc | 2 | 83.79 | 3456 | 889.28 | 99.98 | 1.00E-05 |
| | | | | 1120.6 | 99.99 | 1.00E-05 |
| $^{47}$Ti (n,p) $^{47}$Sc | 1 | 3.349 | 51.84 | 159.38 | 68.30 | 4.00E-03 |
| $^{48}$Ti (n,p) $^{48}$Sc | 4 | 1.819 | 324 | 175.36 | 7.48 | 9.75E-04 |
| | | | | 983.53 | 1.00 | 5.83E-03 |
| | | | | 1037.5 | 97.61 | 6.99E-03 |
| | | | | 1312.1 | 100.11 | 7.08E-03 |
| $^{54}$Fe (n,p) $^{54}$Mn | 1 | 312.1 | 3456 | 834.85 | 99.98 | 4.01E-06 |
| $^{58}$Fe (n,γ) $^{59}$Fe | - | 44.50 | 777.6 | 142.65 | 1.02 | 4.45E-04 |
| | | | | 192.34 | 3.08 | 1.16E-03 |
| | | | | 1099.3 | 56.50 | 1.84E-02 |
| | | | | 1291.6 | 43.20 | 1.37E-02 |
| $^{59}$Co (n,γ) $^{60}$Co | - | 1925 | 12096 | 1173.2 | 99.85 | 3.00E-04 |
| | | | | 1332.5 | 99.98 | 6.00E-06 |
| $^{59}$Co (n,2n) $^{58}$Co | 10 | 70.86 | 5184 | 810.759 | 99.45 | 1.00E-04 |
| $^{58}$Ni (n,p) $^{58}$Co | 0.5 | 70.86 | 5184 | 810.759 | 99.45 | 3.00E-04 |
| $^{60}$Ni (n,p) $^{60}$Co | 3 | 1925 | 12096 | 1173.23 | 99.85 | 3.00E-04 |
| | | | | 1332.49 | 99.98 | 6.00E-06 |
| $^{71}$Ga (n,γ) $^{72}$Ga | - | 0.588 | 36 | 834.13 | 95.45 | 7.67E-04 |
| | | | | 894.327 | 10.14 | 1.48E-04 |

4.4.2. Discussion

Several AMDs were produced with various elemental metals chosen for their traditional use in reactor dosimetry: Ti, Fe, Co, and Ni. The metals were additively manufactured to create an AMD (gray) with a small profile in the X-direction, shown in **Figure 4.11a**, with the objective of eliminating the contributions of the neutron flux from several directions, shown in red arrows. Therefore, the activation of the radioisotopes

from the neutron flux in the reactor should only be produced from neutrons traveling with some component of the green arrows in **Figure 4.11a**. However, this directional dependency of the neutrons is impacted by the AMD metals.
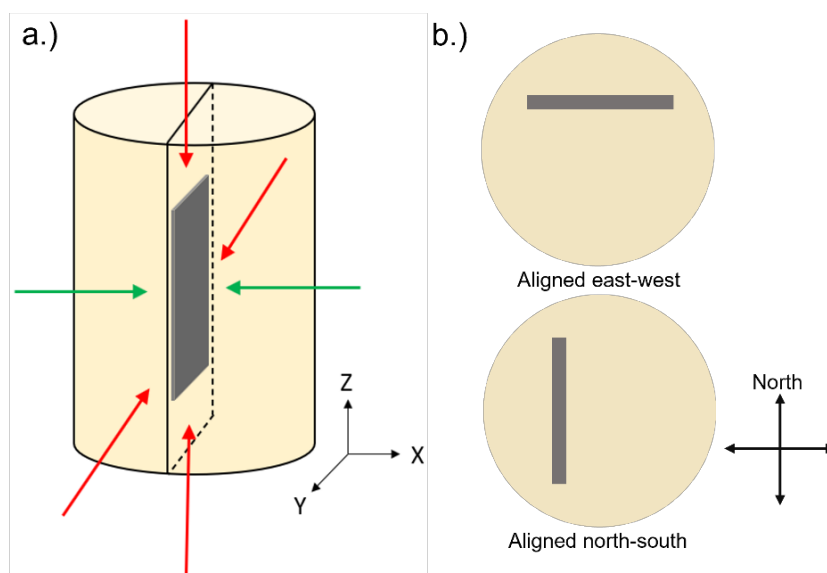


**Figure 4.11.   Representative image of AMD (gray) inside alumina (tan). Using AM the AMDs were a.) manufactured to create an AMD with a small profile in the X-direction, and the b.) top-view of AMD alignment in east-west and north-south directions.**

For example, neutrons traveling in the positive x-direction have a large physical cross section relative to neutrons traveling in the positive y-direction. However, the neutrons traveling in the positive x-direction have a small thickness of AMD material while the positive y-direction have a larger thickness of AMD material with which to interact. Nominal values of the macroscopic cross sections and calculated mean free paths (inverse of macroscopic cross section) shown in Table 4.10.[17] The total macroscopic cross section is typically used in mean free paths; however, the absorption macroscopic cross section is used for the calculation of mean free path since activation of the AMD metal is of interest rather than total interaction. Therefore, if the mean free path

of the AMD element is comparable to the physical dimensions of the AMD, the

directional contributions will be equivalent between the normal (intended green arrow

paths) and the orthogonal (un-intended red arrow paths) directions. The AMDs metal is

approximately 1x0.5x0.5 mm, which indicates from Table 4.10 the Co AMDs are ill-

suited for directional determination using the AMDs. However, cobalt was included due

to its wide use in reactor dosimetry and allows for comparisons with irradiations of cobalt

in traditional flux wires.

**Table 4.10.   Neutron mean free path in AMD Materials**

|  | Macroscopic Absorption Cross Section (cm$^{-1}$) | Mean Free Path (cm) |
|---|---|---|
| Al$^*$ | 0.015 | 66.67 |
| Ti | 0.328 | 3.05 |
| Fe | 0.222 | 4.50 |
| Co | 3.460 | 0.29 |
| Ni | 0.420 | 2.38 |

The AMDs were contained within an alumina material (tan) to maintain control of

the total material during the reactor transient. Then, by incorporating two AMDs closely

spaced axially, the orientations of the AMDs can be made orthogonal, and comparisons

can be made between the two directions of the flux. It is important to note that these

AMD measurements cannot quantify neutron *current* because it allows for neutrons to

interact with the AMDs in two directions, and these values accumulate rather than negate

each other. In TREAT, each set of two AMDs with the same material were positioned

orthogonally with one set facing east/west and the other facing north/south, which is

demonstrated in **Figure 4.11b.**

4.4.2. AMD Reactions

Within the alumina housing the AMDs consist of parent materials of Ti, Fe, Co, and Ni and the isotopic abundances used in this work were taken from ENDF/B, which are presented with associated uncertainties in Table 4.11.[18] Parent materials were selected so that each isotope in the parent material had sensitivities to particular neutron reactions, and those reactions are described in Table 4.9, which includes the approximate neutron energy threshold in MeV (thermal neutron reactions don't have a threshold energy) as well as the half-lives, gamma-ray energies, and photons emitted at those energies per disintegration including associated uncertainties. In addition to the parent materials, an extra AMD element, gallium (Ga), is included in Table 4.9 and Table 4.11, due to its abundant daughter product, $^{72}$Ga, having a large number and amplitude of gamma-rays measured during spectrometry. The substantial contribution from $^{72}$Ga degrades the fidelity of the gamma-ray photopeaks from other elements, particularly $^{54}$Mn. The origin of the Ga could be the alumina surrounding the AMD due to Ga's similar chemistry to aluminum during production of the alumina material.

Compared to traditional flux wires, the AMDs were found to contain a substantial number of "extra" elements, and the total list of observable radioisotopes during gamma spectrometry of the AMDs can be found in Table 4.12. In a traditional flux wire, only the radioisotopes marked with a black X would be found. However, numerous additional photopeaks were observed, which decrease the resolution of the photopeaks of interest.

**Table 4.11.    Parent Isotopic Abundances**

| AMD Element | Isotope | Fractional Abundance | Uncertainty (k = 1) |
|---|---|---|---|
| Ti | $^{46}$Ti | 0.0825 | 0.0003 |
| | $^{47}$Ti | 0.0744 | 0.0002 |
| | $^{48}$Ti | 0.7372 | 0.0003 |
| Fe | $^{54}$Fe | 0.05845 | 0.00035 |
| | $^{58}$Fe | 0.00282 | 0.00004 |
| Co | $^{59}$Co | 1 | 0 |
| Ni | $^{58}$Ni | 0.68077 | 0.00019 |
| | $^{60}$Ni | 0.26223 | 0.00015 |
| Ga | $^{71}$Ga | 0.39892 | 0.00009 |

**Table 4.12.    Radioisotopes identified during gamma spectroscopy for AMDs**

| | X = found in both AMD and flux wires | X = found only in AMDs | | | | |
|---|---|---|---|---|---|---|
| | | MNFW-1 East/West AMDs | | | | |
| | Parent Element | Cobalt | Iron | Nickel | Titanium | Blank |
| $^{24}$Na | Na or Al | X | X | X | X | X |
| $^{46}$Sc | Sc or Ti | | | | X | X |
| $^{47}$Sc | Ti | | X | X | X | X |
| $^{48}$Sc | Ti | | | | X | |
| $^{51}$Cr | Cr or Fe | | | | | X |
| $^{54}$Mn | Fe or Mn | X | X | X | X | X |
| $^{59}$Fe | Fe | | X | | | X |
| $^{58}$Co | Co or Ni | X | X | X | X | X |
| $^{60}$Co | Co or Ni | X | X | X | X | X |
| $^{72}$Ga | Ga | X | X | X | X | X |
| $^{82}$Br | Br | X | | X | | |
| $^{95}$Zr | Zr | | | | | X |
| $^{97}$Zr | Zr | X | X | X | X | X |
| $^{110m}$Ag | Ag | | | | | X |
| $^{181}$Hf | Hf | X | X | X | X | X |
| $^{187}$W | W | X | X | X | X | X |
| $^{198}$Au | Au | | | | | X |

**Table 4.13.    AMD feedstock key constituents and impurities**

| | Percent Composition (%) | | | |
|---|---|---|---|---|
| | $Co_3O_4$ | Ni | Fe | Ti |
| Al | 0 | 0 | ≤0.091 | <0.0005 |
| As | 0 | <0.001 | 0 | 0 |
| Bi | 0 | <0.0005 | 0 | 0 |
| C | 0 | 0 | 0 | <0.02 |
| Ca | 0.001 | 0 | ≤0.0044 | 0 |
| Cd | 0 | <0.001 | 0 | 0 |
| Co | 73.2 | <0.002 | 0 | 0 |
| Cr | 0 | 0 | ≤0.015 | 0 |
| Cu | 0.001 | 0 | ≤0.005 | 0 |
| Fe | 0.01 | 0 | 99.9 | <0.05 |
| Hg | 0 | <0.001 | 0 | 0 |
| K | 0.01 | 0 | 0 | 0 |
| Mg | 0.001 | <0.001 | ≤0.004 | 0 |
| Mn | 0 | 0 | ≤0.13 | 0 |
| Mo | 0 | 0 | ≤0.024 | <0.0002 |
| N | 0 | 0 | 0 | <0.02 |
| Na | 0.01 | 0 | 0 | 0 |
| Ni | 0.01 | >99.9 | ≤0.12 | 0 |
| O | 26.757 | 0 | 0 | 0 |
| P | 0 | <0.001 | 0 | 0 |
| Pb | 0 | <0.001 | ≤0.004 | 0 |
| Sb | 0 | <0.001 | 0 | 0 |
| Si | 0 | <0.001 | ≤0.02 | <0.0003 |
| Sn | 0 | <0.001 | ≤0.008 | 0 |
| Ti | 0 | 0 | ≤0.005 | >99.9 |

More specifically, in **Figure 4.12a**., a gamma ray spectrum for both an AMD and a traditional flux wire, both containing iron, are shown in black and blue, respectively. For the AMD, a larger mass of iron was used causing the black plot to be higher than the blue (traditional flux wire). Aside from the higher counts, comparison of the two plots, there are numerous additional photopeaks observable, and The plot in **Figure 4.12b** shows an annotated view of the black plot in **Figure 4.12a** with a large number of isotopes not related to Fe (only $^{59}$Fe and $^{54}$Mn are photopeaks of interest).

In Table 4.12, a large number of elements, indicated with a red "X", are observable in the respective AMDs. According to the AMD feedstock certificates, with values found in Table 4.13, there are not many elements with large impurities. Since the certificate AMD feedstock information shows a limited number of impurities, it is likely that the impurities found during gamma-ray spectrometry are contained within the alumina material. As can be seen in Table 4.12, most of the measured impurities appear in the alumina without an AMD (Blank specimen). Though it may contain a low concentration of impurities, the relative mass of the alumina compared to the mass of the AMD material, detailed in Table 4.3 and Table 4.4, can have a large effect. In particular, three isotopes, $^{24}$Na, $^{72}$Ga, and $^{181}$Hf, highlighted in orange boxes in Table 4.12, have a large number of gamma rays and provide substantial interferences to desired gamma-ray signatures.

To assess the activation of the alumina encapsulation material and to understand their photopeak contribution during gamma spectroscopy of the irradiated AMDs, a blank AMD was installed for each test, MNFW-1 and MNFW-2. From gamma spectrometry performed for each of these samples, the impurities within the blank samples were not consistent, as shown in the comparative gamma-ray spectra for each blank AMD in **Figure 4.13**. An annotated view of **Figure 4.13a**. is presented in **Figure 4.13b** for an energy range of 500 to 1000 keV. There are several radioisotopes present in the black spectrum (MNFW-1) that are vacant from the blue spectrum (MNFW-2). In particular, $^{110m}$Ag and higher levels of $^{95}$Zr and $^{181}$Hf are present in MNFW-1 and not MNFW-2. The basis for this discrepancy is not currently understood.
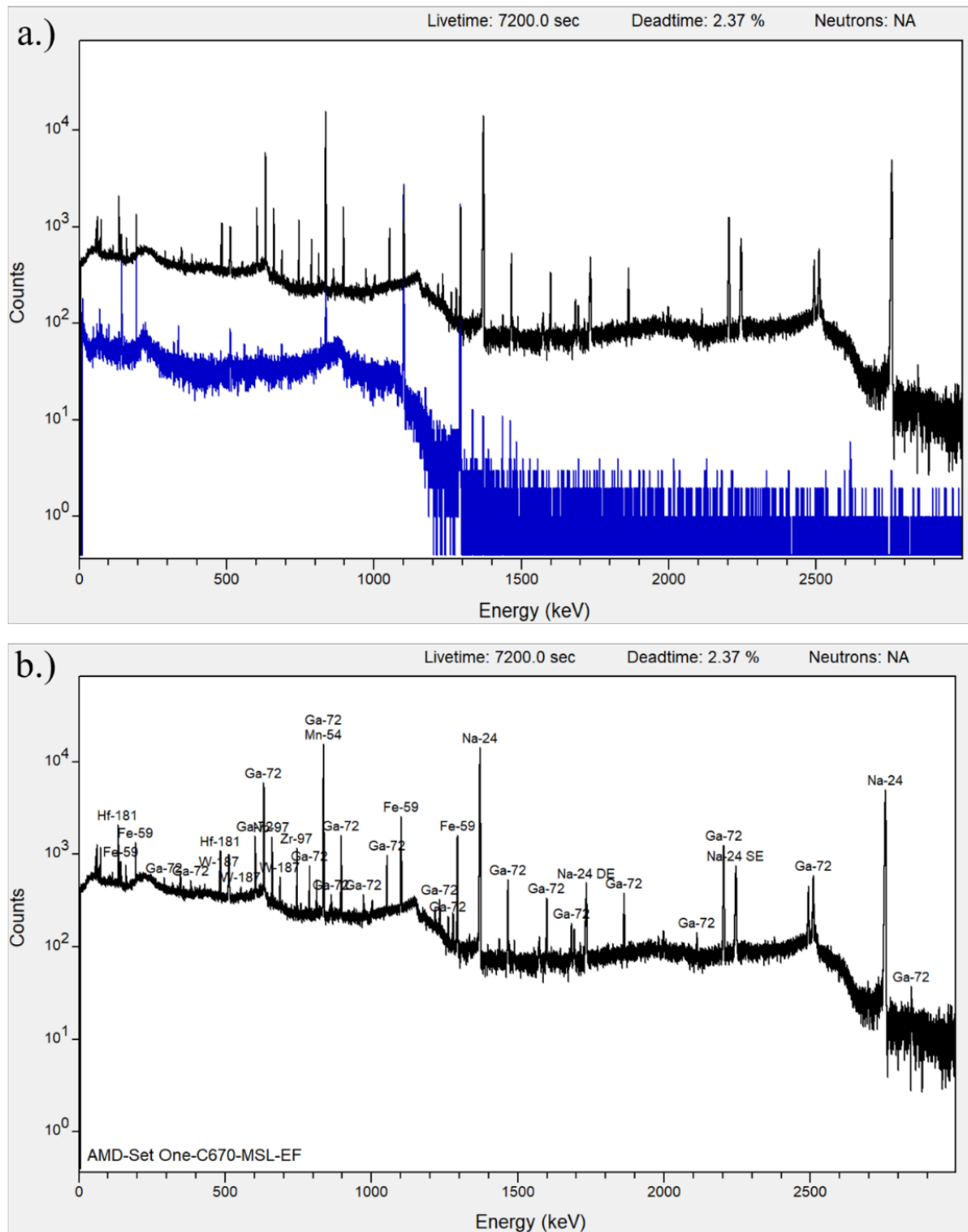
Figure 4.12. Photopeaks of iron dosimeters from MNFW-1. Comparison of (a.) traditional (blue) and East/West AMD photopeaks observed with gamma spectroscopy after irradiation, and (b.) an annotated spectra of the iron East/West AMD identifying all observed photopeaks.

Figure 4.13.    Comparison of "Blank" AMD photopeaks. (a.) Gamma ray spectrum for blank AMDs irradiated in MNFW-1 (blue) and MNFW-2 (black), and the (b.) annotated spectrum identifying all radioisotopes observed from 500-1000 keV.

**4.5. Conclusion**

In summary, advanced manufactured dosimeters were fabricated using DLP and MDP techniques and were irradiated in TREAT. The resulting gamma spectroscopy results revealed asymmetry in the neutron flux under some test conditions, though impurities in the AMD materials prevented the full utilization of their associated nuclear r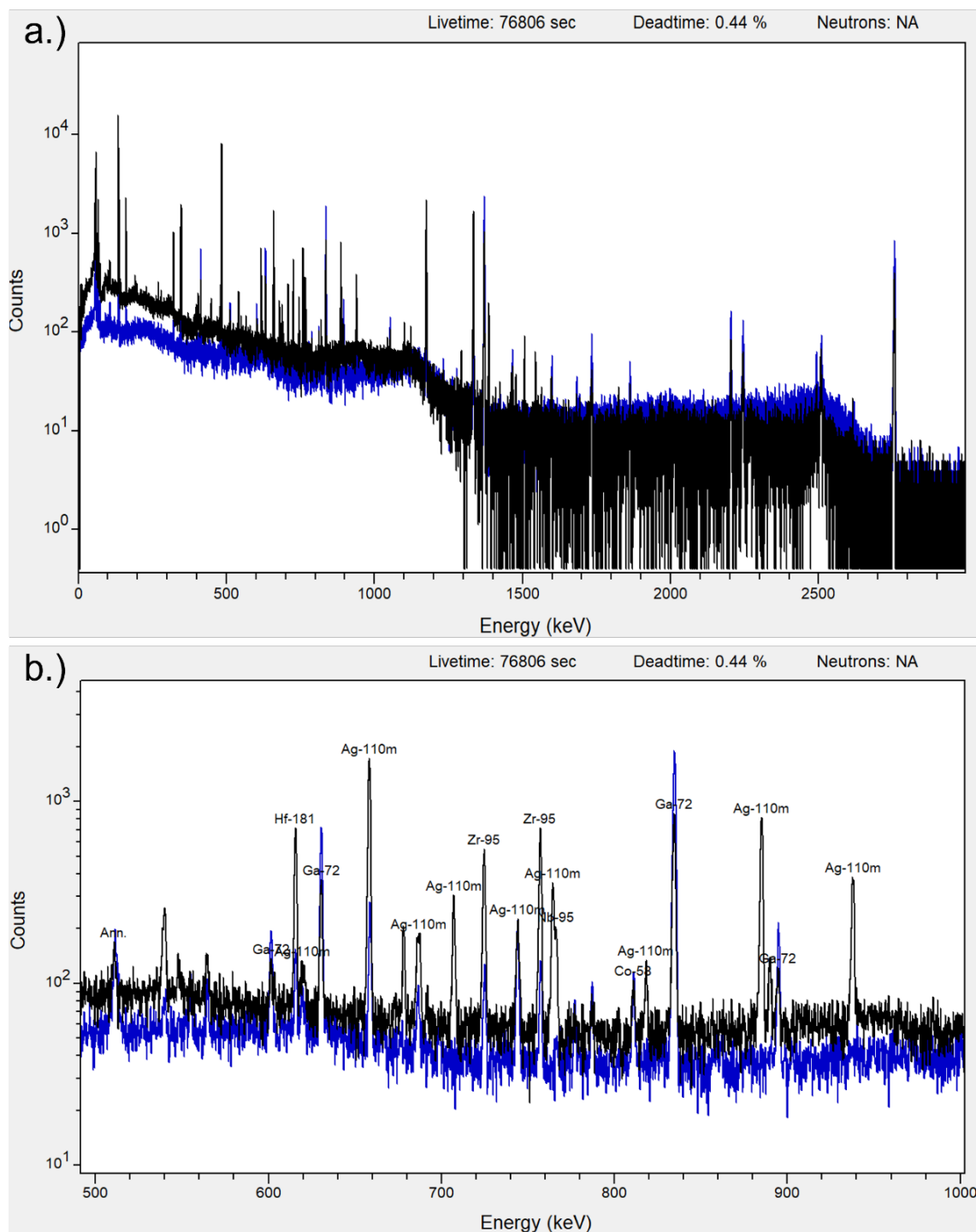eactions. Initial results demonstrate the importance of future work for AMDs and the impact that directional flux may have upon an experiment, as neutron flux can influence local reactivity changes as well as thermal hydraulic conditions within an experiment. However, further investigations into the experimental design and set-up will need to be performed to attribute the differences between the East/West and North/South directions in the MNFW-2 experiment and the East/West to the North/South ratio between MNFW-1 and MNFW-2.

With the ultimate goal of the AMDs being to use the results in the interpretation of the neutron spectrum with specialized software useful for neutron dosimetry and radiation damage calculations.[19] However, the statistics of the AMD results must be improved to provide reliable results for an adjusted spectrum prior to their use or replacement of traditional flux wires.

## 4.6. References

1.  Freund, G., Iskenderian, H. & Okrent, D. TREAT, a pulsed graphite-moderated reactor for kinetic experiments. in *Proc. 2nd United Nations Int. Conf. Peac. Uses At. Energy* 461–475 (US Government Printing Office, 1958).

2.  Pope, C. L., Jensen, C. B., Gerstner, D. M. & Parry, J. R. Transient Reactor Test (TREAT) Facility Design and Experiment Capability. *Nucl. Technol.* **205,** 1378–1386 (2019).

3.  Holschuh, T., Woolstenhulme, N., Baker, B., Bess, J., Davis, C. & Parry, J. Transient Reactor Test Facility Advanced Transient Shapes. *Nucl. Technol.* **205,** 1346–1353 (2019).

4.  Wachs, D. M. Transient testing of nuclear fuels and materials in the United States. *Jom* **64,** 1396–1402 (2012).

5.  Carmack, J., Goldner, F., Shannon M, B. S. & Snead, L. L. Overview of the U.S. DOE accident tolerant fuel development program. *LWR Fuel Perform. Meet. Top Fuel 2013* **2,** 734–739 (2013).

6.  Inl, T. & National, E. Alternatives Analysis for the Resumption of Transient Testing Program. (2013).

7.  DeHart, M. D., Baker, B. A. & Ortensi, J. Interpretation of energy deposition data from historical operation of the transient test facility (TREAT). *Nucl. Eng. Des.* **322,** 504–521 (2017).

8.  Calignano, F., Manfredi, D., Ambrosio, E. P., Biamino, S., Lombardi, M., Atzeni, E., Salmi, A., Minetola, P., Iuliano, L. & Fino, P. Overview on additive manufacturing technologies. *Proc. IEEE* **105,** 593–612 (2017).

9.  Kruth, J. P., Leu, M. C. & Nakagawa, T. Progress in additive manufacturing and rapid prototyping. *CIRP Ann. - Manuf. Technol.* **47,** 525–540 (1998).

10. De Camargo, I. L., Erbereli, R., Taylor, H. & Fortulan, C. A. 3Y-TZP DLP additive manufacturing: Solvent-free slurry development and characterization. *Mater. Res.* **24,** 2–9 (2021).

11.    Medellin, A., Du, W., Miao, G., Zou, J., Pei, Z. & Ma, C. Vat photopolymerization 3d printing of nanocomposites: A literature review. *J. Micro Nano-Manufacturing* **7,** (2019).

12.    Appuhamillage, G. A., Chartrain, N., Meenakshisundaram, V., Feller, K. D., Williams, C. B. & Long, T. E. 110th Anniversary: Vat Photopolymerization-Based Additive Manufacturing: Current Trends and Future Directions in Materials Design. *Ind. Eng. Chem. Res.* **58,** 15109–15118 (2019).

13.    Vasquez, S., Petrelli, M., Angeli, M. C., Costa, J., Avancini, E., Cantarella, G., Munzenrieder, N., Lugli, P. & Petti, L. Cost-effective, mask-less, and high-throughput prototyping of flexible hybrid electronic devices using dispense printing and conductive silver ink. *2021 5th IEEE Electron Devices Technol. Manuf. Conf. EDTM 2021* 11–13 (2021). doi:10.1109/EDTM50988.2021.9420858

14.    Church, K., MacDonald, E., Clark, P., Taylor, R., Paul, D., Stone, K., Wilhelm, M., Medina, F., Lyke, J. & Wicker, R. Printed electronic processes for flexible hybrid circuits and antennas. *2009 Flex. Electron. Displays Conf. Exhib. FLEX 2009* (2009). doi:10.1109/FEDC.2009.5069282

15.    Holschuh, T., Watson, S. & Chichester, D. Metrology for Transient Reactor Characterization Using Uranium Wires. *Nucl. Technol.* **205,** 1336–1345 (2019).

16.    Goorley, T., James, M., Booth, T., Brown, F., Bull, J., Cox, L. J., Durkee, J., Elson, J., Fensin, M., Forster, R. A., Hendricks, J., Hughes, H. G., Johns, R., Kiedrowski, B., Martz, R., Mashnik, S., McKinney, G., Pelowitz, D., Prael, R., Sweezy, J., Waters, L., Wilcox, T. & Zukaitis, T. Initial MCNP6 release overview. *Nucl. Technol.* **180,** 298–315 (2012).

17.    Duderstadt, J. & Hamilton, L. *Nuclear Reactor Analysis.* (1976).

18.  Brown, D. A., Chadwick, M. B., Capote, R., Kahler, A. C., Trkov, A., Herman, M. W., Sonzogni, A. A., Danon, Y., Carlson, A. D., Dunn, M., Smith, D. L., Hale, G. M., Arbanas, G., Arcilla, R., Bates, C. R., Beck, B., Becker, B., Brown, F., Casperson, R. J., Conlin, J., Cullen, D. E., Descalle, M. A., Firestone, R., Gaines, T., Guber, K. H., Hawari, A. I., Holmes, J., Johnson, T. D., Kawano, T., Kiedrowski, B. C., Koning, A. J., Kopecky, S., Leal, L., Lestone, J. P., Lubitz, C., Márquez Damián, J. I., Mattoon, C. M., McCutchan, E. A., Mughabghab, S., Navratil, P., Neudecker, D., Nobre, G. P. A., Noguere, G., Paris, M., Pigni, M. T., Plompen, A. J., Pritychenko, B., Pronyaev, V. G., Roubtsov, D., Rochman, D., Romano, P., Schillebeeckx, P., Simakov, S., Sin, M., Sirakov, I., Sleaford, B., Sobes, V., Soukhovitskii, E. S., Stetcu, I., Talou, P., Thompson, I., van der Marck, S., Welser-Sherrill, L., Wiarda, D., White, M., Wormald, J. L., Wright, R. Q., Zerkle, M., Žerovnik, G. & Zhu, Y. ENDF/B-VIII.0: The 8th Major Release of the Nuclear Reaction Data Library with CIELO-project Cross Sections, New Standards and Thermal Scattering Data. *Nucl. Data Sheets* **148,** 1–142 (2018).

19.  Greenwood, L. R. & Johnson, C. D. User Guide for the STAYSL PNNL Suite of Software Tools. *PNNL-22253, Tech. Rep.* (2013). at <http://www.osti.gov/servlets/purl/1067961/>

CHAPTER FIVE: CONCLUSIONS

**5.1 Summary of Work**

In summary, additive manufacturing methods covered under the umbrella of
DWT have been used to demonstrate the feasibility of integrating these techniques in the
development of advanced and novel passive sensors having applications within extreme
environments such as those found in nuclear and aerospace industries. The advantages of
AM methods for sensor fabrication were demonstrated with the development of a flexible
capacitive strain gauge for aerospace applications, the development of advanced
manufactured melt wires to enhance their temperature resolution while enabling the
miniaturization of melt wires and melt wire packaging, and advanced manufactured
dosimeters to provide a method for directional flux monitoring within a reactor
environment. The work contained within this dissertation has

Chapter two explored the development of a capacitive based strain gauge using
aerosol jet printing with silver serving as the capacitive material and PMMA as the
dielectric while using Kapton as the flexible substrate to provide the necessary flexibility
for these devices to withstand high load/strain. All-purpose Barge Cement served as the
adhesive between the substrate and the Kevlar strap. The printed CSGs exhibited starting
capacitance values ranging from 42 pF to 15 nF and were subjected to dynamic and static
testing for arrangements where the electrodes were oriented either perpendicular or
parallel to the direction of strain. Additionally, cyclic testing was performed for electrode
arrangements perpendicular to the direction of strain. HE-RSGs were then tested

alongside CSGs to compare their response using the same attachment strategy and under the same conditions to evaluate their suitability for SHM of soft structural materials. Devices having a starting capacitance in the nF range were shown to have the highest sensitivity, and a gauge factor of 5.2 was obtained for those devices having their electrodes arranged perpendicular to the direction of strain. In this work, printed CSGs were determined to be better candidates for high elongation applications as they performed better in static situations, dynamic and cyclic events when compared to commercially available HE-RSGs.

Chapter three, introduced the use of AJP for nuclear applications with the fabrication of miniaturized melt wires to accommodate space limited experiments especially in material test reactors. To demonstrate the feasibility of incorporating AM techniques for the fabrication of advanced nuclear in-pile passive temperature sensors, a comparison between standard and AM melt wires of tin, aluminum and zinc. Through DSC and furnace testing, it was determined that the performance of the AM melt-wire capsule was consistent with that of the standard melt-wire capsule, which highlights a path towards miniaturized peak-temperature sensors for in-pile sensor applications. As discussed in this report, multiple discoveries during design optimization of AM melt wires created more challenges that were not initially expected.

Chapter four provided the demonstration of an advanced manufactured dosimeter capable of providing directional flux measurements within the TREAT reactor for the first time since its construction in 1958. Directional flux of within the TREAT core during irradiation experiments using DLP and MDP.

The work contained within this dissertation has served to open the door of possibilities of what sensors for extreme environments are and what they are capable of. The incorporation of additive manufacturing techniques within sensor design and fabrication broadens the design envelope so that innovations in sensors for extreme environments are no longer limited by what our tooling can do, but by what our minds can create.

## 5.2. Potential Future Directions

Integrating additive manufacturing methods within sensor design, development and fabrication for harsh environments found us on the pointy end of the spear while forging ahead with activities to provide proof of concept. For the most part, additive manufacturing methods had not been used previously to improve the sensor technologies for the targeted applications contained within this work. With most research endeavors, at the end of a project, while you may have achieved all the objectives you had initially planned, many seeds for future projects were more than likely planted in each and every failure or step to success, depending on perspective. The following provides, for each activity contained in this dissertation, the seeds of potential future directions for the work that could be pursued to further advance the technology and broaden their intended applications.

Regarding the AJP CSGs, there are several pathways that could be explored. The first could include optimizing the attachment strategy. This could be pursued through a variety of activities. To begin, an extensive down selection process should be performed to identify the best suited candidates to adhere the strain gauge to the component of interest. This activity would include the need to test and validate the adhesive and

mechanical properties of a wide range of adhesives. A second variable to include in this down selection progress would be through quantifying the strain transfer between the sensor substrate and the structural component of interest, which significantly affects the performance of the device. The second activity could encompass the identification of the appropriate techniques for applying the adhesive to minimize the interference of the adhesive in strain transfer between the structural component and the strain gauge. Furthermore, a third activity would encompass optimizing the design and fabrication of the strain gauge. Most significant, would be to mitigate the variability between device performance by introducing process control parameters to minimize the variance in capacitance of AJP strain gauges. Identification of a more appropriate dielectric material would significantly benefit the performance of the strain gauge, especially in high temperature environments. Finally, to expand the application of capacitive strain gauges for SHM to the nuclear industry substrates and dielectric materials capable of withstanding high temperatures and irradiation exposure are required. This could include an extensive down selection process that would require the need to identify methods for developing feedstock materials compatible with additive manufacturing technologies of interest to facilitate the integration of these materials within AJP capacitive strain gauges, which necessary if the novel aspects of AM are to be exploited.

To improve the performance and reliability of advanced manufactured melt wires there are several avenues to pursue. The first focus for the future work could be in broadening the material selection and geometries for the encapsulation, as we were unable to capture high-resolution XCT images and have a conclusive melting behavior of Al on SS substrate. This will enable AM melt wires to provide multiple material selection

for encapsulation as well as guarantee high-resolution XCT images of PIE melting. Additionally, it was possible that a very small amount of oxygen entered during an inert gas encapsulation that could have oxidized the aluminum to be unidentifiable post-melting in the XCT image. To further improve the encapsulation method, entrapping Helium required laser welding a weephole through a quartz window of an enclosed chamber where air could be purged and replaced with helium using a vacuum and having a weep hole machined for perfect one-shot weld. Finally, the last focus of future work would be on the printed materials. Studying binder effects on material performance, determine effectiveness of oxygen getter additives, and design specific print patterns advantageous to specific material melting characteristics (pooling, surface tension collection, rounded edges, etc.) would greatly enhance the post-melting XCT images. Again, being able to broaden melt wire selection and how each material has its unique material characteristics could benefit the post-melting evaluation.

The AMDs discussed in this work measure directional flux, not neutron current. Future work could include activities to allow neutron current to be obtained. This could include the identification and integration of an appropriate neutron filter or shield. Candidates for the neutron filter would need to account for neutron cross section and other experimental requirements. Additionally, optimizing the AMD foil dimensions for device performance is needed, and could be accomplished by integrating modeling and simulation efforts within the device design process. To expand on this, the activation of the radioisotopes from the neutron flux in the reactor should only be produced from neutrons traveling perpendicular to the face of the flux foil and eliminating a direction of neutron interaction compared to the current configuration is necessary. Finally, AMDs

could be used for further investigations into nuclear data to improve the nuclear data libraries by providing thin materials with negligible self-shielding or attenuation considerations.

A common theme amongst all the applications listed in this dissertation is the need to develop feedstock compatible with various additive manufacturing techniques considered most appropriate for the intended environment. Through materials development and a significant expansion of the library of materials available for DWT techniques to include those that are more relevant for the nuclear and aerospace industries, DWT has incredible potential to broaden the capabilities of sensors intended for use in extreme environments. In each case, however, the development of new materials and inks will require thorough optimization, and theoretical guidance in this area is severely limited. Significant work could be found in the area of developing a comprehensive evaluation of ink design for DWTs that are guided by physical principles of the printing processes, numerical modeling, and in-situ process monitoring methods.

APPENDIX

**Supplementary Information – Aerosol Jet Printed Capacitive Strain Gauge for Soft**

**Structural Materials**

**Supplementary Information**

**Aerosol Jet Printed Capacitive Strain Gauge for Soft Structural Materials**

Kiyo T. Fujimoto[1,2,3], Jennifer K. Watkins[1,2,4], Timothy Phero[1,2], Doug Litteken[5], Kevin Tsai[3], Takoda Bingham[6], Kshama Lakshmi Ranganatha[7], Benjamin Johnson[7], Zhangxian Deng[6], Brian Jaques[1,2] and David Estrada[1,2]

[1]Center for Advanced Energy Studies, Boise State University, Idaho Falls, ID USA
[2]Micron School of Materials Science and Engineering, Boise State University, Boise, ID USA
[3]Measurement Sciences Department, Idaho National Laboratory, Idaho Falls, ID 83402 USA
[4]Department of Advanced Fuel Manufacturing and Development, Idaho National Laboratory, Idaho Falls, ID USA
[5]NASA Johnson Space Center, Houston, TX USA
[6]Department of Mechanical Engineering, Boise State University, Boise, ID USA
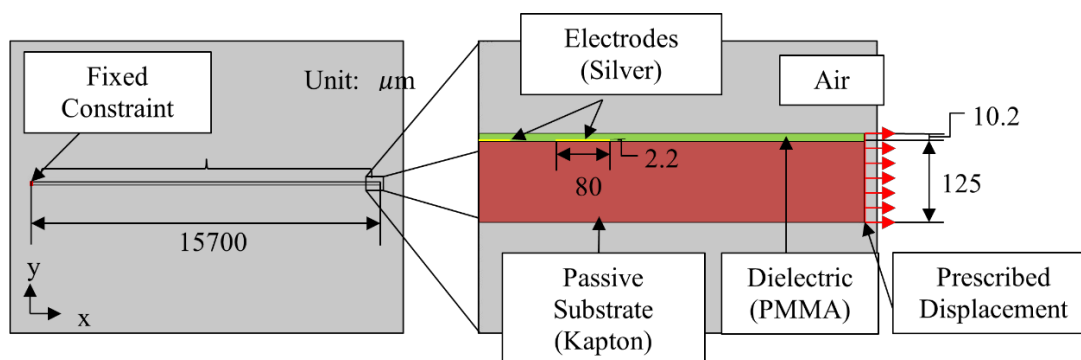[7]Department of Electrical and Computer Engineering, Boise State University, Boise, ID USA

**Figure A.1.    Finite Element model geometry and boundary conditions. Using COMSOL Multiphysics. See Appendix A Discussion.**

162

**Table A.1.    Key material properties used in for the physics in the COMSOL model**

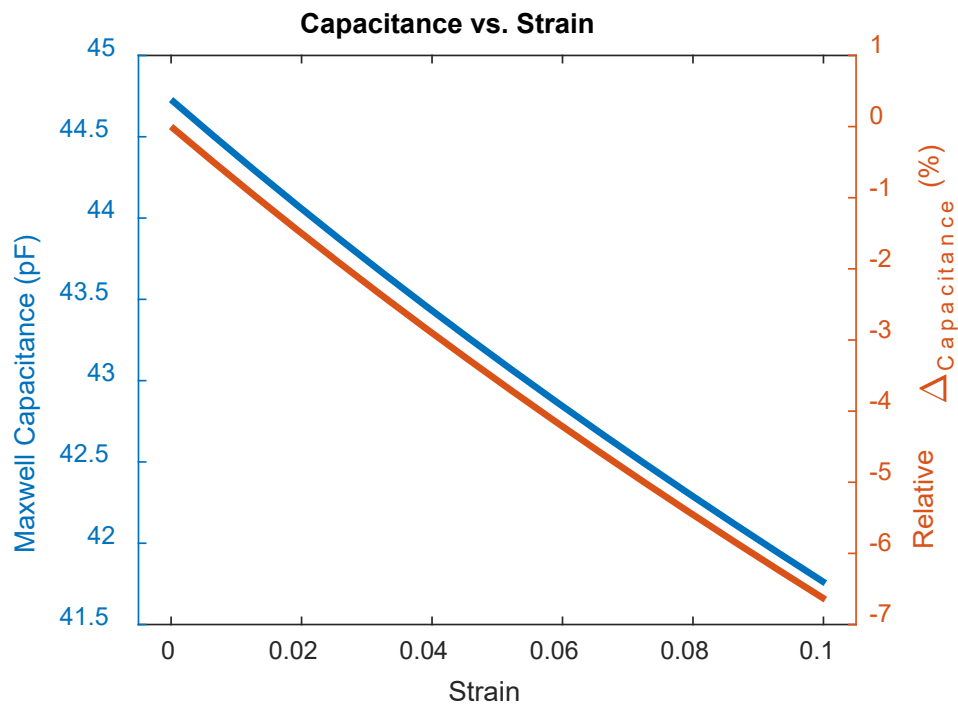| Material | Young's modulus (GPa) | Density (kg m-3) | Poisson's ratio | Relative permittivity |
|----------|----------------------|------------------|-----------------|----------------------|
| Silver | 83 | 10500 | 0.37 | 100000 |
| Kapton | 2.8 | 1420 | 0.34 | 4 |
| PMMA | 3 | 1190 | 0.4 | 4.9 |
| Air | – | – | – | 1 |



**Figure A.2.    Maxwell capacitance and relative change in capacitance with increase in strain. Finite element and analytical modeling shows that the capacitance decreases from 44.73 pF to 41.75 pF as the substrate strain increases from 0 to 10%. This corresponds to a gauge factor of 0.663. See Appendix A Discussion.**
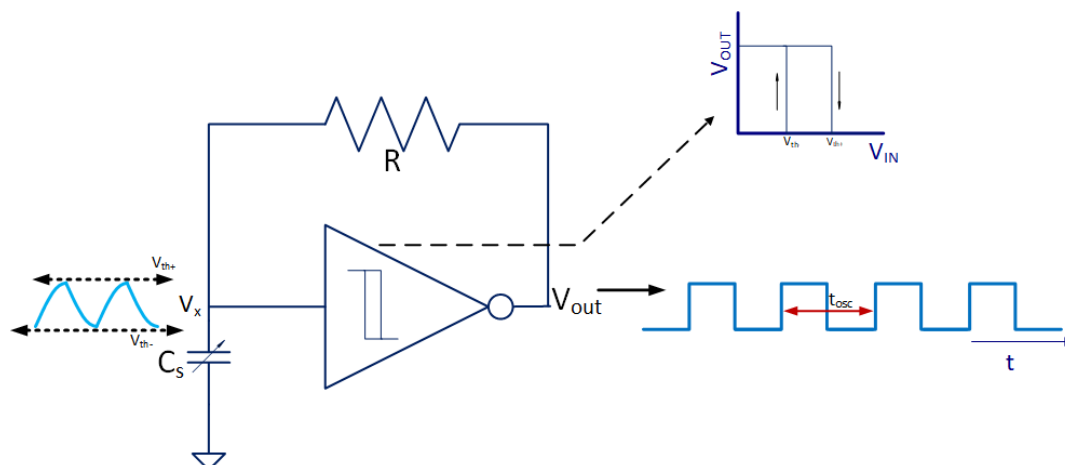
**Figure A.3.** Schematic of relaxation oscillator. The schematic for a digital readout system which introduces the ability to directly measure capacitance for high rates of strain and large capacitance range. See Appendix A Discussion.
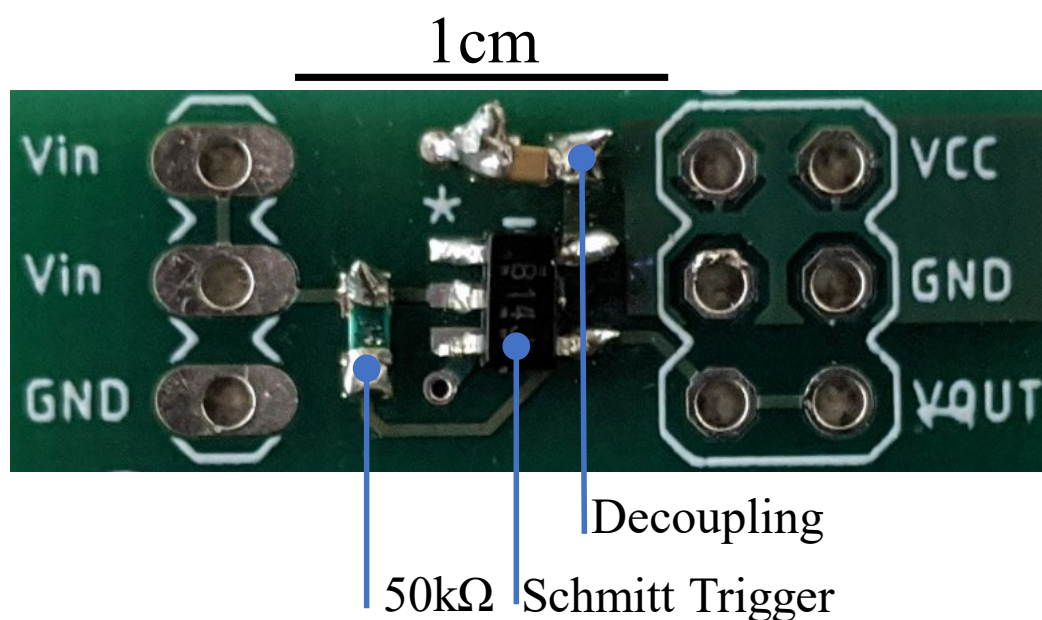


**Figure A.4.** Example readout PCB relaxation oscillator PCB. The total area of the active circuitry was roughly 1 cm x 1 cm due to the components required. A coupling capacitor was used to decrease variations in supply voltage, and a 50 kΩ feedback resistor was used. Depending on the application, the oscillation period can be adjusted by changing the feedback resistance. See Appendix A Discussion.
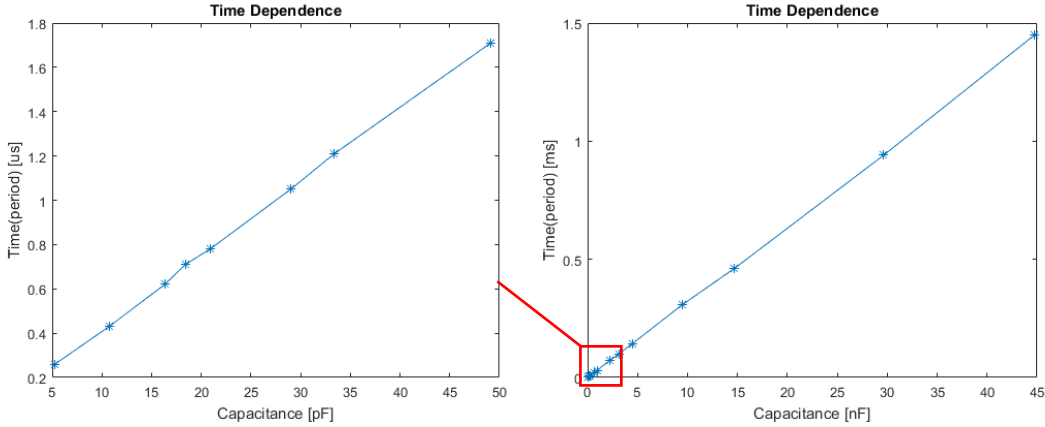
**Figure A.5.** **Oscillation period for the PCB readout was measured over a wide range of capacitance. To demonstrate the wide dynamic range of the readout circuitry, we measured the oscillation period for several capacitance values that correspond to the variance exhibited by the strain gauges. Oscillation jitter (pulse-to-pulse period variance) was 7.542 ns, which corresponds to 188 fF of capacitance resolution and approximately 0.99% strain. See Appendix A Discussion.**

**Table A.2.** **Capacitance measurements with Direct Digital Readout**

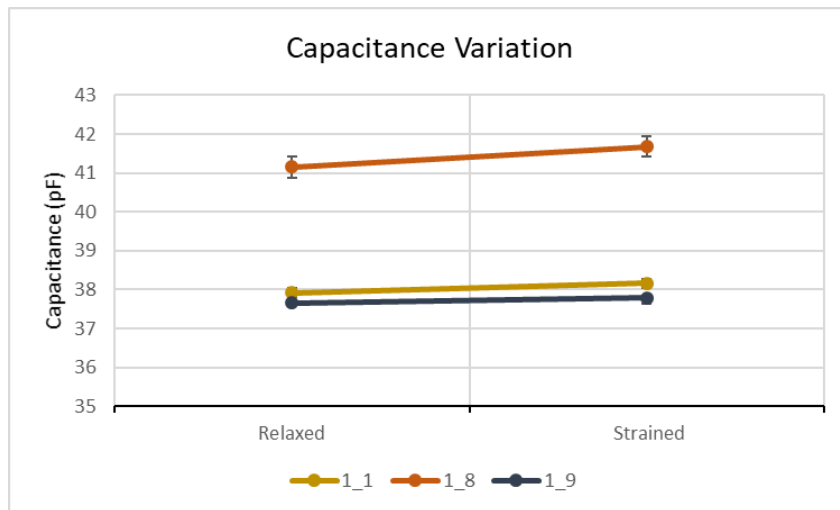| Strap | Relaxed | | | Strained | | |
|---|---|---|---|---|---|---|
| | $f_{OSC}$ (kHz) | $t_{OSC}$ (µs) | Capacitance (pF) | $f_{OSC}$ (kHz) | $t_{OSC}$ (µs) | Capacitance (pF) |
| 1_1 | 659.2 | 1.517 | 37.92 | 655.1 | 1.526 | 38.16 |
| 1_8 | 607.5 | 1.64 | 41.15 | 599.8 | 1.66 | 41.68 |
| 1_9 | 663.8 | 1.507 | 37.66 | 661.5 | 1.51 | 37.79 |



**Figure A.6.** **Graph of the Variation in the Capacitance measured with the PCB readout for three different printed CSGs. See Appendix A Discussion.**

**Appendix Discussion**

A.1 Finite element and analytical modeling

Modeling using multiphysics can be used to verify interdependencies of theory and physical testing. COMSOL Multiphysics can allow for strain (solid mechanics) to be solved at the same time as capacitance (electrostatics). Appendix A Figure 1 is a 2D cross sectional view model constructed in COMSOL Multiphysics. The thickness of this model (depth along the z-axis) is 15.1 mm. A circular air domain with a radius of 23.55 mm is defined to replicate the infinite air around the sensor in practice. The strain gauge is fixed on the left end. A boundary displacement is prescribed along the x-axis on the other end of the sensor, as shown in Appendix A Figure 1. The displacement is increasing at a constant rate of 0.1 mm s$^{-1}$. A total of 100 silver electrodes are evenly distributed along the x-axis on the substrate. Each electrode is represented by an 80 by 2.2 µm rectangular domain. To detect the capacitance every other electrode had to be linked, one set was for the constant voltage of 1 V, and the other set was for the ground which had no electrical charges. The capacitance between two sets of electrodes are calculated by the lumped parameters using the energy method. Material porosity was ignored and material properties used in this study are summarized in Appendix A Table 1.

Appendix A Figure 2 demonstrates the expected behavior for the printed CSGs where the input displacement strains the substrate and changes the spacing between electrodes. Therefore, the capacitance varies with respect to the prescribed displacement. Appendix A Figure 2 shows that the capacitance decreases from 44.73 pF to 41.75 pF as the substrate strain increases from 0 to 10%. This corresponds to a gauge factor of 0.663.

A.2 Digital capacitance readout

For practical application of the printed CSG's it will be necessary to quickly and efficiently obtain the capacitance read out for analysis while minimizing the effects of interference. The ability to accommodate a large capacitance range from printed strain gauges while having a fast and efficient response can be achieved using a digital red out that uses frequency rather than voltage.

The printed strain gauges have a wide variance in their capacitance values, i.e., the range of capacitances lie in pF to nF range. This wide variance imposes significant challenges for an electronic readout system due to the dynamic range requirements. Achieving sub-pF resolution with nF range would likely require an 18-bit analog-to-digital converter for a traditional analog readout scheme. Furthermore, a high rate of strain requires a readout circuit that is efficient to detect the subtle changes in the capacitances very quickly due to the strain exerted on the inflatable habitats, parachutes, and decelerator systems. To accommodate the large capacitance range with fast and efficient readout, we used a frequency readout rather than a voltage readout do its relatively unconstrained dynamic range (time vs. bits). To implement a frequency readout, we used a relaxation oscillator that outputs a digital clock that is linearly dependent on the change in capacitance of the strain gauge. We chose to implement the relaxation oscillator with an off-the-shelf Schmitt trigger as seen in Appendix A Figure 3.

The oscillator creates a waveform whose period ($t_{osc}$) is a function R, $C_S$, the supply voltage ($V_{CC}$), and the switching thresholds ($V_{th+}$, $V_{th-}$). $C_S$ represents the capacitance of the gauge and is the only parameter that changes. Each period changes as per equation 1.1,

$$t_{osc} = RC_s \, ln \left( \frac{((V_{CC} - V_{th-})V_{th+}}{(V_{CC} - V_{th+})V_{th-}} \right) \tag{1}$$

$$f_{\text{osc}} = \frac{1}{t_{\text{osc}}} \qquad\qquad (2)$$

By measuring the period of each oscillation, we can determine the capacitance value and therefore strain. In addition to accommodating a large dynamic range, this readout scheme has several advantages compared to an analog readout: 1.) The output signal is digital meaning it is less sensitive to interference, 2.) Digital signaling obviates the need for an analog-to-digital converter, making it amenable to parallelized data readout from multiple gauges. The frequency readout is only limited by the temporal resolution of the digital sampling circuit (e.g., microcontroller or FPGA), 3.) No carrier signal (e.g., sinewave) is required to measure a complex impedance meaning only a 3-wire interface is required ($V_{\text{CC}}$, GND, $V_{\text{OUT}}$) for the readout circuit.

A.3 Method for reporting electrical measurements and strain response

Capacitance measurements were obtained with an Agilent HP 4284A Precision LCR Meter (10 kHz at 5V), and resistance measurements were obtained with a Keithley 2182A/6220. For capacitance measurements, at each specified load, measurements were obtained in triplicate. These measurements were then averaged. Resistance values were then obtained from an average of 500 collected measurements.

Due to the large variance in the initial capacitance measurements, the data was reported as a relative change in capacitance, represented as $\Delta C_{\text{relative}}$ (%)

$$\Delta C_{\text{relative}}(\%) = \frac{C_x - C_0}{C_0} \cdot 100 \qquad\qquad (3)$$

where $C_0$ is the initial capacitance, and $C_x$ is the capacitance after reaching the desired target load (dynamic and cyclic) or time (static).

For consistency, the resistance data was also reported as a relative change in resistance, represented as $\Delta \Omega_{\text{relative}}$ (%)

$$\Delta\Omega_{\text{relative}}(\%) = \frac{R_x - R_0}{R_0} \cdot 100 \tag{4}$$

Where $C_0$ is the initial capacitance, and $C_x$ is the capacitance after reaching the desired target load (dynamic and cyclic) or time (static).

*Uncertainty analysis for error reporting.* The capacitance for the printed CSGs and resistance uncertainty for the commercial strain gauges was estimated from the general formula for propagation of error, which utilizes the partial derivative method:

$$\sigma_{\Delta C_{\text{relative}}} = \sqrt{\left(\frac{\partial \Delta C_{relative}}{\partial C_0}\right)^2_{C_x} S_{C_0}{}^2 + \left(\frac{\partial \Delta C_{relative}}{\partial C_x}\right)^2_{C_0} S_{C_x}{}^2} \cdot 100 \tag{5}$$

and

$$\sigma_{\Delta\Omega_{\text{relative}}} = \sqrt{\left(\frac{\partial \Delta\Omega_{relative}}{\partial R_0}\right)^2_{R_x} \sigma_{R_0}{}^2 + \left(\frac{\partial \Delta\Omega_{relative}}{\partial R_x}\right)^2_{R_0} \sigma_{R_x}{}^2} \cdot 100 \tag{6}$$

where $\sigma_{\Delta C_{\text{relative}}}$ or $\sigma_{\Delta R_{\text{relative}}}$ is the total uncertainty in $\Delta C_{\text{relative}}$ or $\Delta\Omega_{\text{relative}}$ expressed as a percent, respectively. $S_{C_0}, S_{C_x}, S_{R_0}$ and $S_{R_x}$ represent the standard deviation or uncertainty for the initial capacitance, capacitance at the targeted load or time, initial resistance and resistance at the targeted load or time, respectively.

So,

$$\sigma_{\Delta C_{\text{relative}}} = \sqrt{\left(-\frac{C_x}{C_0{}^2}\right)^2 \sigma_{C_0}{}^2 + \left(\frac{1}{C_0}\right)^2 \sigma_{C_x}{}^2} \cdot 100 \tag{7}$$

And

$$\sigma_{\Delta\Omega_{\text{relative}}} = \sqrt{\left(-\frac{\Omega_x}{\Omega_0{}^2}\right)^2 \sigma_{\Omega_0}{}^2 + \left(\frac{1}{\Omega_0}\right)^2 \sigma_{\Omega_x}{}^2} \cdot 100 \tag{8}$$

Where $C_x$ is the capacitance at a specific target load (dynamic and cyclic) or time (static), $C_0$ is the initial capacitance, $\Omega_x$ is the resistance at a specific target load (dynamic and cyclic) or time (static), and $\Omega_0$ is the initial resistance.